Study of pion-kaon femtoscopic correlations in Pb−Pb collisions at $\sqrt{s_{\mathrm{NN}}}$= 2.76 TeV with ALICE detector at the LHC

A thesis submitted in partial fulfillment of the requirements
of the degree of Doctor of Philosophy

Submitted by:

Ashutosh Kumar Pandey

(Roll No. 11I120008)

Under the guidance of:

Prof. Sadhana Dash

Department of Physics,

Indian Institute of Technology Bombay,

Powai, Mumbai 400076.

April, 2019

Dedicated to

my family, teachers and country

Thesis Approval

Thesis entitled "**Study of pion-kaon femtoscopic correlations in Pb−Pb collisions at $\sqrt{s_{\rm NN}}$= 2.76 TeV with ALICE detector at the LHC**" by **Ashutosh Kumar Pandey** is approved for the degree of Doctor of Philosophy.

Examiners

(1) Dipankar Dutta

(2) B Hanas

Supervisor

Sadhana Dash

Chairman

P. Biswas

(Prof. P. K. Biswas)

Date : 29/7/19

Place : Mumbai

Declaration

I declare that this written submission represents my ideas in my own words and where other's ideas or words have been included, I have adequately cited and referenced the original sources. I also declare that I have adhered to all principles of academic honesty and integrity and have not misrepresented or fabricated or falsified any idea/data/fact/source in my submission. I understand that any violation of the above will be cause for disciplinary action by the Institute and can also evoke penal action from the sources which have thus not been properly cited or from whom proper permission has not been taken when needed.

Ashutosh Kumar Pandey

Ashutosh Kumar Pandey

Roll No. 11I120008

Date : 29.07.2019

Place : MUMBAI

Abstract

The main goal of studying nucleus-nucleus collisions at ultra-relativistic is to characterize the dynamical processes by which QGP (Quark Gluon Plasma) like system is produced and to study the properties this hot and dense matter exhibits. However, experimentally, it is very challenging to study the QCD matter at high temperature and density because of very short spatio-temporal dimensions of the system produced. The study of bulk matter properties requires a very good understanding of the dynamics and chemistry of the collision, which can only be acquired by coordinated analysis of experimental data and theory. The ALICE (A Large Ion Collider Experiment) experiment at the LHC (Large Hadron collider) at CERN is a dedicated experiment to study the hot and dense matter created in ultra-relativistic Heavy Ion Collisions. It provides an opportunity to study the properties of the equilibrated system of de-confined state of quarks and gluons known as Quark Gluon Plasma via various experimental probes. The tool to characterize the spatio-temporal properties of the collision region at femtometer scale is known as *Femtoscopy* and this study is essential to address the dynamical equilibration process through which the QCD matter proceeds. The correlations of two final-state particles at small relative momentum are the best source to provide the direct link to the size and lifetime of the smaller system. The work in this thesis presents the first ever measurement of the emission asymmetry at the LHC energies using the ALICE detector. The study has been performed using the data collected by ALICE experiment at the LHC in Pb−Pb collisions at $\sqrt{s_{\mathrm{NN}}}$= 2.76 TeV. The analysis was carried out in different centrality classes namely 0-5%, 5-10%, 10-20%, 20-30%, 30-40% and 40-50%. The thesis describes the detailed steps of the femtoscopic technique required to determine the size of the homogeneity region of pion-kaon emission and the emission asymmetry. The analysis reported in this thesis was performed with the cartesian coordinate formalism. The method involved the construction of correlation function and the Double Ratio of the pion-kaon pairs. The pions and kaons were identified by the combined information provided by the TPC and the TOF detector in different momentum ranges. The selected pairs were corrected for the two-track merging effects due to detector resolution and γ conversions. The correlation functions and double ratios were obtained for all charge combinations of pion-kaon pairs in different centrality classes. The obtained correlation function was also corrected for the background pairs, originating from non-femtoscopic sources like elliptic flow, resonance decay etc. The relevant parameters of the source, namely the size and the emission asymmetry was extracted by fitting the correlation function using

the CorrFit software. The double ratio deviated from unity in the *Out* direction for all combinations of pion-kaon pairs. This observation suggested that the space-time position of pion and kaon emissions are not same and the pions are emitted closer to the centre of the source compared to kaons. The kaons are emitted earlier than pions. The average size of the pion-kaon homogeneity region and the emission asymmetry was found to decrease for all charge combinations from most central to peripheral collisions. This observation was consistent with the previous measurements of source size using identical particle femtoscopy. The value of emission asymmetry in *Out* direction decreased from most central collisions to peripheral collisions and the trend of emission asymmetry with respect to centrality is consistent with the previous observation at RHIC energies. The obtained results are also compared to the expectations of Therminator2 event generator coupled with (3+1)-dimensional viscous hydrodynamic calculations. The pion-kaon emission asymmetry obtained with the model agreed with the experimental observation when an additional time delay of 2.1 fm/c was introduced for kaons. The results obtained in this analysis are consistent with the hydrodynamic-induced evolution of the system created in heavy ion collisions which favors a strong radial flow in central collisions. The origin of emission asymmetry can be understood by the strong radial flow hypothesis and the interplay between the collective and thermal movement of the dense matter created in collisions of heavy ions.

Contents

List of Figures

List of Tables

Chapter 1

Introduction

"In modern physics, there is no such thing as 'nothing'. Even in a perfect vacuum, pairs of virtual particles are constantly being created and destroyed. The existence of these particles is no mathematical fiction. Though they cannot be directly observed, the effects they create are quite real. The assumption that they exist leads to predictions that have been confirmed by experiment to a high degree of accuracy."
− Richard Morris

Abstract: This chapter presents a brief overview of the particle interactions and fundamental forces. The discussion is followed by introduction of heavy-ion physics and the experimental signatures of the formation of strongly interacting matter called Quark Gluon Plasma (QGP). The thesis topic is briefly introduced in one of the signatures followed by the scope and organization of the thesis.

1.1 Science

A normal human being when born starts crying just after birth and the reasons could be hunger, attention or many more. The initial way of communicating thoughts is via crying. As the human being grows, and starts to see things happening around, the daily events are questioned and thoughts are analysed. This inquisitive and curious nature of the human mind has made human beings different from other animal species around. The evolution of the humankind is attributed to this curious and thinking mind. Whenever, someone tries to study any phenomenon or event in a systematic and organized way, which can be tested experimentally, we call the study as *science*. The word "*science*", derived from a Latin word "*scientia*", meaning *knowledge* [1]. Science has in many ways impacted our daily life and it will not be an exaggeration, if we state that science is playing a definitive role in our daily lives. Science has given us medicines, vehicles, quality food, internet, entertainment and almost everything necessary for an enriched quality of life on this planet. The modern science can be divided into many branches depending on the subject of interest. The branches of science (known as the basic sciences) are Physics, Chemistry and Biology which are briefly discussed in following sections:

1.1.1 Biology

The word *biology*, came from the Greek word *βίος* (bios), "life" and the suffix -*λογία* (-logia), "study of" [2]. This means, biology is the branch of science which studies the life and physical structure, chemical processes, molecular interactions, physiological mechanisms, development and evolution of living organism. In biology, the 'cell' is treated as the fundamental unit of life. All living organisms are made up of either a single cell or many cells. Cells arise from pre-existing cells by the process of cellular division. The theory of evolution, suggests that all living organisms on the Earth have common ancestral origin. It is believed that life appeared on Earth approximately 3.5 billion years ago.

1.1.2 Chemistry

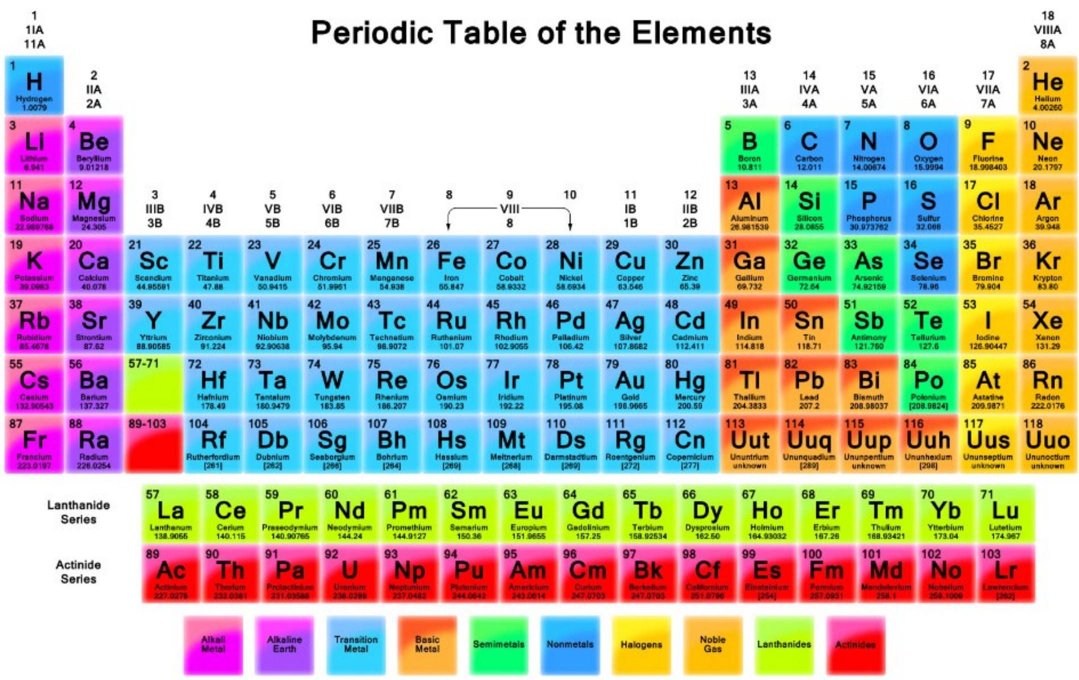

Figure 1.1: Periodic Table of the Elements [3].

Chemistry is the branch of science, which involves the study of molecules/compound, composed of *atoms* or *elements* (Figure 1.1), by means of its composition, structure, properties, behavior and the reactions with other compounds [4]. This includes the interactions of atoms and molecules via chemical bonds to form new chemical compounds. The atoms and molecules can interact by four types of chemical bonding:

- Covalent bonds – In covalent bonding, sharing of one or more electron(s) takes place.
- Ionic bonds – In ionic bonding, one atom donates one or more electrons to another atom forming ions.
- Hydrogen bonds – It is formed as a result of partial electrostatic attraction between a hydrogen atom (H) bound to a more electronegative atom and another adjacent atom bearing a lone pair of electrons. It can occur at both *intermolecular* and *intramolecular* level.
- Van der Waals bonds – It is a distance dependent interaction between atoms or molecules. These attractions are comparatively weaker and cease to exist at longer distances between interacting molecules.

1.1.3 Physics

Physics is the oldest branch of natural science that studies matter by means of its motion and behavior through space and time. The word *physics* is derived from Greek word *φυσική* (*ἐπιστήμη*) meaning 'knowledge of nature' [5]. Basically, it aims to study nature and the way it behaves. The study includes the origin, composition and evolution of the universe. The building blocks of the universe i.e. the fundamental particles and their interactions are briefly discussed in subsequent sections.

1.2 States of Matter

The visible *matter*[1] is formed as a result of varied interactions between the elementary particles, of which it is composed of. Matter can exist in four different states:

- **Solid** – It is the state of matter where the composite particles are tightly packed together [6; 7]. They have a definite shape and volume. In solids, the electrons

[1]Matter is anything which has mass and occupies some volume in space.

of each atom are in motion and the atoms exhibit small vibrational motion, while being fixed in their position.

- **Liquid** – It is the state of matter which takes the shape of its container but the volume remains constant over a wide range of pressure at constant temperature [6; 7]. A liquid is almost an incompressible *fluid*.
- **Gas** – A gas has no definite shape or volume. It is a compressible fluid. The gas molecules have enough kinetic energy and the effect of intermolecular forces is small (zero for *ideal gases*) [6; 7]. The mean free path of gas molecules is very large compared to molecular dimensions.
- **Plasma** – Plasma may be the most common state of matter in the universe [6; 7]. It consists of unbound positive and negative particles. Any movement of a charged plasma particle affects and is affected by the fields created by the other charges. Plasmas do not have well defined shape or volume but plasmas are electrically conductive.

1.3 Fundamental Interactions

The different states of matter and their properties can be studied by studying the fundamental composition of matter and the interactions between them. The most elementary particles which constitute the visible universe are quarks and leptons. Universe also contains dark matter and energy . It is important to understand how the elementary particles come together to form matter and the way they interact among themselves. The different ways by which fundamental particles interact with each other are called fundamental interactions. There are four known fundamental interactions.

1.3.1 Gravitational Interaction

The term *gravitation* originates from the latin word *gravitas* which means *weight*. Gravitational interaction is one of the fundamental interactions which acts on particles having mass and energy [8]. It is the weakest among the four fundamental interactions, approximately 10^{38} times weaker than the strong force (section 1.3.4), 10^{36} times weaker than the electromagnetic force (section 1.3.2) and 10^{29} times weaker than the weak force (section 1.3.3). It is always attractive in nature. Although gravitational force has an infinite range, it becomes weaker for objects at farther distances. The force equation is

Property	**Gravitation**	**Weak**	**Electromagnetic**	**Strong**
Affects	Mass/Energy	Flavor	Electric charge	Color charge
Affected	All particles	Gauge bosons and leptons	Electrically charged	Quarks, gluons
Force carriers	Graviton (not observed)	$W^{\pm}, Z^0$	γ	Gluons
Relative strength	1	10^{26}	10^{37}	10^{39}
Range (m)	∞	10^{-17}	∞	10^{-14}

Table 1.1: Four fundamental forces and their properties [8]

the following:

$$F = G\frac{m_1 m_2}{r^2} \tag{1.1}$$

where F is the gravitational force, m_1 and m_2: masses of the interacting objects, r : distance between the centers of the objects and G is the gravitational constant. In SI unit, G has a value 6.674×10^{-11} N/kg^{2}m^2.

The long range and mass dependence of gravitational force makes it responsible for large scale phenomena like planetary motion, structure of galaxies, black holes and expansion of universe. The universal theory of gravitation given by Newton is a good approximation for phenomena like planetary motion but accurate description in terms of *geometry of space-time* is given by *General Theory of Relativity*. The merging of General Theory of Relativity with quantum mechanics is called theory of "quantum gravity" which

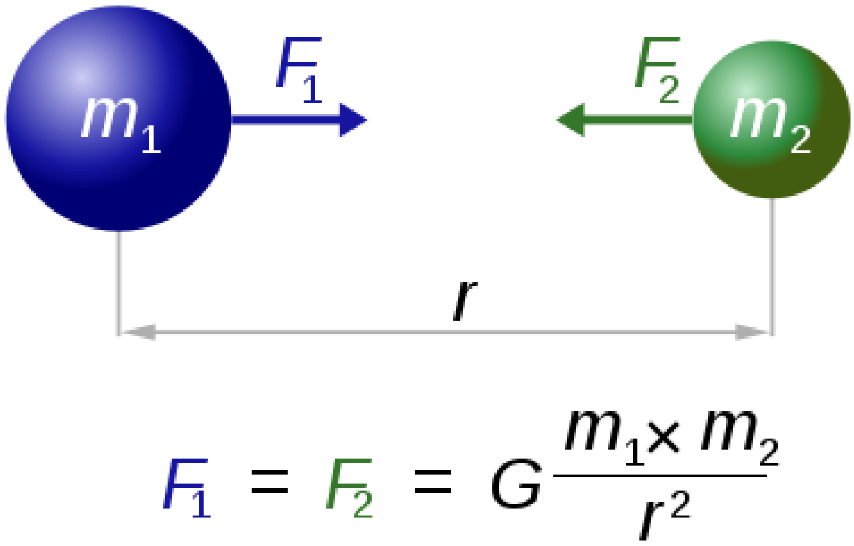

Figure 1.2: Newton's law of universal gravitation [9].

is applicable at temperature T ~ $10^{19} GeV \sim 10^{32} K$. This was the initial temperature of universe at the time of Big-Bang. The mediator particle of gravity is known as *Graviton* but it is not yet experimentally discovered.

1.3.2 Electromagnetic Interaction

The electrically charged particles interact through Electromagnetic force which is repulsive for same kind of charges and attractive for oppositely charged particles [8]. The word *Electromagnetism* has emanated from compound form of two Greek words, $\eta\lambda\epsilon\kappa\tau\rho o\nu$ *ēlektron*, "amber", and $\mu\alpha\gamma\nu\eta\tau\iota\varsigma$ *magnētis lithos*, meaning "Magnesian stone"which is an iron ore. This is an infinite range interaction and is responsible for most of the physical processes we see around us like friction, motion of electrons inside atom etc. Electromagnetic interaction is studied under the theory of *Electrodynamics.* For charged particles at rest, the electrostatic potential V varies with distance r as:

$$V(r) \sim \frac{1}{r} \tag{1.2}$$

When the charged particles move with respect to each other, the combined effect of electric and magnetic forces acts between them. Electrical and magnetic forces were believed to be different in ancient times. In 19th century, James Clerk Maxwell discovered that electricity and magnetism are not different interactions but two aspects of the same fundamental interaction. Maxwell's equations quantified and unified both the interactions

[10]. The constant speed of light in vacuum (c) derived from Maxwell's equations is consistent with the c, coming from *the theory of special relativity* proposed by Albert Einstein in 1905.

The mediating particle for electromagnetic interaction is *photon*(γ). It has zero charge, zero rest mass and spin 1.The Feynman's diagram for a typical electromagnetic interaction is shown in Figure. 1.3.

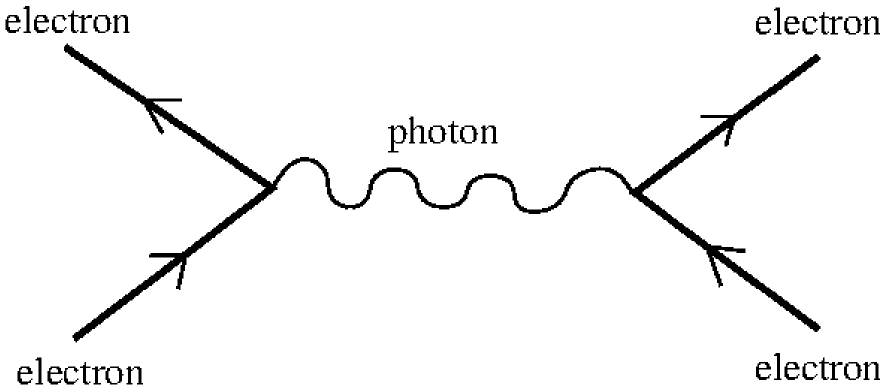

Figure 1.3: Feynman's diagram for electromagnetic interaction

1.3.3 Weak Interaction

The weak interaction or weak nuclear force is the interaction between sub-atomic particles. It is responsible for β decay and hence, plays essential role in nuclear fission reactions [8].

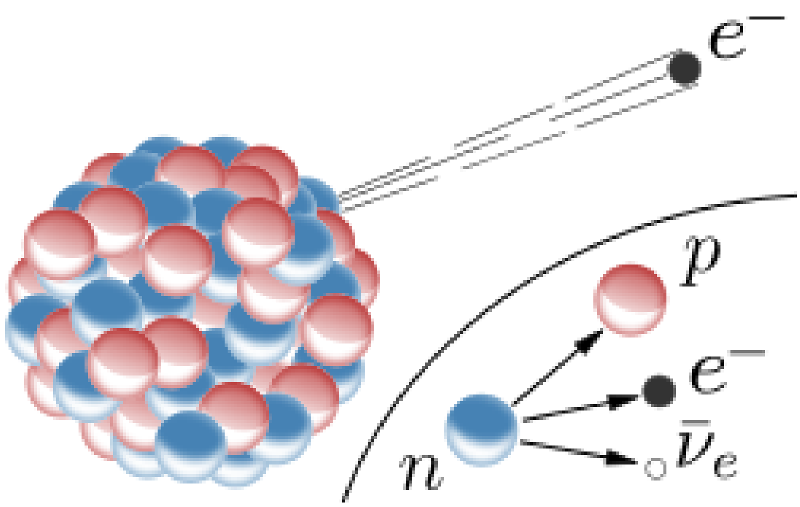

Figure 1.4: The radioactive beta decay due to weak interaction [11].

The mediating *Gauge bosons*[2] (section 1.4) for weak interaction are $W^{\pm}$ and Z^0 bosons. The weak interaction takes place only at small subatomic distances, lesser than the diameter of a proton. The range of this force is $10^{-18}m$ and the long range behavior is given by the following :

$$F \sim \frac{1}{r} e^{-m_{W,Z} r} \tag{1.3}$$

where $m_{W,Z}$ is the mass of mediating boson. There are two kinds of weak interactions : charged mediated by $W^{\pm}$ bosons and neutral mediated by Z bosons. Quarks and leptons participate in weak interactions. The Feynman diagram for charged and neutral weak interactions are shown in Figure 1.5 and 1.6, respectively.

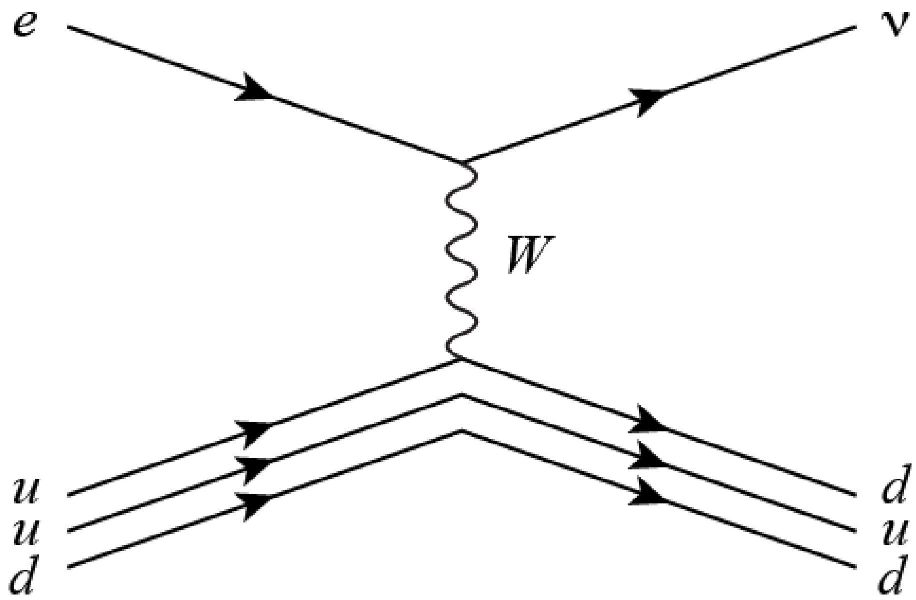

Figure 1.5: Feynman's diagram for charged weak interaction

The weak interaction has some unique properties, like:

- The weak interaction is the only interaction in which, flavor of quarks can be changed i.e. one type of quark can be changed to another type (Figure 1.5). This implies that flavor is not conserved in weak interaction and hence the theory of weak interaction is also called *Flavordynamics*.
- It is the only interaction where violation of parity-symmetry (**P**) takes place.
- It is also the only interaction where violation of charge-parity (**C-parity**) symmetry takes place.

[2]In the Standard Model (section 1.4), force carriers that mediated the electromagnetic, weak and strong fundamental interactions are known as Gauge bosons.

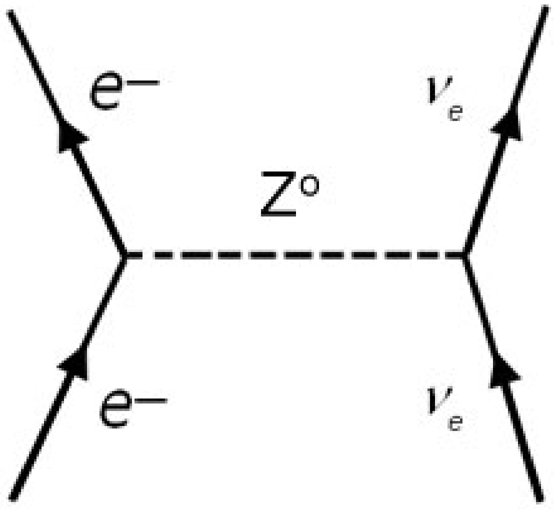

Figure 1.6: Feynman's diagram for neutral weak interaction

- The mediators of the weak force have significant masses (Figure 1.8)

1.3.4 Strong Interaction

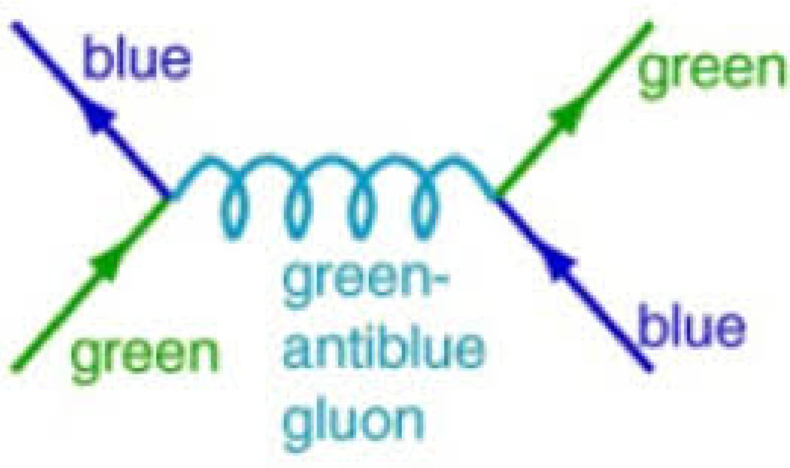

Figure 1.7: Feynman's diagram for strong interaction

The strong interaction is the strongest interaction but it is not felt in daily life because it's range is very small (of the order of $10^{-15}m$) [8]. It bounds *nucleons* i.e. protons and neutrons inside the *nucleus* and quarks inside the *hadrons*. This interaction is mediated by *Gluons* which has zero mass, zero electric charge and spin 1. Gluons like quarks contain color charge and therefore they can interact with each other. This self-interaction makes the study of strong interaction very complicated and interesting compared to other interactions. As the strong interaction acts between colored objects like quarks and gluons, the theory under which strong interaction is studied is called *Chromodynamics*. The theory is briefly described in section 1.5. The interaction potential of strong interaction varies with distance as following:

$$V(r) \sim \frac{-\alpha_s(r)}{r} + \sigma r \tag{1.4}$$

$\alpha_s \rightarrow 0$ as r $\rightarrow 0$ The Feynman diagram for a typical strong interaction has been shown in Figure 1.7.

1.4 Standard Model

One of the major aims of physicists around the world is to unify these known interactions so that one can have an integrated theory of everything we observe in this universe. The properties and comparison of the four interactions is shown in Table 1.1. It is clear that the gravitational force is very weak compared to other forces, and its effect on smaller particles is very small. So in general, gravity can be excluded, while studying *particle physics*.[3] In 1961, Sheldon Glashow discovered a way to combine weak and electromagnetic interactions. This was the first step towards the Standard Model. Steven Weinberg and Abdus Salam gave it, its modern form in 1967 by incorporating the Higgs mechanism into Glashow's electroweak interaction. It is believed that all elementary particles in the Standard Model i.e. fermions (quarks and leptons) and W, Z bosons get their masses through the Higgs mechanism[4]. The electroweak theory became well accepted after CERN discovered the neutral weak current caused by Z boson in 1973. This discovery won the 1979 Nobel Prize in Physics which was shared by Glashow, Salam and Weinberg. Later, in 1983, $W^{\pm}$ and Z^0 boson were discovered and their mass ratio was found to be consistent with the predictions of the Standard Model. The **Standard Model (SM)** of the particle physics is the theory which classifies all known elementary particles (Figure 1.8) as well as unifies the electromagnetic, weak, and strong interactions, excluding the gravitational force in the universe. The SM was developed by many scientists around the

[3]Particle physics or high energy physics is the branch of physics which basically investigates the smallest detectable particles and their interactions.

[4]The Standard Model incorporates an interesting property known as "symmetry" (another fundamental property of nature). The symmetry implies that the Lagrangian of these three interactions should be invariant under certain transformations. This study is done by gauge theory and the field is called gauge field and gauge bosons are the quantum of gauge field. In mathematical language, Standard Model is a non-abelian gauge theory with U(1)×SU(2)×SU(3) symmetry group with twelve gauge bosons- photon, three weak bosons and eight gluons [12; 13]. These group symmetries imply that the gauge bosons should be massless. But after the discovery of W and Z bosons as massive bosons in 1973, Higgs mechanism was adopted to explain the origin of mass.

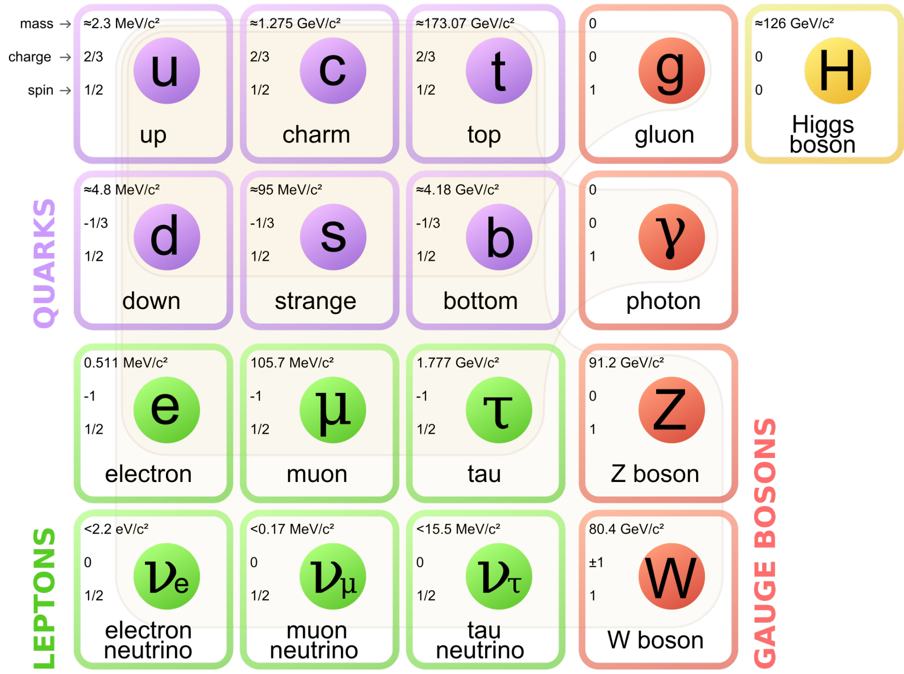

Figure 1.8: The fundamental particles of Standard Model and the force mediating bosons.

world from mid 20$^{\text{th}}$ century. The current formulation was finalized in the mid-1970s after experimental confirmation of the existence of quarks. It became a more trusted theory after the experimental observation of the top quark (1995), the τ neutrino (2000) and the Higgs boson (2012). Various properties of the W and Z bosons and weak neutral currents have been also predicted by SM with great accuracy. SM has successfully predicted many things which have been experimentally observed and it is believed to be theoretically self-consistent but it is unable to explain many phenomena and hence, not a complete theory of fundamental interactions. SM does not explain baryon asymmetry, excludes the theory of gravitation described by general relativity, does not incorporate neutrino oscillations and their non-zero masses etc. Abraham Pais and Sam Treiman first coined the term "Standard Model" in 1975. Our visible universe is composed of 12 *fermions* (spin $\frac{1}{2}$ particles) in which 6 are known as *quarks : up, down, charm, strange, top* and *bottom quarks* and remaining 6 are known as *leptons: electron, muon, tau* and *their associated neutrinos*. The charge, mass and other properties of these particles can be found in Figure 1.8.

1.5 Quantum Chromodynamics

Quantum Chromodynamics (QCD) is the theory of fundamental interactions between quarks and gluons, the basic building block of matter. It is a non-abelian gauge theory obeying SU(3) symmetry [13]. The *Color* charge is the QCD analog of electric charge. There are three color charges in QCD, namely, red, green, blue and three anti-color charges: anti-red, anti-green and anti-blue (Figure 1.9). Quarks and Gluons both carry color charges and hence the name of the theory is chromodynamics (*chromo* means color).

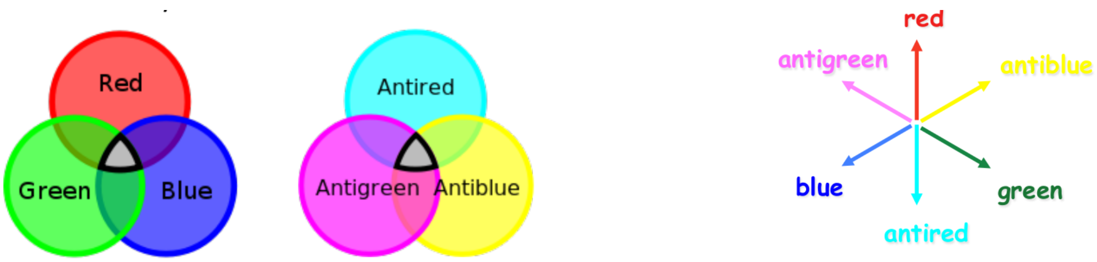

Figure 1.9: Types of color charges in QCD [14]

The force carrier of QCD are gluons. There are 8 gluons (based on all color combinations), 6 quarks and 6 anti-quarks in QCD (Figure 1.8). Both quarks and gluons are called partons. Hadrons, which are color singlet entities, are formed by either a quark-antiquark pair (mesons e.g. pion, kaon), or by combining three quarks (baryon e.g. proton, neutron), as illustrated in Figure1.10.

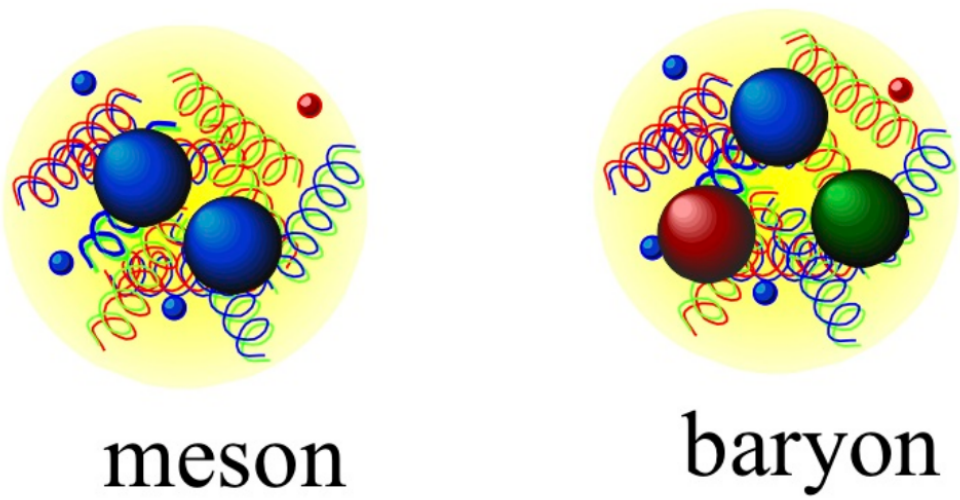

Figure 1.10: Quark compositions of meson and baryon [14]

The gauge invariant QCD Lagrangian, which governs, the dynamics of the quarks and gluons, is given by the following expression:

$$\mathcal{L}_{\text{QCD}} = \bar{\psi}_i(i(\gamma^\mu D_\mu)_{ij} - m\delta_{ij})\psi_j - \frac{1}{4}G^a_{\mu\nu}G^{\mu\nu}_a \tag{1.5}$$

where $\psi_i(x)$ is the space-time quark field, D_μ is the gauge covariant derivative, and γ^μ are Dirac matrices. $4G^a_{\mu\nu}$ is the gauge invariant gluon field strength tensor and is given by

$$G^a_{\mu\nu} = \partial_\mu A^a_\nu - \partial_\nu A^a_\mu + g f^{abc} A^b_\mu A^c_\nu \tag{1.6}$$

where A^a_ν are the gluon fields and are dynamical function of space-time. f_{abc} is the SU(3) structure constant, m and g are the quark mass and coupling, respectively.

1.5.1 Color confinement and Asymptotic freedom

Quarks contain fractional electric charge but Millikan's oil drop experiment gives negative result for fractional charges. The experimental fact that quarks (fractional charges) are not observed in isolation, was accommodated in the theory by postulating **quark confinement** or **color confinement** or simply **confinement**. Due to color confinement, quarks are never found in isolation. This observation is a direct consequence of the strong force between two color charges which increases as the distance between the color charges increases. As a result, a large amount of energy is required to increase the separation between the two quarks within a hadron. Eventually, instead of producing an isolated color charge, this energy produces a quark-antiquark pair and a new hadron is formed.

QCD has another remarkable property- **Asymptotic freedom**, which means that at very short distances or very large momentum transfer, the strong interaction strength decreases [15]. This implies that, the strong interaction coupling constant becomes very weak at high energy regime. This prediction of QCD was first discovered in the early 1970s by David Politzer and by Frank Wilczek and David Gross [16]. They were awarded the 2004 Nobel Prize in Physics for this spectacular theory.

The Asymptotic freedom can be understood from the expression of strong interaction coupling constant α_S, given by

$$\alpha_S(Q^2) = \frac{\alpha_S(\Lambda^2)}{1 + \alpha_S(\Lambda^2)\left(\frac{33-2N_f}{12\pi}\right)\ln\frac{Q^2}{\Lambda^2}} \tag{1.7}$$

where, Q is the momentum exchanged, Λ is the QCD length scaling parameter and N_f is the number of flavors. Figure 1.11 shows, the values of α_S calculated from QCD and obtained from different experiments.

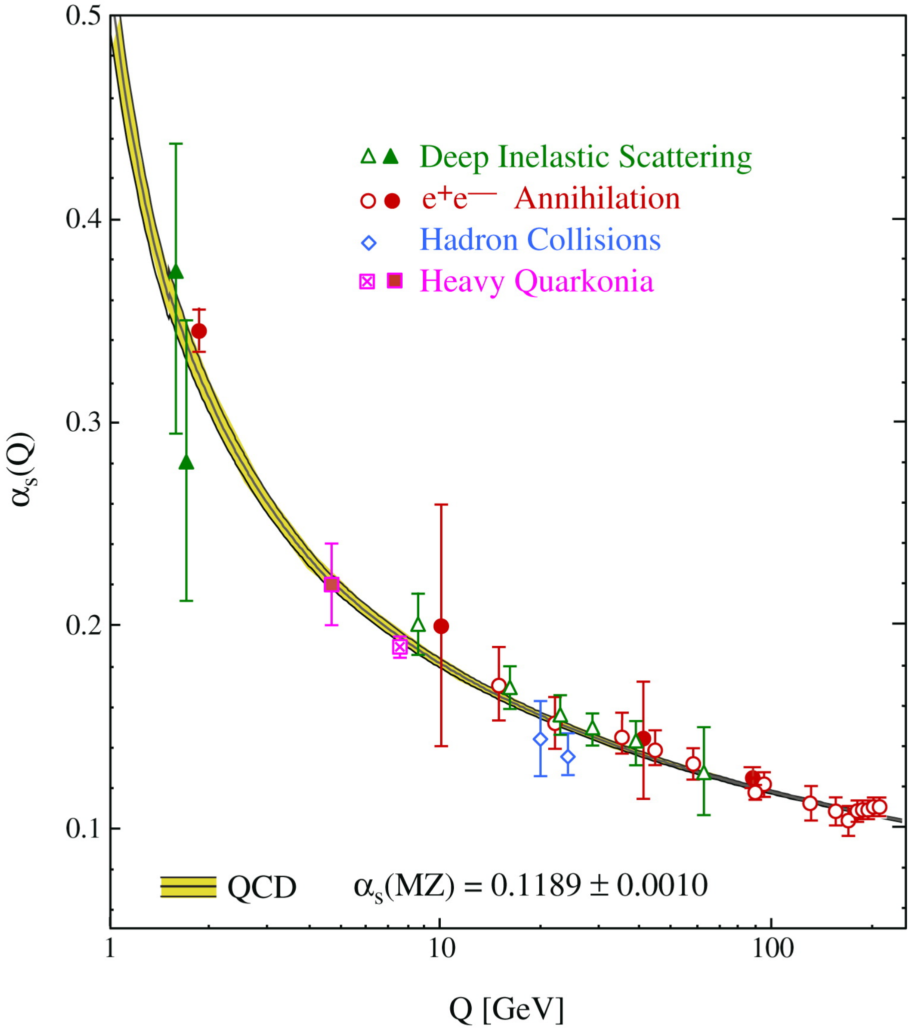

Figure 1.11: The summary of measurement of QCD coupling constant $\alpha_S(Q)$ as a function of the respective energy scale Q. Open and filled symbols indicate NLO and NNLO QCD calculations used in the respective analysis. The curves are the results obtained from the QCD predictions for the combined world average value of $\alpha_S(M_{Z^0})$, in 4-loop approximation and using 3-loop threshold matching at the heavy quark pole masses M_c = 1.5 GeV and M_b = 4.7 GeV [17].

1.5.2 Perturbative QCD

Perturbative QCD (pQCD) is a subfield of QCD in which study of strong interactions is carried out by using the fact that α_S is vanishingly small in very high energy regime or very short distance interactions [15]. Thus, one can apply perturbative calculations in the theory accurately in very high energy experiments. However, most strong interaction reactions can not be directly calculated with pQCD, because for low momentum transfer regions, $\alpha_S \rightarrow 1$ ($Q^2 \sim 1\text{GeV}/c^2$, $\Lambda^{-1}_{QCD} \sim 1fm$) where free quarks and free gluons can not be observed due to color confinement. In this scenario, one has to depend on non-perturbative calculations and modelling.

1.5.3 Lattice QCD

Lattice QCD is the most successful, well established non-perturbative theory which provides a mathematical framework to investigate the non-perturbative phenomena like confinement and the formation of the deconfined quark-gluon plasma state [18; 19]. Lattice QCD is a lattice gauge theory which is formulated on discrete set of space-time points called the 'lattice'. The continuum QCD can be recovered by considering the size of the lattice to be infinitely large and its sites to be infinitesimally close to each other. It is almost impossible to obtain perturbative solutions at low momentum transfer region due to the highly non-linear behavior of strong force. Lattice QCD formulation is discrete (not continuous) space-time and hence, introduces a cut-off in momentum. This momentum cut-off has an order $1/a$, where "a" represents the lattice spacing. This regularizes the theory and makes lattice QCD mathematically a well defined theory.

In Lattice QCD, lattice sites are the fields representing quarks and on the links connecting neighboring sites, the gluons fields are defined. The computational cost of numerical solutions increase drastically as the lattice space decreases. Therefore, to extrapolate results at "a = 0", repeated calculations are performed at different lattice spacing. The fastest supercomputers are required for numerical lattice QCD calculations using Monte Carlo methods. Many lattice QCD results have been successfully matched with results from many experiments. The determination of the proton mass theoretically with an error of less than two percent is one of the examples. The framework of Lattice QCD is based on Feynman's path integral approach. The use of path integral formulation of quantum field theory, enables to establish connection with statistical mechanics and thermodynamics. There are many interesting predictions by Lattice QCD calculations. One of the lattice QCD calculations predicts deconfinement of quarks from confined state to a deconfined state of quarks and gluons at high energies and at zero *baryon-chemical potential*[5] (μ_B). The QCD phase transition properties, at zero μ_B or vanishing baryon number, depend on the number of quark flavors and their masses (Figure 1.12).

Figure 1.12 shows the variation of energy density (ϵ/T^4) [6] with respect to the ratio of temperature i.e T/T_C for different quark flavors as predicted by Lattice QCD calculations. It can be seen that there is an abrupt jump in the value of ϵ/T^4 to $\sim$ 80 % of the ideal gas limit at a critical temperature T_c from the lower hadronic value and keeps rising until T $\sim$

[5]Baryon-chemical potential is change in energy of system when a baryon is added to it.

[6]It can be scaled with pressure too.

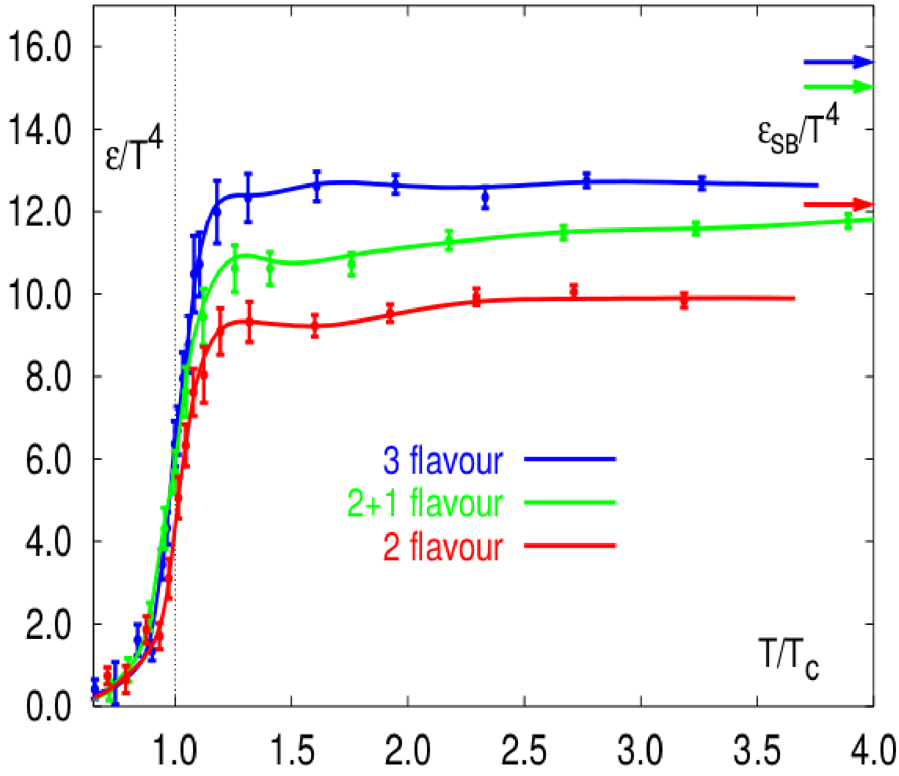

Figure 1.12: Variation of energy density scaled by T^4 as a function of temperature of hadronic matter at zero baryo-chemical potential, calculated from lattice QCD at finite temperature [19].

$2T_c$ where it saturates. The energy density is below the ideal gas limit at T_c which implies that there exists a substantial interaction among the quarks and gluons in that phase. The number of flavors taken in lattice calculation also affects the change in energy density. This clearly indicates the phase transition of hadronic colorless phase to a deconfined phase known as *Quark-Gluon Plasma* (QGP) phase. In QGP phase, degrees of freedom of quarks and gluons are basic degrees of freedom. The lattice QCD calculations predict the temperature and energy density corresponding to this hadronic to QGP phase transition to be ~ 170 MeV and ~ 0.7 GeV/fm^3, respectively. The following section briefly describes the experimental formation of such a conjectured state of matter.

1.6 Heavy Ion Collisions and Quark-Gluon Plasma

The running QCD coupling constant $\alpha_S(Q)$ (Figure 1.11) as a function of momentum transfer, makes QCD a very complicated as well as an interesting theory. The asymptotic freedom property of QCD, predicts that at very large momentum exchange and at very short distances, quarks and gluons interact very weakly with each other. Lattice QCD predicts a phase transition from hadronic state to almost free quark-gluon state or quark-gluon plasma (QGP), if the temperature and energy density of the system are ~ 170 MeV and ~ 0.7 GeV/fm^3, respectively (Figure 1.13). Additionally, Big-Bang theory also predicts the existence of QGP after few micro seconds of the Big Bang. It is also believed that QGP can be now be found in the core of neutron stars due to extreme densities of nuclear matter.

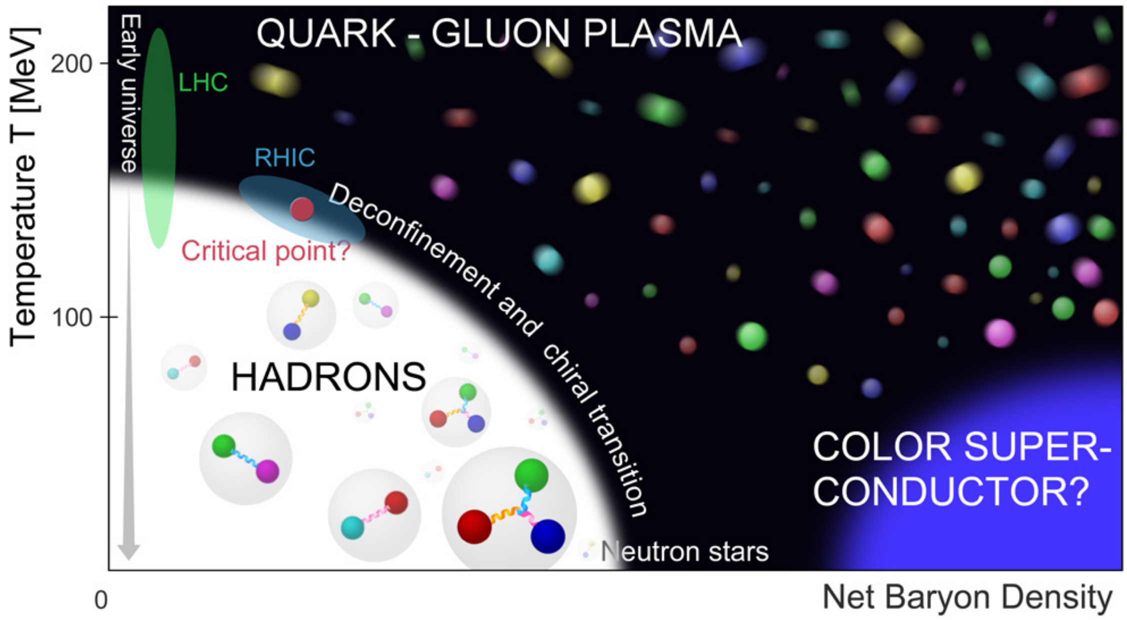

Figure 1.13: Lattice QCD Phase Diagram [20].

Therefore, the study of this so called 'novel state of matter', i.e. QGP, can help us to understand the evolution of universe as well as to understand the matter at extreme densities and temperatures. As it is not yet possible to go back in time or inside the neutron star to study such an exotic state, one must investigate to create such conditions in laboratory. Huge particle accelerators and colliders have been constructed to collide heavy ions experimentally to produce and study the QGP state. The *Relativistic Heavy Ion Collider (RHIC)* and the *Large Hadron Collider (LHC)* are the two most powerful particle colliders in the world. The collider experiment will be discussed in Chapter 3. The heavy ion particle colliders basically collide heavy nuclei like Gold (Au), Lead (Pb) at relativistic energies. In heavy ion collisions, two heavy nuclei like Pb^{82+} are allowed to collide with each other at ultra-relativistic speed. A nuclei is made of nucleons i.e. protons and neutrons which contain quarks and gluons. In a hadron, quarks are bound due to strong interaction by exchanging gluons between them. However, when nucleon density becomes very high, the hadrons start to penetrate into each other and the quarks inside hadrons loose their identity. Due to screening of color charge, the quarks inside hadrons do not remain confined inside hadrons and become free to move inside nuclear radius rather than the nucleonic radius. Similar phenomena happen when two nuclei collide head-on with ulta-relativistic energies. The kinetic energy of the nucleus gets transformed into heat energy due to inelastic collisions and the hadrons melt. The deconfinement of quarks takes place and a very hot and dense soup of quarks and gluons is formed. This soup or new state of matter is called Quark-Gluon Plasma (QGP).

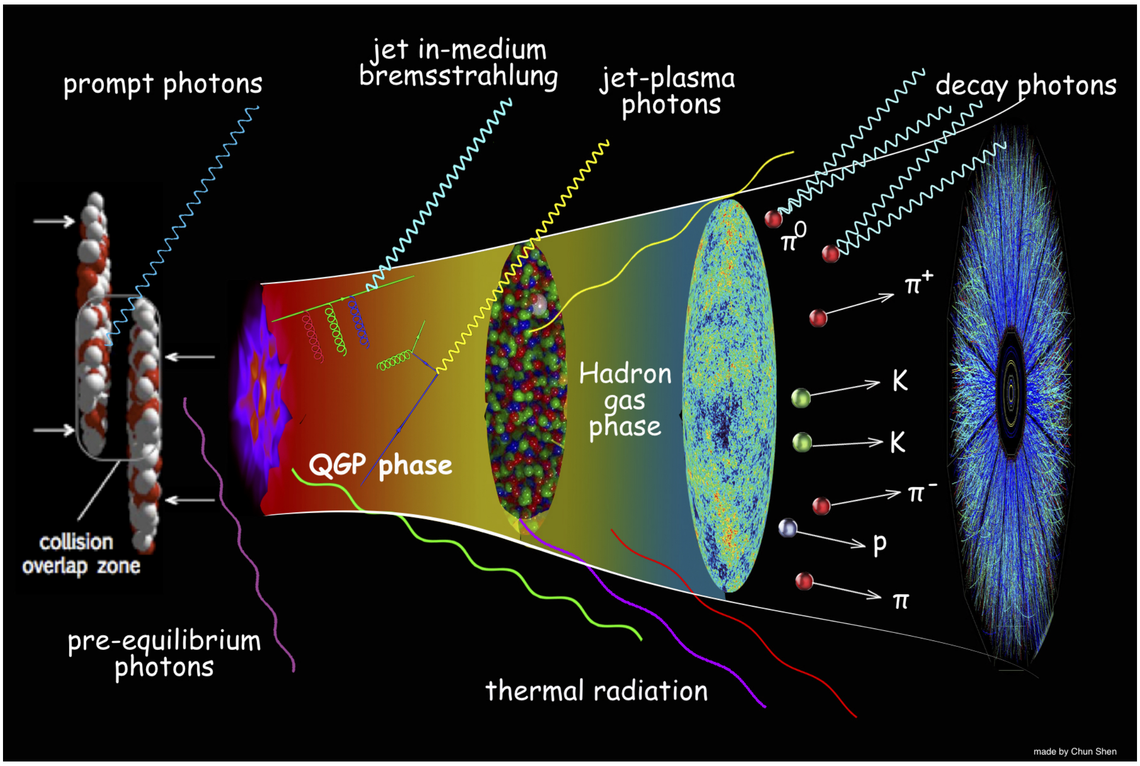

Figure 1.14: Stages of relativistic heavy-ion collision [21].

Figure 1.14 shows the various stages of heavy-ion collisions. It is shown that two Lorentz contracted nuclei in center of mass frame approach each other at ultra-relativistic speed. After collision, nuclei lose their kinetic energy followed by the formation of a very hot and dense fireball of quarks and gluons for a very short period of time. As the fireball starts expanding due to its inner pressure, the temperature of fireball starts decreasing. As the temperature decreases, free quarks start to combine in the form of doublets (meson) and triplets (baryon) due to strong field of gluons, and thousands of new particles are produced. The fireball continues expanding until the energy density becomes too low to produce new particles. This is called **chemical freeze out**. After chemical freeze out, fireball still continues to expand and the produced particles interact with each other via elastic scattering. When mean free path of particles become equivalent to the size

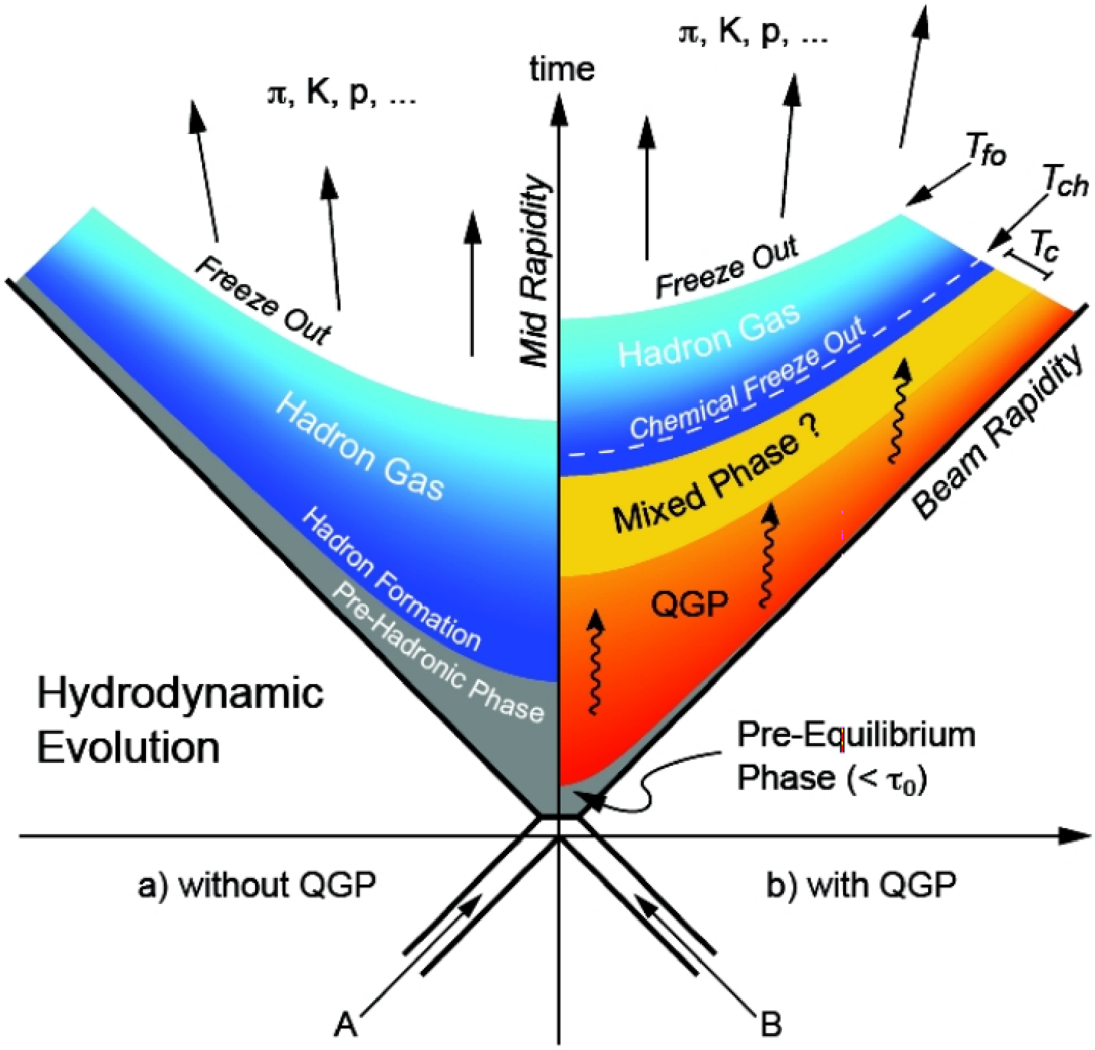

Figure 1.15: The space-time diagram for the evolution of matter produced in relativistic heavy-ion collisions [22].

of fireball, elastic scattering of particles stop.This is called **kinetic or thermal freeze out**. A space-time diagram for the evolution of matter produced in relativistic heavy-ion collisions is shown in Figure 1.15. Particles move straight after kinetic freeze out and most of them decay due to their short lifetime. Primarily, the pions, kaons, electrons and protons get detected by the detectors. The properties of these detected particles are studied using the information from various detectors, to study the properties of the QGP. The QGP or system produced after heavy ion collisions can not be studied directly due to its small size and lifetime. Many signatures are proposed to probe the QGP. These signatures leave footprints of the early stage after collisions even after hadronization, and are sensitive to the dynamics of QGP. Some of the signatures are discussed briefly in the following sections.

1.7 Elliptic Flow

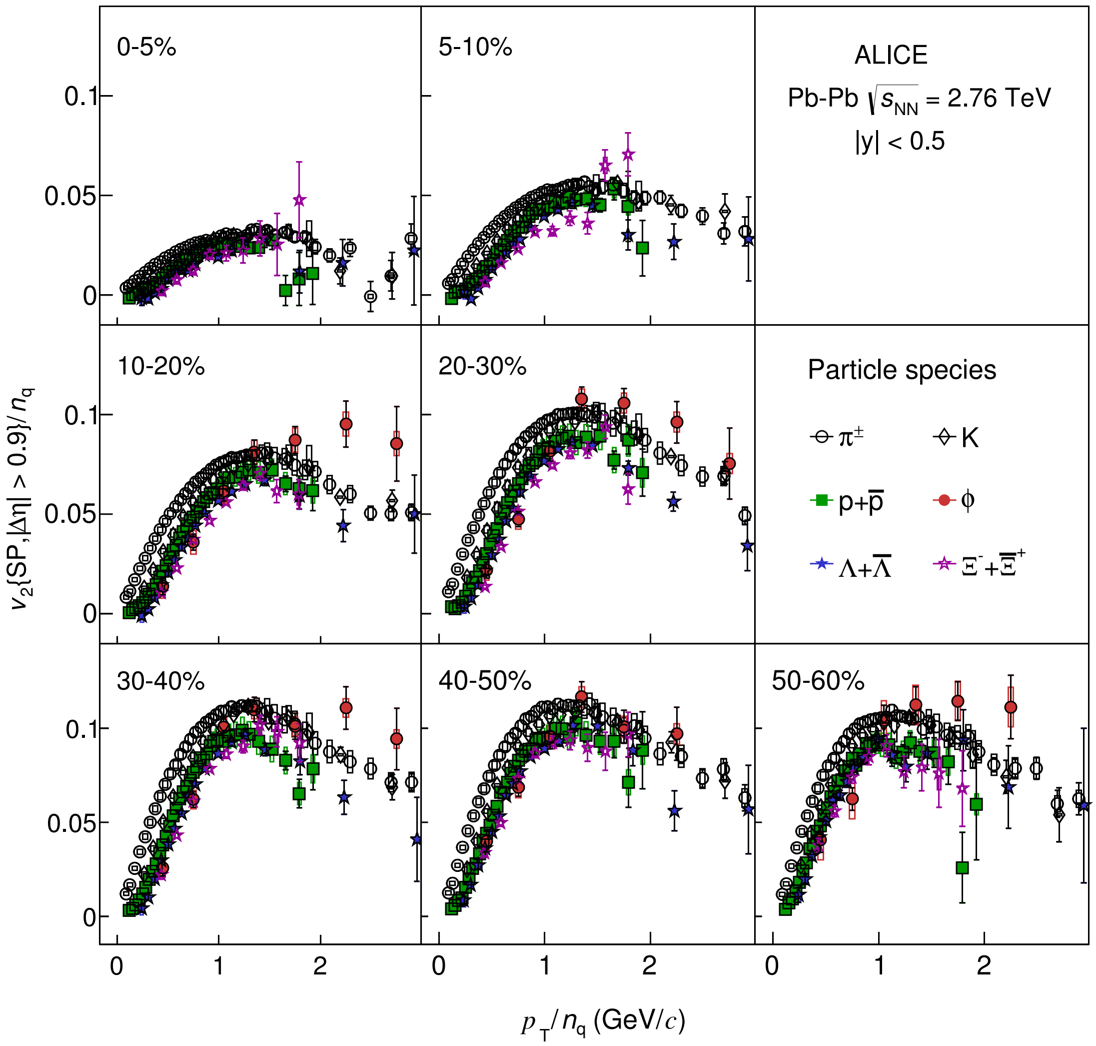

Figure 1.16: v_2/n_q as a function of p_T/n_q for identified hadrons in Pb−Pb collisions at $\sqrt{s_{\rm NN}}$= 2.76 TeV for different centrality classes [23].

In the heavy-ion collision process, the medium produced undergoes hydrodynamical expansion due to large pressure gradient. The medium constituents try to achieve local thermal equilibrium by interacting among themselves. In non-central collisions where the impact parameter has non-zero value and the shape of the overlapping region of the two nuclei represents an ellipsoid, a collective motion is built up by the conversion of spatial anisotropy in the reaction zone to momentum anisotropy in the transverse momentum space after sufficient interaction among the partons. The pressure gradient is more along the minor axis than major axis and during expansion, the reaction zone attains symmetry. The hadrons contain the information about initial stages and it is reflected in the transverse momentum spectra of the produced particles. Due to self-quenching nature of anisotropic flow, any non-trivial result is useful and can be a unique tool to probe the medium produced in early stage. The anisotropic flow is measured experimentally by using the transverse momentum distribution of produced particles with respect to reaction plane[7]. The momentum anisotropy can be written in terms of Fourier coefficient of triple differential invariant distribution of produced particles:

$$E\frac{d^3N}{d^3p} = \frac{1}{2\pi}\frac{d^2N}{p_T dp_T dy}[1 + 2\sum_n v_n cos[n(\phi - \Psi_n)]], n = 1, 2, 3, ... \quad (1.8)$$

where v_n and Ψ_n represent the flow harmonics and angle of the initial state spatial plane of symmetry, respectively. The first right hand side term of the equation is the radial flow. Radial flow is isotropic in nature. The first and second flow harmonics, v_1 and v_2, are referred as directed flow and elliptic flow, respectively. v_2 is believed to be sensitive to early stage evolution, freeze-out conditions and equation of state of the medium formed after heavy ion collisions. v_2 can also be theoretically connected with shear viscosity to entropy ratio η/s from ADS/CFT theory and hence, can inform about the bulk properties of the medium created. The first sign of collectivity in heavy ion collisions was observed at AGS and SPS energies followed by measurements at RHIC energies. The results from ALICE collaboration at the LHC for Pb−Pb collisions at $\sqrt{s_{\rm NN}}$= 2.76 TeV are shown in Figure 1.16. The most interesting result was the scaling of v_2 with number of constituent quarks. This observation implied that the collective phenomena is developed at the partonic level. The comparison of these results with various theoretical models which included hydrodynamical evolution of the medium formed suggested the formation of an almost perfect fluid with strongly interacting matter. The study of v_2 at the LHC energies is expected to provide a more precise measurement of η/s, due to higher multiplicity, which will be helpful to understand the contribution from partonic fluid. The measurement of other higher order harmonics like v_3, v_4 and v_5 has also been useful to put constraints on theoretical models and has helped to understand the matter created in heavy-ion collisions.

1.8 Strangeness Enhancement

The strangeness enhancement in heavy-ion collisions has been predicted as one of the key observables for the existence of the QGP as the initial colliding nuclei do not have strange quarks [24]. This means strange quarks are produced in the hot QCD matter in such collisions. The threshold energy for production of strange hadrons is ~300−400

[7] The reaction plane is the plane which is spanned by impact parameter and beam direction

MeV while the threshold for anti-baryon is smaller. The QGP lifetime is small for weak decays and once produced, a strange quark can only be destroyed by annihilating with an anti-strange quark. Thus, the number of strange particles observed can be expected to be a good probe of QGP evolution. To know about the strangeness enhancement, study and comparison of the abundance of strangeness between plasma and hadronic phase is necessary. The high rate of $gg \rightarrow s\bar{s}$ (called flavor creation) contributes to the strangeness enhancement because of high gluon density. These processes have very small cross-section in p−p collisions and are not present in the hadronic phase.

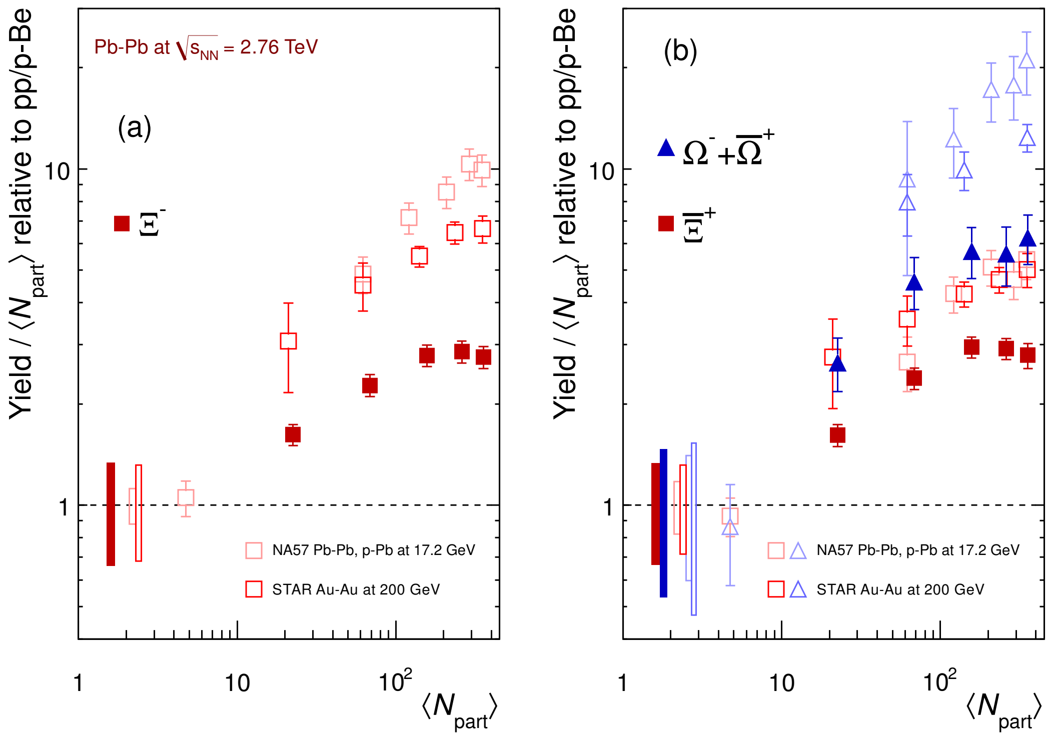

Figure 1.17: Strangeness enhancement as a function of the mean number of participants ($<N_{part}>$). The ALICE, results have been shown by full symbols while RHIC and SPS results are shown by open symbols [24].

Figure 1.17 shows the measurement of multi-strange hadron production as a function of the mean number of participants ($<N_{part}>$) in Pb−Pb collisions at $\sqrt{s_{\rm NN}}$= 2.76 TeV as measured by ALICE experiment. The ALICE results are also compared with STAR results for Au−Au collisions data at $\sqrt{s_{\rm NN}}$= 200 GeV and with NA57 results for Pb−Pb collisions at $\sqrt{s_{\rm NN}}$= 17.2 GeV. It has been observed that enhancement is more for particles with higher strange quark content which is consistent with previous measurements at RHIC and SPS energies. This observation suggested the presence of large number of $s\bar{s}$ quarks inside the hot and dense partonic medium. Figure 1.17 also shows the reduction in strangeness enhancement with increasing collision energies. This can be understood by statistical hadronization models by taking into account the strangeness conservation in canonical ensemble. In smaller system like p−p where charged-particle multiplicity is lower, the quantum conservation laws including strangeness have to be applied locally on an event-by-event basis. On the other hand, for high charged particle multiplicity systems like the one produced in Pb−Pb collisions, the conservation laws can be applied on an average basis and a grand canonical formalism can be used for the thermodynamical description. The phase space available for particle production is reduced by the quantum number conservation laws and these laws also tend to decrease the canonical suppression factor with increasing center-of-mass energy of the collision.

1.9 Jet Quenching and Partonic Energy Loss

In the relativistic high energy collisions, the initial hard scattering among the partons results in the production of two or more outgoing final state partons. The produced partons split into quark-antiquark pairs and/or radiate gluons. At the end, these produced partons fragment into a set of collimated spray of hadrons known as *jets*. The production and propagation of these jets are different in heavy-ion collisions than those in elementary collisions (like p−p) due to the formation and presence of hot and dense medium in heavy-ion collisions. The partons traversing through the medium loose their energy in medium via gluon radiation. Consequently, these partons in colored dense medium can fragment into hadrons whose transverse momentum is significantly reduced. This phenomenon is known as *jet quenching* which is a final state effect. Jet quenching can provide information like diffusion constant and transport coefficient of the medium produced by collisions. The first experimental evidence of jet quenching was observed in the di-hadron correlation study in azimuthal plane at RHIC in Au−Au collisions at $\sqrt{s_{\rm NN}}$= 200 GeV [25]. Figure 1.18 shows the experimental results from two-particle correlation study in p−p and Pb−Pb collisions at $\sqrt{s_{\rm NN}}$= 2.76 TeV as measured by ALICE experiment [26]. The measured correlation is shown as a function of azimuthal angle difference, $\Delta\phi$ ($\Delta\phi = \phi_{associated} - \phi_{trigger}$) for a high p_T trigger particles with respect to low p_T associated particles. The clearly visible double peak of the correlation function, in p−p and peripheral Pb−Pb collisions where no dense medium is assumed to be formed, is consistent with a di-jet event. However, in central Pb−Pb collisions, the away side peak is seen to be strongly suppressed.

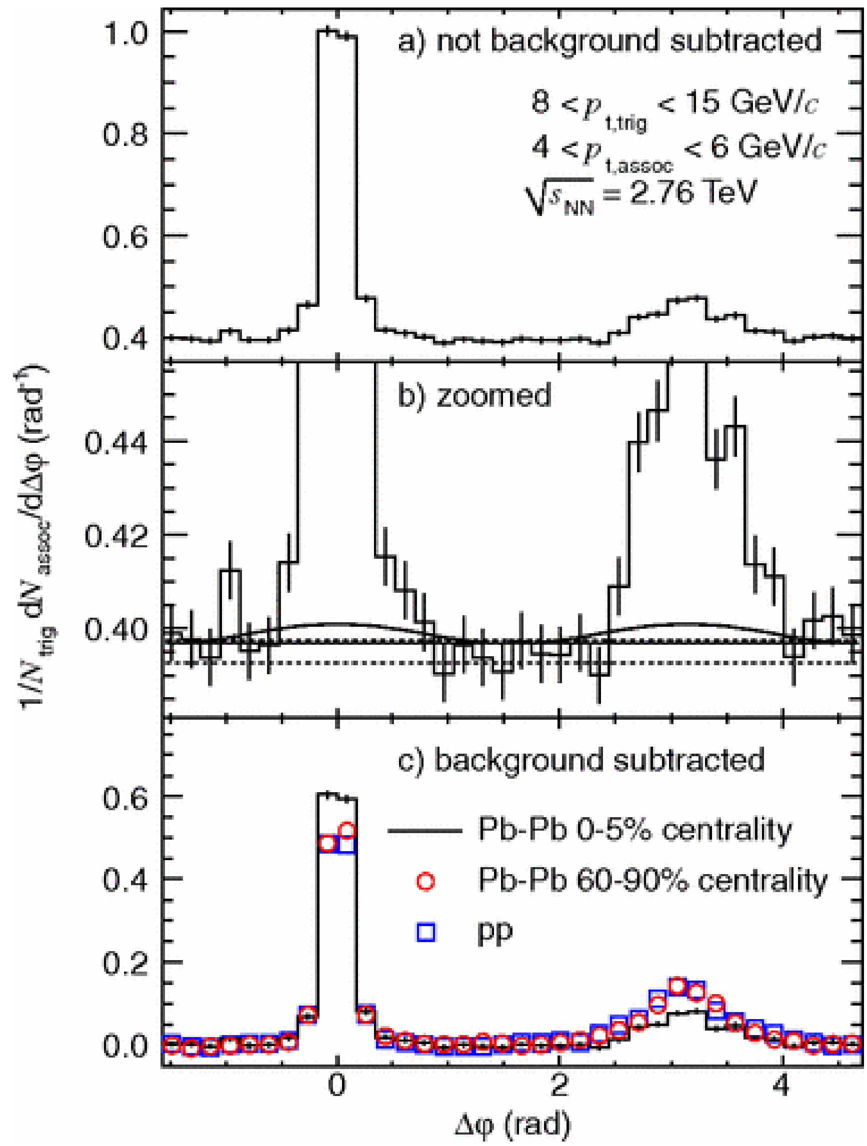

Figure 1.18: (**Upper panel**) The azimuthal correlation (background not subtracted) for central Pb−Pb collisions at $\sqrt{s_{\rm NN}}$= 2.76 TeV as measured by ALICE experiment. The middle panel shows the zoomed version of the same. (**Lower panel**) Comparison of the background subtracted results from central collisions to peripheral Pb−Pb collisions and p−p collisions at 2.76 TeV measured by ALICE experiment [26].

This can be attributed to the final state effect of the energy loss of the jet while passing through the medium.

The measurement of nuclear modification factor also provides a useful way of estimating the effects of hot and dense medium created in heavy ion collisions compared to that created in elementary collisions. The nuclear modification factor is defined as,

$$R_{AA}(p_T) = \frac{(1/N_{evt}^{AA})d^2N_{\rm ch}^{AA}/d\eta dp_T}{\langle N_{\rm coll}\rangle(1/N_{evt}^{pp})d^2N_{\rm ch}^{pp}/d\eta dp_T}, \tag{1.9}$$

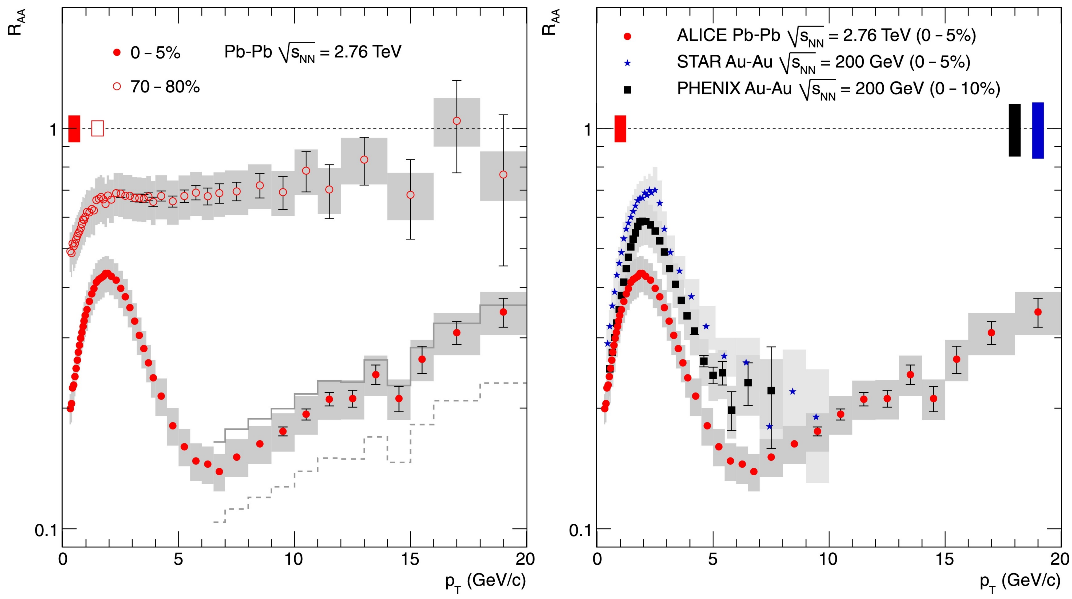

Figure 1.19: (**Left panel**) R_{AA} in central (0-5%) and peripheral (70-80%) Pb−Pb collisions at $\sqrt{s_{NN}}$ = 2.76 TeV as measured by ALICE experiment. (**Right panel**) Comparison of R_{AA} in central Pb−Pb collisions at the LHC to measurements at $\sqrt{s_{NN}}$ = 200 GeV by the PHENIX and STAR experiments at the RHIC [27].

where $\langle N_{\rm coll} \rangle$ is the number of binary nucleon-nucleon collisions, $d^2N_{\rm ch}^{AA}/d\eta dp_T$ is the differential yield of charged particles per event in nucleus-nucleus (A−A) collisions and $d^2N_{\rm ch}^{pp}/d\eta dp_T$ is the differential cross section of charged particle production in p−p collisions. The value of R_{AA} is expected to be one in the absence of any medium effect in A−A collisions (or nuclear collisions were mere superposition of nucleon-nucleon collisions). Figure 1.19 shows the measurement of R_{AA} as a function of transverse momentum in Pb−Pb collisions at $\sqrt{s_{\rm NN}}$= 2.76 TeV as measured by ALICE experiment [27]. The figure shows a clear suppression of high p_T hadrons in central Pb−Pb collision compared to the peripheral collisions. This clearly indicates the loss of energy of hard-scattered partons due to interaction with colored dense medium produced in heavy-ion collisions. The ALICE results are also compared (right panel) to the previous measurements at the RHIC energies. It can be seen that the suppression is more at the LHC energies compared to that at the RHIC energies.

1.10 Direct Photons

Direct photons are photons which do not originate from hadronic decays. As they are produced in all stages of the heavy ion collisions and leave the fireball unaffected, they act as an excellent tool to study the medium created in such collisions. The two types of

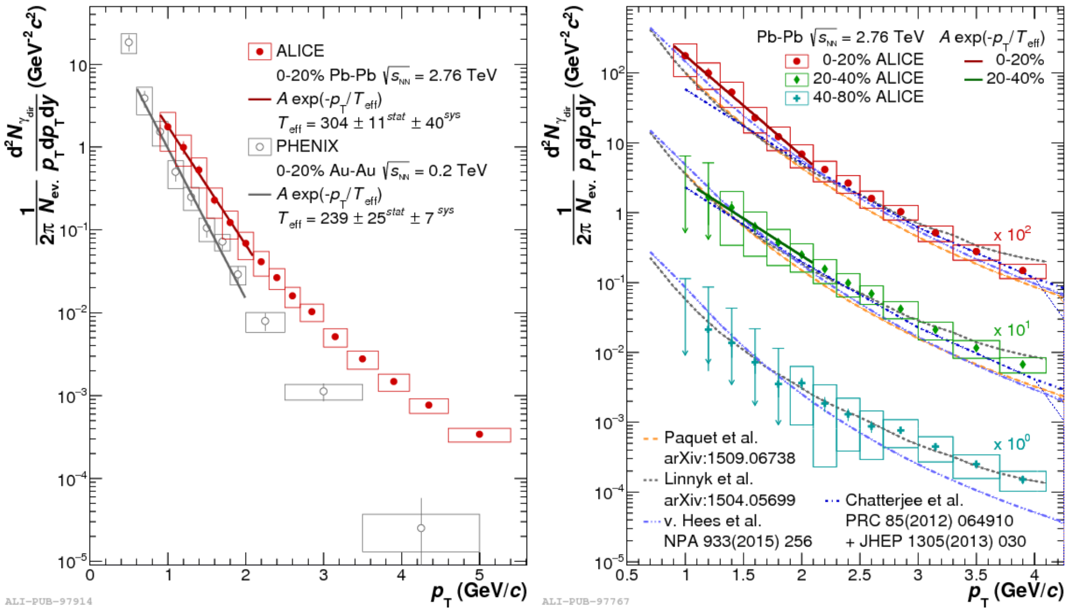

Figure 1.20: (**Left panel**) The direct photon spectrum (with exponential fit) for 0-20% central events in Pb−Pb collisions at $\sqrt{s_{\mathrm{NN}}}$=2.76 TeV ALICE experiment and in Au−Au collisions at $\sqrt{s_{\mathrm{NN}}}$=200 GeV PHENIX. (**Right panel**) The direct photon spectra for different centrality classes are compared to theoretical calculations from different models. The spectra are scaled appropriately for visibility [28; 29].

direct photons often considered, are prompt photons and thermal photons. The former is produced in initial hard partonic scatterings and provides information on distributions of partons inside nuclei. The thermal photons are produced by the QGP and are also emitted by the hadronic matter throughout the evolution of the fireball. They carry information about the temperature, radial flow and the space-time evolution of the system. The low p_T ($p_T < 4$ GeV/c) spectrum of the direct photons predominantly contains information about the temperature of the medium created. The direct photon spectrum for 0-20% most central Pb−Pb events at $\sqrt{s_{\mathrm{NN}}}$= 2.76 TeV and Au−Au events at $\sqrt{s_{\mathrm{NN}}}$= 200 GeV are shown in the left panel of Figure 1.20. In order to extract the respective slope parameters, both spectra are fitted with an exponential function at low p_{T} [28; 29]. The fit to the spectrum from Au−Au collisions data gives a slope parameter of $\mathrm{T_{eff}}$ = 239 ± 25 ± 7 MeV, while the ALICE Pb−Pb collisions data have a larger slope parameter of $\mathrm{T_{eff}}$ = 304 ± 11 ± 40 MeV which is consistent with a larger initial temperature of the medium at the higher centre of mass energy.

1.11 Femtoscopy

One requires a detailed understanding of the collision dynamics in order to obtain the information on bulk matter produced in heavy ion collisions. Due to the small size of the system produced and for its transient nature, it becomes difficult to perform direct measurement of the size of the system and the time for which it exists. The femtoscopic correlations arise from Bose-Einstein correlation (for identical bosons only) and final state interaction (FSI). The measured femtoscopic correlation functions contain the contribution throughout the fireball expansion. The technique of obtaining femtoscopic correlations between the emitted particles provides us a method to estimate the size and lifetime of the system. The method primarily involves calculating the correlation function of a pair of final state particles at small relative momentum. The pairs can be chosen to be identical particles or non-identical particles depending upon the physics message one wants to extract from the correlation. This thesis reports about the pion-kaon femtoscopic studies

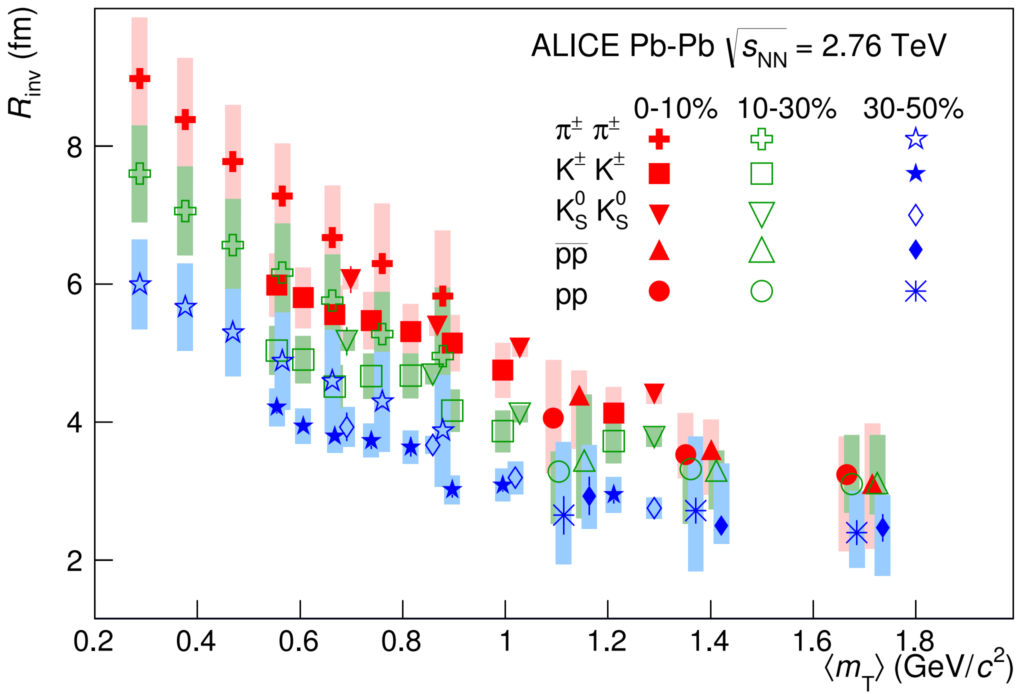

Figure 1.21: The variation of source size (R_{inv}) as a function of average transverse mass for three centrality classes for different particle pairs in Pb−Pb collisions at $\sqrt{s_{\text{NN}}}$=2.76 TeV measured by ALICE experiment [30].

in Pb−Pb collisions at $\sqrt{s_{\text{NN}}}$=2.76 TeV. Therefore, the theoretical formalism, experimental methods with particular emphasis on non-identical particle femtoscopy is provided in Chapter 2. Figure 1.21 shows the variation of source radii extracted from identical particle femtoscopy studies as a function of average transverse mass (m_T) in Pb−Pb collisions at $\sqrt{s_{\rm NN}}$=2.76 TeV as measured by ALICE experiment [30]. A gradual decrease of source radii is observed with an increase of m_T which indicated the presence of collectivity.

1.12 Scope and organisation of the thesis

The aim of this thesis is to study the femtoscopic correlation between non-identical charged particles produced in relativistic heavy-ion collisions. This study investigates the pion-kaon femtoscopic correlation in Pb−Pb collisions at $\sqrt{s_{\rm NN}}$= 2.76 TeV using ALICE detector. The study provides a unique opportunity to measure the convoluted source size of the pion-kaon system at low relative momenta and emission asymmetries between the produced particles of different mass. The Chapter 2 of the thesis provides an overview of the formalism of femtoscopic measurements focusing on non-identical particle femtoscopy followed by a discussion on the Large Hadron Collider (LHC) collider facility and the ALICE (A Large Ion Collider Experiment) experiment in Chapter 3. In Chapter 4, the details of the experimental data analysis is reported. The experimental results are discussed in Chapter 5 while the investigation is summarized in Chapter 6.

Chapter 2

Two particle Femtoscopic Correlation

"I have tried to read philosophers of all ages and have found many illuminating ideas but no steady progress toward deeper knowledge and understanding. Science, however, gives me the feeling of steady progress: I am convinced that theoretical physics is actual philosophy. It has revolutionized fundamental concepts, e.g., about space and time (relativity), about causality (quantum theory), and about substance and matter (atomistics), and it has taught us new methods of thinking (complementarity) which are applicable far beyond physics." – Max Born

Abstract: This chapter describes the theoretical aspects of femtoscopy. The basic idea of femtoscopic correlations have been discussed with a greater emphasis on non-identical particle correlation.

2.1 Origin of Femtoscopy

The main goal of studying nucleus-nucleus collisions at ultra-relativistic is to characterize the dynamical processes by which QGP like system is produced and to study the properties this hot and dense matter exhibits. However, experimentally, it is very challenging to study the QCD matter at high temperature and density because of very short spatio-temporal dimensions of the system produced. The tool to characterize the spatio-temporal properties of the collision region at femtometer scale is know as $Femtoscopy$ and this study is essential to address the dynamical equilibration process through which the QCD matter proceeds. Addressing the bulk matter properties requires a very good understanding of the dynamics and chemistry of the collision, which can only be acquired by coordinated analysis of experimental data and theory. Because the correlations from identity interference or either interactions are stronger for smaller space-time separation, correlations of two final-state particles at small relative momentum are the best source to provide the direct link to the size and lifetime of the smaller system.

The two particles interference from a chaotic source was first applied by Hanburry-Brown and Twiss where photons were exploited to determine the source size of stars [31; 32]. In 1960, Goldhaber, Lee and Pais showed that the correlations of identical pions are sensitive to source dimensions in $p-\bar{p}$ collisions [33]. These methods were refined by Kopylove, Pedgoretsky, Koonin and Gyulassy and it was shown that other class of correlations such as Strong and Coulomb interactions are useful in source size measurements. Although the theory is very different, still Heavy-Ion community often uses *HBT (Hanbury-Brown and Twiss Interferometry)* for analysis related to size and shape of the source, in reference to Hanbury-Brown and Twiss's original work with photons.

2.2 Basic Formalism

The femtoscopic studies are generally done using momentum correlation functions between two or more particles with small relative momenta. The general two-particle correlation function is defined as:

$$C(\mathbf{p_a}, \mathbf{p_b}) = \frac{P_2(\mathbf{p}_a, \mathbf{p}_b)}{P_1(\mathbf{p}_a)P_1(\mathbf{p}_b)} \tag{2.1}$$

where P_2 is the conditional probability to observe a particle with momentum $\mathbf{p}_b$ if a particle of momentum $\mathbf{p}_a$ was also observed, while P_1 is the probability of observing a particle with a given momentum.

In femtoscopy, two-particle correlation function is constructed as:

$$\begin{aligned} C^{ab}(\mathbf{P}, \mathbf{q}) &= \frac{dN^{ab}/(d^3p_a d^3p_b)}{(dN^a/d^3p_a)(dN^b/d^3p_b)}, \\ P &\equiv p_a + p_b, \ \ q^\mu = \frac{(p_a - p_b)^\mu}{2} - \frac{(p_a - p_b)\cdot P}{2P^2}P^\mu . \end{aligned} \tag{2.2}$$

where numerator is the measured experimental two-particle inclusive spectra while denominator is the single particle inclusive spectra. There are two equations which relate measured correlation function to the space-time emission function $s(p, x)$. The first form is written as:

$$C^{ab}(\mathbf{P}, \mathbf{q}) = \frac{\int d^4x_a d^4x_b s_a(p_a, x_a) s_b(p_b, x_b) |\Psi(\mathbf{q}^*, \mathbf{r}^*)|^2}{\int d^4x_a s_a(p_a, x_a) \int d^4x_b s_b(p_b, x_b)} . \tag{2.3}$$

In the above equation, $s(p, x)$ describes the probability of emitting a particle with momentum p from a space time point x and contains all the space-time information about

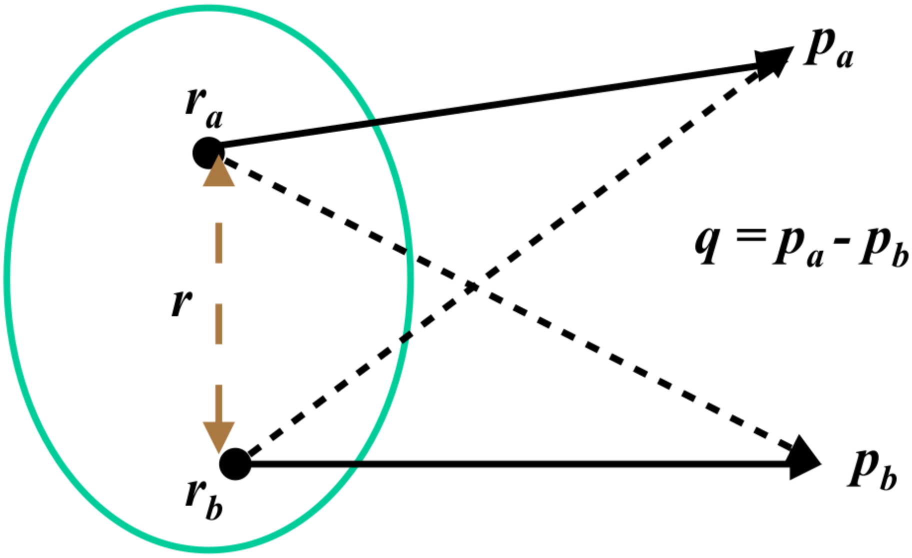

Figure 2.1: A schematic of pair emission from a source

emission source. Superscript "*" denotes the quantities in the center of mass frame where pair momentum $\mathbf{P} = 0$. In calculations of correlation functions, $|\Psi|^2$ serves as weight and the source function s_a is evaluated at the momentum

$$\bar{\mathbf{p}}_a = m_a\mathbf{P}/(m_a + m_b), \bar{p}_a^0 = E_a(\bar{\mathbf{p}}_a). \tag{2.4}$$

The second equation is,

$$\begin{aligned} C^{ab}(\mathbf{P}, \mathbf{q}) - 1 &= \int d^3r^* \mathcal{S}_\mathbf{P}(\mathbf{r}^*) \left[|\Psi(\mathbf{q}^*, \mathbf{r}^*)|^2 - 1\right], \\ \mathcal{S}_\mathbf{P}(\mathbf{r}^*) &\equiv \frac{\int d^4x_a d^4x_b s_a(\bar{p}_a, x_a) s_b(\bar{p}_b, x_b) \delta\left(\mathbf{r}^* - \mathbf{x}_a^* + \mathbf{x}_b^*\right)}{\int d^4x_a d^4x_b s_a(\bar{p}_a, x_a) s_b(\bar{p}_b, x_b)}. \end{aligned} \tag{2.5}$$

In this form, $|\Psi|^2$ is a kernel using which one can transform from coordinate-space basis to the relative-momentum basis. The function $\mathcal{S}_\mathbf{P}(\mathbf{r}^*)$ represents the distribution of particles with similar velocities and total momentum pair $\mathbf{P}$ as they move in their asymptotic state. This means correlations address the dimensions of the "region of homogeneity" instead of measuring the size of entire source. In the case of central collisions where collective expansion of the produced matter is strong, the size of the homogeneity region is significantly smaller than the entire source size.

The equations 2.3 and 2.5 are based on some assumptions which will be discussed in the following [34]. For single particle emission, in terms of T-matrix elements,

$$E\frac{dN}{d^3p} = \int d^4x\, s(p,x) = \sum_{F^*} |\int d^4x T_{F^*}(x) e^{-ip\cdot x}|^2, \tag{2.6}$$

$$s(p,x) = \sum_{F^*} \int d^4\delta x T^*_{F^*}(x+\delta x/2) T_{F^*}(x-\delta x/2) e^{ip\cdot\delta x}. \tag{2.7}$$

where F^* represents the state of all other particles in the system. All other interactions as well as residual system are incorporated into the T matrix.

The first assumption in femtoscopy is that higher order symmetrization and anti-symmetrization is neglected. equation 2.6 indicates that last interaction with the source of all particles with momentum p had at some point x, which is indeed the case for distinguishable particles. Hence equation 2.6 does not represent an assumption for distinguishable particles. However, if there is more than one particle of a type a ($N_a > 1$), then one must consider $T_a(x_1 \cdots x_{N_a})$. In this case, the evolution matrix is not just a phase factor but also includes $N_a!$ interference terms. To obtain single-particle probability, one must integrate over the N_a - 1 momenta.

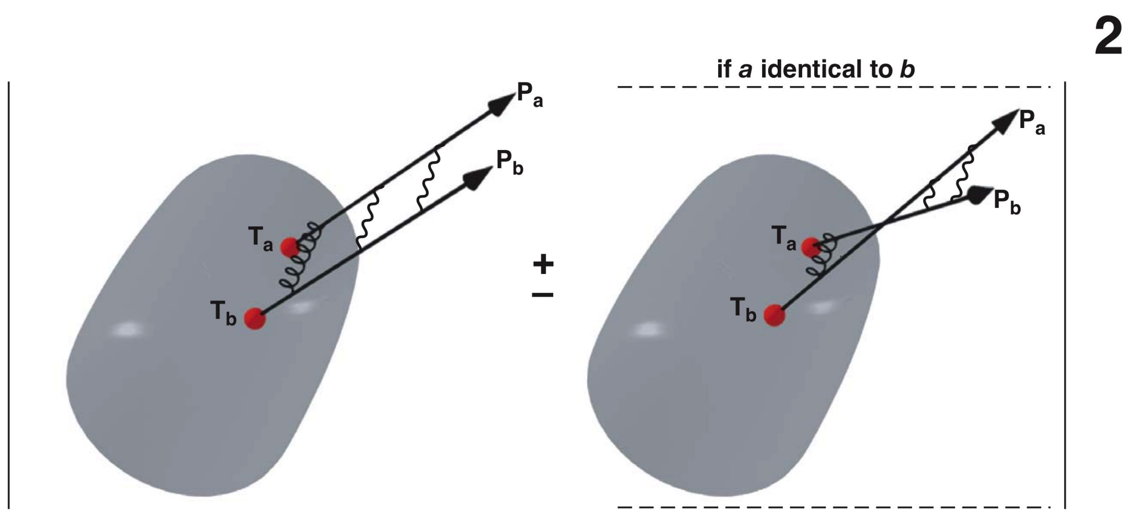

Figure 2.2: A schematic diagram to represent the emission amplitude for two independently emitted particles from grey-shaded source region. The particles interact with each other in final states [34].

The second assumption is that the particle emission process is independent for each particle produced. Two-particle matrix is required to factorize in equation 2.6, $T_{F^{**}}(x_a, x_b) = T_{F^*_a}(x_a)T_{F^*_b}(x_b)$, i.e., that the emission is independent. The two-particle evolution operator factorizes into a center-of-mass and a relative operator when the multi-particle symmetrization is neglected. In the case of identical particles $U = e^{iP\cdot(x_a+x_b)/2}(u_{q^*}(x_a^*-x_b^*)\pm(u_{q^*}(x_b^*-x_a^*))/\sqrt{2}$ and for non-identical particles $U(x_a,x_b;p_a,p_b) = u_{q^*}(x_a^*-x_b^*)e^{iP\cdot(E_a^*x_a/M_{\rm inv}+E_b^*x_b/{\rm Minv})}$ (illustrated in Figure 2.2). Then, the two-particle probability, in term terms of single-particle source functions, can be expressed as:

$$E_aE_b\frac{dN_{ab}}{d^3p_ad^3p_b} = \int d^4x_ad^4x_bd^4\tilde{q}s_a((E_a^*/M_{\rm inv})P+\tilde{q},x_a)s_b((E_b^*/M_{inv})P-\tilde{q},x_b)$$
$$\times d^4\delta r^* e^{i\tilde{q}\cdot\delta r^*}u_{q^*}^*(x_a^*-x_b^*+\delta r^*/2)u_{q^*}(x_a^*-x_b^*-\delta r^*/2). \quad (2.8)$$

It is very difficult to solve the equation 2.8 because it requires the knowledge of the source function evaluated at off-shell. When the interaction between particles is only due to identical particle interference,

$$u_q(x_a-x_b) = [e^{iq\cdot(x_a-x_b)} \pm e^{iq\cdot(x_b-x_a)}]/\sqrt{2} \quad (2.9)$$

In this case, analytical integration can be performed over $\tilde{q}$ and δr^*,

$$E_aE_b\frac{dN_{ab}}{d^3p_ad^3p_b} = \int d^4x_ad^4x_b\,\{s(p_a,x_a)s(p_b,x_b) \quad (2.10)$$
$$\pm s(P/2,x_a)s(P/2,x_b)\cos[(p_a-p_b)\cdot(x_a-x_b)]\}\,.$$

For non-zero q, $P_0/2 \neq E(\mathbf{P}/2)$, the source functions in the interference term are evaluated off-shell. Due to smoothness approximation, $s(P/2,x_a)s(P/2,x_b)$ is replaced by $s(E(\mathbf{P}/2),\mathbf{P}/2,x_a)s(E(\mathbf{P}/2),\mathbf{P}/2,x_b)$ leading to equation 2.5 or, by $s(p_a,x_a)s(p_b,x_b)$ leading to equation 2.3.

The last assumption is equal time approximation which means all particles are assumed to be created at same time and their interaction takes place just after they are produced. The above assumptions are semi-classical and are described in reference [34] in details.

2.2.1 Relevant Frame of Reference

It is useful to discuss the frame of references which are used in femtoscopic analysis. Each particle used in the correlation can be described by its space-time position , x_i and four momentum, p_i in the reference frame of the emitting source (CMS). When the two particles are combined to form a pair, the three dimensional quantities of relevance on which the correlation functions depend on are the total momentum of the pair P (= p_1 + p_2) and the relative momentum of the pair i.e q (= p_1 - p_2). The femtoscopic analyses are usually carried out in **Longitudinally co-moving system (LCMS)**, a rest frame moving along longitudinal (beam) direction where $p_{1,z} = -p_{2,z}$ and thus, $P_z = 0$. The axes of the

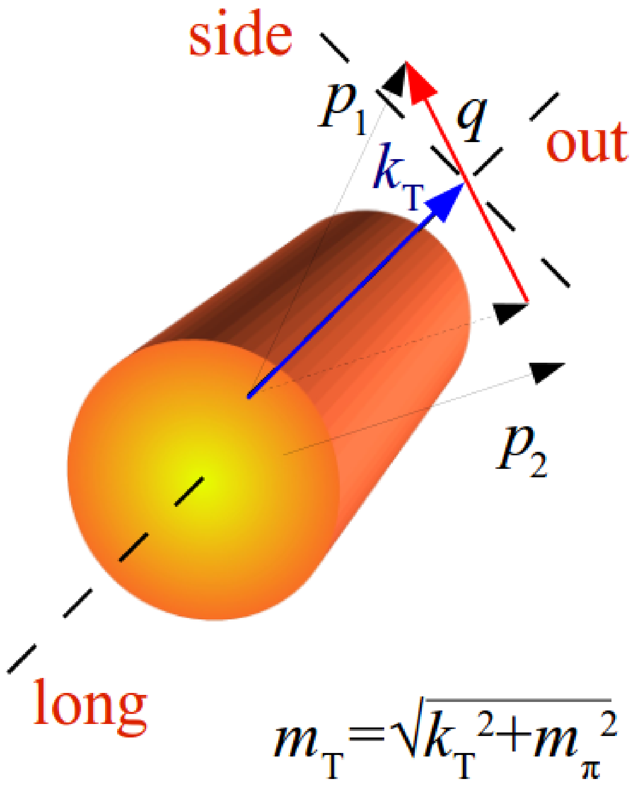

Figure 2.3: *Out* – *Side* – *Long* co-ordinate system

frame are defined in **Out, Side** and **Long** prescription where the longitudinal axis(*Long* axis) is parallel to the beam and the *Out* axis is chosen in the direction of the average momentum of the pair ($k_T = \frac{p_{T_1}+p_{T_2}}{2}$). The *Side* axis is perpendicular to the *Out* and *Long* axes. The **Out-Side-Long** coordinate system (also known as Bertsch-Pratt coordinate system) is shown in Figure 2.3 [35; 36].

Any four-vector W can be expressed in this coordinate system as follows :

$$W_{long} = (P_0 W_z - P_z W_0)/M_T \tag{2.11}$$

$$W_{out} = (P_x W_x + P_y W_y)/P_T \tag{2.12}$$

$$W_{side} = (P_x W_y - P_y W_x)/P_T \tag{2.13}$$

where $M_T^2 = P_0^2 - P_z^2$ and $P_T^2 = P_x^2 + P_y^2$. The analysis presented in the thesis is carried out in the **Pair Rest Frame (PRF)**, where the centre of mass of the pair rests. Therefore, the momenta of the two particles are equal and opposite. The variables are marked with an asterik(*). The relative momentum in this frame can be quantified as $k^* = (p_1 - p_2)/2$.

2.3 Origin of Emission Asymmetry

The evolution of the system created in heavy ion collisions can be modeled by hydrodynamic evolution due to presence of strong radial flow. This suggests a strong space-momentum correlation between the emitted particles.The velocity of particles of the system can have two components: the fluid cell velocity, β_f and the thermal velocity component, β_t. This is represented in Figure 2.4. The evolving system develops a collective radial flow in the transverse direction and one can visualize that the matter is collectively moving from the centre of source. The particles emitted from this fluid element will have same flow velocity, β_f. The mean emission point of a particle whose

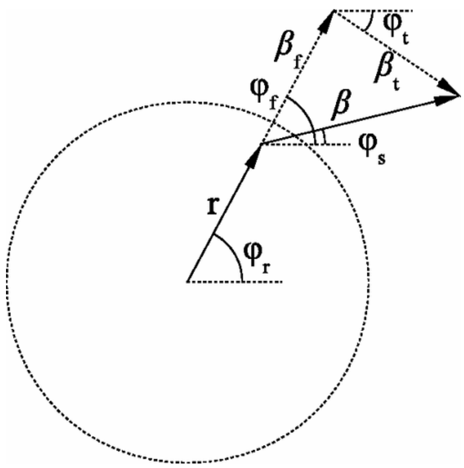

Figure 2.4: Diagram of the particle's velocity (β) decomposition into the flow velocity (β_f) and thermal velocity (β_t) components [37].

component is parallel to the velocity can be written as [37] :

$$x_{out} = \frac{\overrightarrow{x} \cdot \overrightarrow{\beta}}{\beta} = \frac{r(\beta_f + \beta_t cos(\phi_t - \phi_f))}{\beta} \tag{2.14}$$

If one assumes a Gaussian density profile with radius r_0 for particles at fixed β and having a linear transverse velocity profile, $\beta_f = \beta_0 r/r_0$, the mean position can be written as

$$\langle x_{out} \rangle = \frac{\langle r\beta_f \rangle}{\langle \sqrt{\beta_t^2 + \beta_f^2} \rangle} = \frac{r_0\beta_0\beta}{\beta_0^2 + T/m_T} \tag{2.15}$$

The pions and kaons emitted from the fluid element will have the same flow velocity β_f but different momenta. The particles will also receive a momentum dependent random thermal kick. The $\langle r\beta_f \rangle$ is same for both pions and kaons and if we assume that the spatial characteristics of both pion and kaon emission are the same, then $\langle x_{out} \rangle$ for pions will be smaller than $\langle x_{out} \rangle$ for kaons because T/m_t component is smaller for kaons. Thus, on an average, pions (lighter particle) are emitted closer to the center of the system than kaons (heavier particles). One can define an emission asymmetry, $\mu_{out}^{light,heavy}$, between the non-identical particles with different masses as

$$\mu_{out}^{light,heavy} = \langle r_{out}^{light,heavy} \rangle = \langle x_{out}^{light} - x_{out}^{heavy} \rangle \quad (2.16)$$

Therefore, hydrodynamical evolution predicts a negative asymmetry between particles of different masses. Now there are various limits in equation 2.15. When there is no flow in the system then, $\beta_f = 0$ and average emission point for all types of particles is zero. This means all particles are emitted from the center of the source and there is no emission asymmetry between different mass particles. If the temperature is very high, the thermal velocity component of the particles dominate the flow velocity component, and the average emission point for all types of particles is again zero. This shows, emission asymmetry arises in a system where both thermal and flow velocity have similar magnitude.

2.3.1 Formalism : Non-identical particle Femtoscopy

Non-identical particle femtoscopy correlates two particles (say A and B) with different masses. The experimental correlation function is a special form of equation 2.1 and is expressed as:

$$C(\vec{k}^*) = \frac{\int N(\vec{p}_a, \vec{p}_b)\delta(\vec{k}^* - \frac{1}{2}(\vec{p}_a^* - \vec{p}_b^*))d^3p_a d^3p_b}{\int D(\vec{p}_a, \vec{p}_b)\delta(\vec{k}^* - \frac{1}{2}(\vec{p}_a^* - \vec{p}_b^*))d^3p_a d^3p_b} \equiv \frac{N(\vec{k}^*)}{D(\vec{k}^*)} \quad (2.17)$$

where $N(\vec{p}_a, \vec{p}_b)$ is the distribution of correlated pairs of particles type A and B which come from same event and $D(\vec{p}_a, \vec{p}_b)$ is the distribution of pairs when both particles come from two different events(not correlated). Apart from femtoscopic correlation, this correlation function contains all other event-wide correlations like elliptic flow (v_2), global event energy and momentum conservation, resonance decay correlations, residual correlations and jets etc [37; 38]. Therefore, one needs to correct for these non-femtoscopic effects before comparing to models as the later computes the femtoscopic effects only. However, the correction procedures are not very effective and depends on the experiment. In models, the correlation function is defined in terms of single particle and two-particle emission functions which are given by:

$$S_A(\vec{x}_1, \vec{p}_1) = \int S(x_1, p_1, x_2, p_2, ..., x_N, p_N)dx_2dp_2...dx_Ndp_N \quad (2.18)$$

$$S_{AB}(\vec{x}_1, \vec{p}_1, \vec{x}_2, \vec{p}_2) = \int S(x_1, p_1, x_2, p_2, ..., x_N, p_N)dx_3dp_3...dx_Ndp_N \quad , \quad (2.19)$$

where $S_A(\vec{x}_1, \vec{p}_1)$ and $S_{AB}(\vec{x}_1, \vec{p}_1, \vec{x}_2, \vec{p}_2)$ are probabilities to emit a particle and a particle pair from a given space−time point and momentum, respectively. This means the correlation function is a 14-dimensional object, 7 independent components per particle (4 space−time components and 3 momenta components). In order to simplify it, assumptions are made as described below. The source emission function S_{AB} should contain all the physics aspects of the pair emission processes which includes the proper symmetrization for bosons and fermions together with the effects of the interactions (Final State Interactions) between the particles of the pair. For sake of simplicity, most models based on heavy-ion collisions assume that the interaction between two final-state particles is independent from their emission process. Therefore, one can factorize the FSI and the symmetrization of the two-particle wave function to write the correlation function as:

$$C(\vec{p}_1, \vec{p}_2) = \int S_{AB}(\vec{p}_1, \mathbf{x_1}, \vec{p}_2, \mathbf{x_2}) \, |\Psi_{AB}|^2 \, d^4\mathbf{x_1} d^4\mathbf{x_2}, \tag{2.20}$$

where Ψ is the pair wave function. For non-identical particle correlations, the pair wave function Ψ represents a particular physical scenario where the two particles A and B, after being produced in collisions, interact through FSI (Coulomb and/or Strong) till freeze-out. After the freeze-out, they stream towards the detector as plane-waves. Ψ can be expressed as the solution of scattering problem with the reversed time direction. The wave function is factorized into two parts. The first part describes the motion of the pair as a whole and the wave function is the function of pair total momentum and "average"emission point. The second part describes the interaction between the pair particles which depends on relative pair momentum $\vec{k}^*$ and relative separation $\vec{r}^*$. The first part of the wave function does not affect the modulus as it is an exponential function and contributes an additional phase only. This part can be neglected and the pair wave function can be written as :

$$\Psi^{(+)}_{-k^*}(\mathbf{r}^*) = \sqrt{A_C(\eta)} \left[e^{-i\vec{k}^*\mathbf{r}^*} F(-i\eta, 1, i\zeta) + f_C(\vec{k}^*) \frac{\tilde{G}(\rho, \eta)}{\mathbf{r}^*} \right] \tag{2.21}$$

where A_C is the Gamow factor, F is the confluent hypergeometric function, $\eta = 1/(k^* a_C)$, $\zeta = k^* r^* (1 + \cos\theta^*)$, $\tilde{G}$ is the combination of the regular and singular s-wave Coulomb functions and f_C is the strong scattering amplitude, modified by the Coulomb interaction. θ^* is the angle between the pair relative momentum k^* and relative position r^* in PRF and a_C is the Bohr radius of the pair and has values 248.52 fm, 83.59 fm and 222.56 fm for pion-kaon, kaon-proton and pion-proton pairs respectively, and has negative values for opposite-charged pairs. For identical bosons and fermions, Ψ must also be properly symmetrized and anti-symmetrized, respectively. The expression for f_C is given by:

$$f_C(\vec{k}^*) = \left[\frac{1}{f_0} + \frac{1}{2} d_0 \vec{k^*}^2 - \frac{2}{a_C} h(\vec{k}^* a_C) - i\vec{k}^* A_C(\vec{k}^*) \right]^{-1}, \tag{2.22}$$

where the $f_0 = 0.137$ fm for like-sign pair of pion-kaon, -0.071 fm for unlike-sign pair of pion-kaon, -0.148 fm for like-sign pair of pion-proton, 0.112 fm for unlike-sign pair of pion-proton, -0.360 fm for like-sign pair of kaon-proton pair, d_0 is the effective radius and taken to 0 for above mentioned pairs at small k^* where the $1/f_0$ term dominates. The expression for F is given by:

$$F(\alpha, 1, z) = 1 + \alpha z + \alpha(\alpha + 1)z^2/2!^2 + ... \tag{2.23}$$

Emission function The FSI interaction shown in equation 2.21 depends only on $\vec{k}^*$ and $\vec{r}^*$ of the pair. The term S_{AB} from equation 2.19 can be simplified in terms of $\vec{k}^*$ and $\vec{r}^*$ as:

$$\begin{aligned} S_{AB}(\vec{k}^*, \mathbf{r}^*) &= \int\int_{P_{min}}^{P_{max}} S_{AB}(\mathbf{x_1}, \vec{p}_1, \mathbf{x_2}, \vec{p}_2) \times \delta(\vec{k}^* - 1/2(\vec{p}_1^* - \vec{p}_2^*))d^3p_1 d^3p_2 \\ &\times \delta(\vec{r}^* - (\vec{x}_1^* - \vec{x}_2^*))d^4x_1 d^4x_2 \end{aligned} \tag{2.24}$$

where the integration over space is to be done over full variable range and the measurable particle momenta has boundary P_{min} and P_{max}.

The equation 2.20 can be rewritten as:

$$C(\vec{k}^*) = \int S_{AB}(\vec{k}^*, \mathbf{r}^*) \left|\Psi_{-k^*}^{(+),AB}(\mathbf{r}^*)\right|^2 d^4\mathbf{r}^*. \tag{2.25}$$

In the case where emission process of each particle is assumed to be independent, the two-particle emission function S_{AB} can be written in terms of single particle emission function via a convolution:

$$\begin{aligned} S_{AB}(\vec{k}^*, \mathbf{r}^*) &= \int S_A(\vec{p}_1, \mathbf{x_1}) S_B(\vec{p}_2, \mathbf{x_2}) \times \delta(\vec{k}^* - \frac{1}{2}(\vec{p}_1 + \vec{p}_2))\delta(r^* - \mathbf{x_1} + \mathbf{x_2}) \\ &\times d^4\mathbf{x_1} d^4\mathbf{x_2} d^3\vec{p}_1 d^3\vec{p}_2. \end{aligned} \tag{2.26}$$

In the second case where a model of discretely producing particles exists, equation 2.25 is evaluated via the Monte-Carlo procedure using the expression:

$$C(\vec{k}^*) = \frac{\sum_{pairs} \delta(\vec{k}^*_{pair} - \vec{k}^*) \left|\Psi_{-k^*}^{(+),AB}(\mathbf{r}^*)\right|^2}{\sum_{pairs} \delta(\vec{k}^*_{pair} - \vec{k}^*)}. \tag{2.27}$$

Correlation function and asymmetry signal As shown in equation 2.20, the correlation function is a pair wave function averaged over the source. The simplified version of this which contains Coulomb correlation only and is averaged over pairs, can be written as:

$$C(k^*) = A_C(\eta)[1 + 2\langle r^*(1 + \cos\theta^*)\rangle / a_c + ...], \tag{2.28}$$

In this part, like-sign pion-kaon pairs have been considered to illustrate the origins of the asymmetry where A_C is negative and a_c is positive. $r^*(1 + \cos\theta^*)$ is always positive as per definition. The overall correlation effect ($R = |C - 1|$) will be $1 - A_C$ for $r^* = 0$ (a point source). The correlation effect R decreases as the size of the system and r^* increase. For the pion-kaon pairs, $2\langle r^*(1 + \cos\theta^*)\rangle / a_c > 0$ and $A_C - 1 < 0$, so they compete each other. This shows that the correlation function is sensitive to the source size. It is important to consider that the correlation function becomes less sensitive to the system size as the size increases which implies that the method is useful to measure the source size precisely when the system is not very large.

As discussed above, a non-zero mean value of the separation vector $\langle \mathbf{r}^* \rangle$ can be yielded by the two-particle emission function. To observe this in experimental data, equation 2.28 shows that the correlation function depends on the angle (θ^*) between $\vec{k}^*$ and $\vec{r}^*$. When $\cos\theta^* > 0$ i.e. both the particles are aligned, the correlation effect is smaller than when both the particles are not aligned($\cos\theta^* < 0$). When $\cos\theta^* > 0$, it indicates a scenario where the particles are moving away from each other after being produced whereas they approach each other when $\cos\theta^* < 0$. Even if θ^* can not be accessed in experiments but it affects the R. The relative momentum $\vec{k}^*$ and pair total momentum $\vec{K}$ for the velocity $\vec{v}$ can be calculated using experimental data of measured momenta. In the transverse plane, the correlation function can be divided into two groups: **C+$_{\mathbf{out}}$** corresponds to the case where lighter mass particles are faster i.e. $\overrightarrow{k^*}.\overrightarrow{v} > 0$ and **C−$_{\mathbf{out}}$** when the heavier particles are faster i.e. $\overrightarrow{k^*}.\overrightarrow{v} < 0$, Figure 2.5. For $k^* \to 0$, higher terms of$1/a_C$ or $1/k^*$ can be neglected and we have:

$$F = 1 + 2\frac{r^*}{a_C} + 2\frac{\vec{k}^*\vec{r}^*}{k^* a_C} + O\left[\left(\frac{1}{a_C}\right)^2\right] + O\left[\left(\frac{1}{k^*}\right)^2\right] + ... \tag{2.29}$$

which implies:

$$C|_{k^*} = \langle A_C F^* F \rangle \doteq A_C \left(1 + 2\frac{\langle r^* \rangle}{a_C} + 2\frac{\left\langle \vec{k}^*\vec{r}^* \right\rangle}{k^* a_C}\right). \tag{2.30}$$

One should also consider that

$$\left\langle \vec{k}^*\vec{r}^* \right\rangle = \langle k^*_{out} r^*_{out} + k^*_L r^*_L \cos(\theta^* - \psi) \rangle = k^* \cos\psi \langle r^*_{out} \rangle . \tag{2.31}$$

where

$$\psi = \theta^* + \phi. \tag{2.32}$$

and ϕ is the angle between the pair velocity $\vec{v}$ and $\vec{r}^*$. Considering for a fixed k^* and $\cos(\psi)$:

$$C(k^*, \cos\psi) = A_C \left(1 + 2\frac{\langle r^* \rangle}{a_C} + 2\cos\psi \frac{\langle r^*_{out} \rangle}{a_C}\right), \tag{2.33}$$

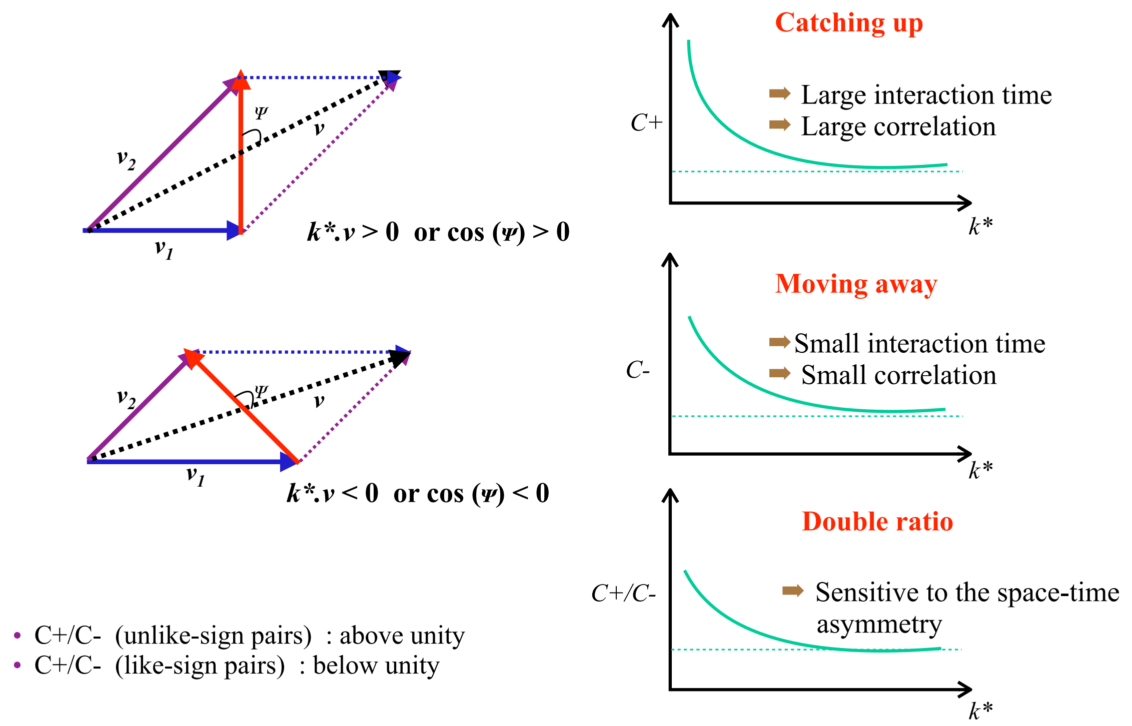

Figure 2.5: (**Left**) The blue arrow shows the heavier particle which is emitted first and the purple arrow represents the lighter mass particle. (**Right**) The schematic variation of C+, C- and C+/C- with respect to k^*.

The uniformity of $\cos\psi$ distribution for uncorrelated particles at $k^* \rightarrow 0$, we have:

$$\begin{aligned} C_+ &\doteq A_C \int_0^1 C(\cos\psi) d\cos\psi = 1 + 2\frac{\langle r^* \rangle}{a_C} + \frac{\langle r^*_{out} \rangle}{a_C} \\ C_- &\doteq A_C \int_{-1}^0 C(\cos\psi) d\cos\psi = 1 + 2\frac{\langle r^* \rangle}{a_C} - \frac{\langle r^*_{out} \rangle}{a_C} \\ \frac{C_+}{C_-}\Big|_{k\rightarrow 0} &\doteq 1 + 2\frac{\langle r^*_{out} \rangle}{a_C}. \end{aligned} \tag{2.34}$$

Figure 2.6 and 2.7 show the pion-kaon femtoscpoy results from Au−Au collisions at $\sqrt{s_{NN}}$= 130 GeV. It can be seen that the double ratio for unlike-sign charged pairs is above unity and the same is below unity for like-sign charged pairs. This indicates that kaons leave the system earlier than pions.

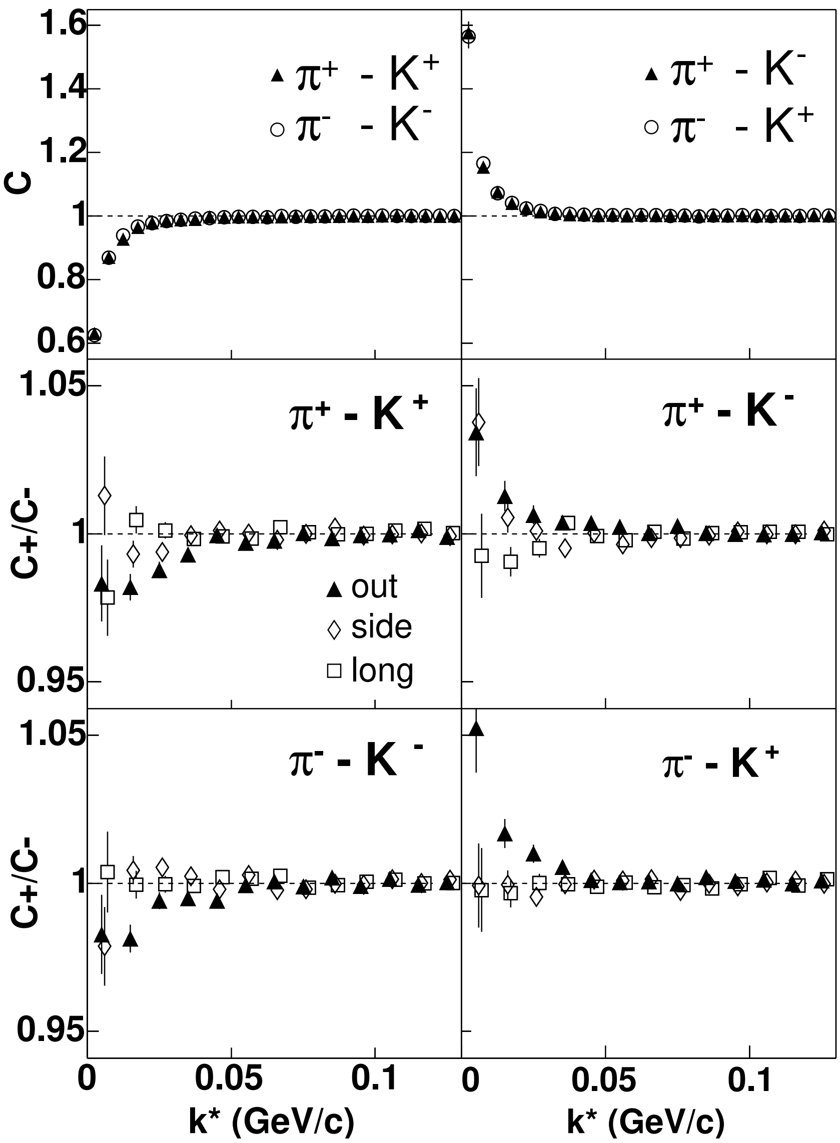

Figure 2.6: (**Upper panels**) pion-kaon correlation functions $C(k^*)$ (the average of $C_+(k^*)$ and $C_-(k^*)$) as a function of k^* in Au−Au collisions at $\sqrt{s_{NN}}$= 130 GeV. (**Middle and lower panels**) The projection of double ratio (C+/C-) in k^*_{out}, k^*_{side} and k^*_{long} as a function of k^* [39].

Spherical harmonics representation of Correlation Function The correlation function can also be studied very effectively by decomposing it in terms of Spherical Harmonics (SH). In SH representation, the 3-dimensional correlation function is represented as an infinite set of 1-dimensional components defined as:

$$C_l^m(\vec{k^*}) = \frac{1}{\sqrt{4\pi}} \int d\varphi d(cos\theta) C(k^*, \theta, \varphi) Y_l^m(\theta, \varphi), \quad (2.35)$$

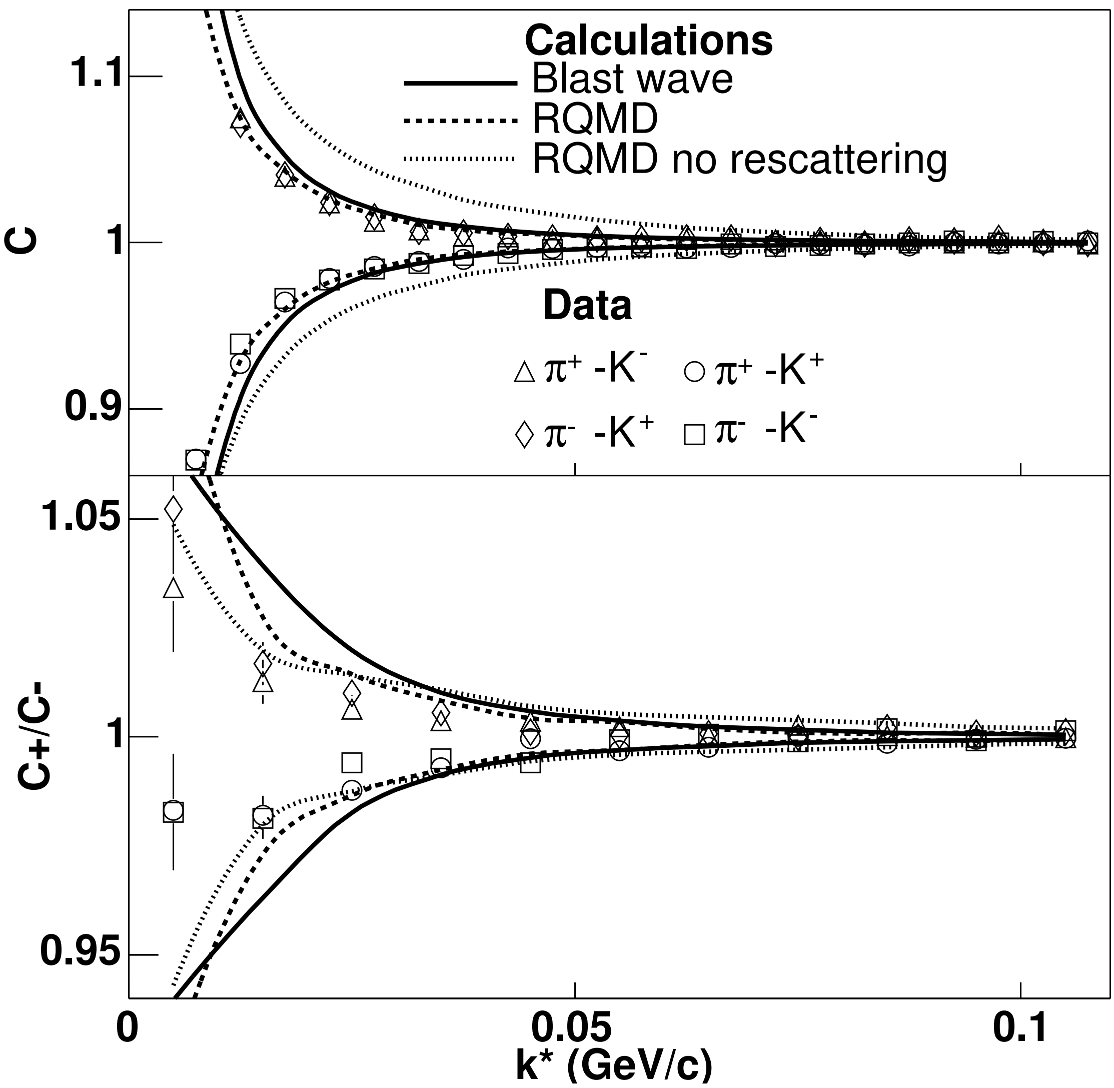

Figure 2.7: Comparison of the pion-kaon correlation functions (Upper panel) and double ratios (lower panel) in Au−Au collisions at $\sqrt{s_{\rm NN}}$= 130 GeV with different models [39]

where $C_{\rm l}^{\rm m}$ are the components the correlation function and $Y_{\rm l}^{\rm m}$ are the spherical harmonics given by the following equation:

$$Y_{\rm l}^{\rm m}(\theta, \varphi) = (-1)^{\rm m} \left[\frac{(2l+1)(l-m)!}{4\pi(l+m)!} \right]^{1/2} P_{\rm l}^{\rm m}(cos\theta) e^{{\rm i m}\varphi}, \tag{2.36}$$

where $P_{\rm l}^{\rm m}(cos\theta)$ are associated Legendre polynomials. The polar angle θ and the azimuthal angle φ are related to the Bertsch-Pratt coordinate system as:

$$k^*_{\rm out} = |\vec{k}^*| sin\theta sin\varphi, \tag{2.37}$$

$$k^*_{\rm side} = |\vec{k}^*| sin\theta cos\varphi, \tag{2.38}$$

$$k^*_{\rm long} = |\vec{k}^*| cos\theta. \tag{2.39}$$

In this approach, C_0^0 reflects the overall system size, $\Re C_1^1$ is sensitive to the emission asymmetry and vanishes if there is no emission asymmetry between pair of particles. The components $\Re C_2^0$ and $\Re C_2^2$ give the size of the system in *Out*, *Side*, and *Long* directions.

Chapter 3

The ALICE Experiment at LHC

"Without data you are just another person with an opinion." – W. Edwards Deming

Abstract: This chapter describes the Large Hadron collider with specific focus on ALICE experiment and its detector components.

The standard model has been proven quite successful in many experiments. This theory treats twelve particles (and their antiparticles) as fundamental particles. These particles interact with each other by four fundamental interactions. However, there are many unanswered questions and our understanding of the universe is not complete without understanding about the origin of mass of particles, composition of the invisible part of the universe *dark matter* and *dark energy*, matter and anti-matter asymmetry observed in the visible universe. The study of QGP can help us to understand the evolution of universe as well as to understand matter at extreme density and temperature. In order to understand and explore more about the aforementioned puzzles of the universe and its evolution via experiments, the Large Hadron Collider (LHC) has been designed.

3.1 Large Hadron Collider (LHC)

The LHC is the biggest accelerator complex installed at CERN (Figure 3.1). LHC is reusing the same tunnel[1] used for Large Electron-Positron collider (LEP) which is 27-km in circumference [40]. The maximum attainable energy in a collider is the function of accelerator size, radius of machine and the magnetic field strength which keeps particles

[1]The tunnel was built underground because building a tunnel underground is cheaper than acquiring land to build a 27 km circumference machine. Also, Earth's crust protects it from radiation. The tunnel's depth is 100 m in terms of mean and varies between 50 m (towards Lake Geneva) and 175 m (under the Jura). This is due to geological considerations which translates into cost.

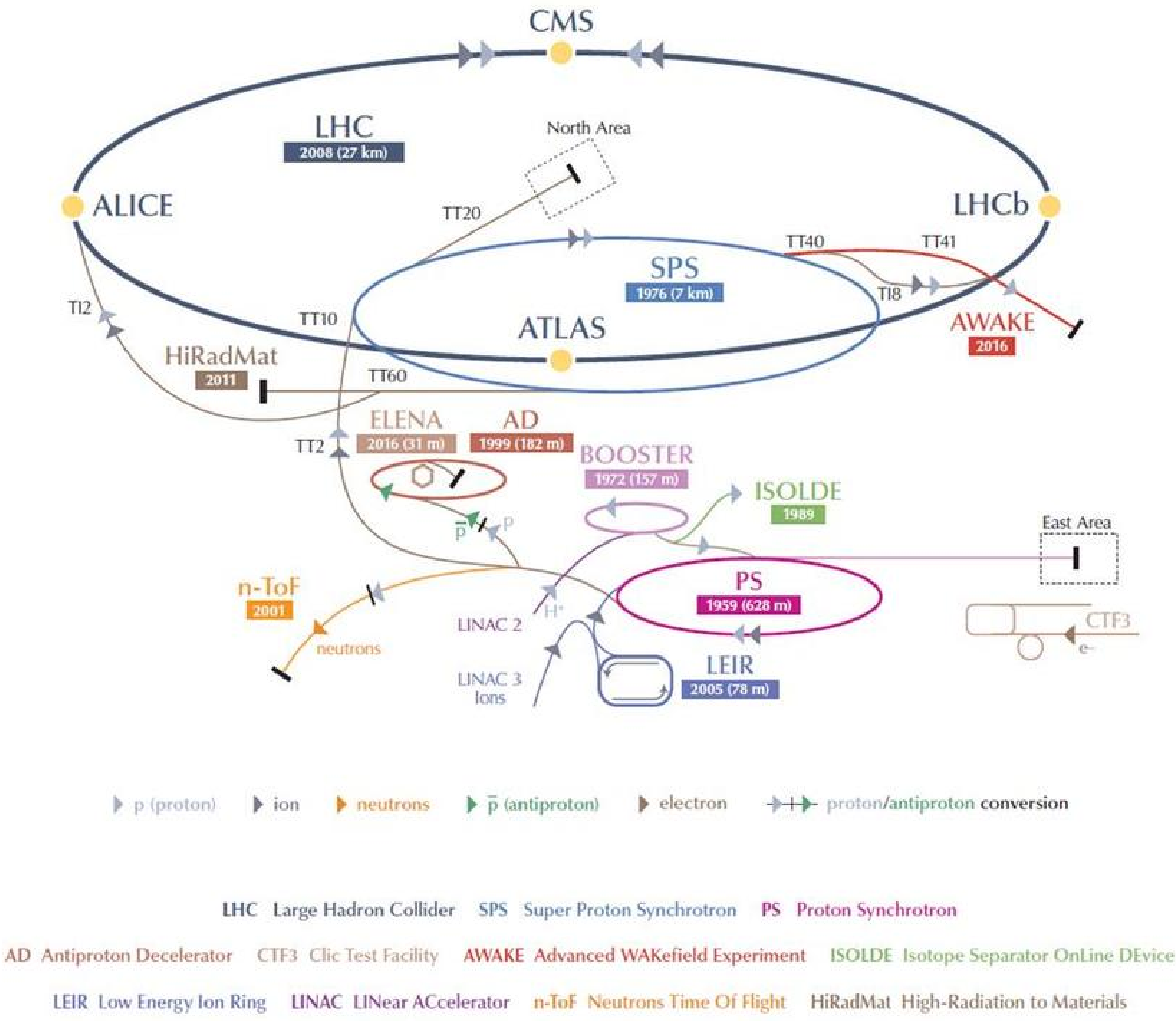

Figure 3.1: CERN accelerator complex [40]

in their orbit. The circular colliders have extra advantage that when two oppositely circulating beams collide, the collision energy is them of energies of two beams (E = E_{beam1} + E_{beam2}) while in fixed target accelerators E $\propto \sqrt{E_{beam}}$.

The LHC accelerates either protons or ions, which are hadrons. An accelerator can only accelerate particles which are charged[2] and stable (except in special cases). In the LHC like colliders, heavy particles like proton and ions have much lower energy loss due to synchrotron radiation compared to lighter particles such as electrons. Therefore, in order to achieve maximum beam energy, accelerating heavy particles is more effective.

The number of events per second in the LHC collisions is given by:

$$N_{event} = L\sigma_{event} \tag{3.1}$$

[2]electromagnetic devices can only influence and accelerate charge particles

where σ_{event} is the cross section for the event under study and L is the machine luminosity. L depends on the beam parameters and can be written as the following for a Gaussian beam profile:

$$L = \frac{N_b^2 n_b f_{rev} \gamma_r}{4\pi \varepsilon_n \beta^*} F \tag{3.2}$$

where N_b is the number of particles per bunch, n_b is the number of bunches per beam, f_{rev} is the revolution frequency, γ_r is the relativistic gamma factor, ε_n is the normalized transverse beam emittance, β^* is the beta function at the collision point and F is the geometric luminosity reduction factor due to the crossing angle at the interaction point (IP). The expression of F is given by:

$$F = \left(1 + \left(\frac{\theta_c \sigma_z}{2\sigma^*}\right)^2\right)^{-1/2} \tag{3.3}$$

where, θ_c is the full crossing angle at the IP. σ_z is the RMS bunch length and σ^* is the transverse RMS beam size at the IP.

An ultrahigh vacuum with the beam vacuum pressure $\sim 10^{-13}$ atm is maintained inside the LHC beam pipe to avoid collisions with gas molecules. A large variety of magnets ($\sim$ 9600 in total), like dipole magnet[3], quadrupole magnet, sextupole magnets etc are used at LHC to optimize (to bend and focus) the beam trajectory. A list of the important parameters for the LHC is provided in Table 3.1.

3.1.1 Acceleration of Proton

In order to accelerate and collide protons at the LHC, electrons are stripped off from hydrogen atoms to get protons in the first stage. These protons are then injected into Proton Synchrotron Booster (PSB) at an energy of 50 MeV from Linac2 where the booster accelerates them to 1.4 GeV. This is followed by the protons passing through the Proton Synchrotron (PS) where the beam is accelerated to 25 GeV. They are further accelerated to 450 GeV in the Super Proton Synchrotron (SPS). Finally, they are transferred from SPS to the LHC beam pipe in both clockwise and anti-clockwise direction where they are accelerated to the required nominal collision energy.

[3]The LHC dipoles use niobium-titanium (NbTi) cables. The LHC operates at 1.9 K (-271.3^{o}C). A current of 11,850 A flows in the dipoles, to create the high magnetic field of 8.33 T which required to bend the 7 TeV beams around the 27-km ring of the LHC. The temperature of 1.9 K is reached by pumping superfluid helium into the magnet systems. Each dipole is 15 m long and weighs around 35 t.

Quantity	number
Circumference	26,659 m
Dipole operating temperature	1.9 K (-271.3^{o}C)
Number of magnets	9593
Number of main dipoles	1232
Number of main quadrupoles	392
Number of RF cavities	8 per direction
Energy, protons	6.5 TeV (Design value: 7 TeV)
Energy, ions	2.56 TeV/u (Energy per nucleon)
Peak magnetic dipole field	7.74 T
Distance between bunches	~ 7.5 m
Peak Luminosity (protons)	~ 1.2×10^{34} cm^{-2}s^{-1}
No. of bunches per proton beam	2808
No. of protons per bunch (at start)	1.2×10^{11}
Peak Luminosity (ions)	~ 1×10^{27} cm^{-2}s^{-1}
No. of bunches per ion beam	592
No. of ions per bunch (at start)	7.0×10^{7}
Number of turns per second	11 245
Number of collisions per second	1 billion

Table 3.1: LHC parameters [41]

3.1.2 Acceleration of Pb Ions

The LHC can accelerate heavy ions like 'Pb'(Lead). The Pb ions are produced from a highly purified lead sample which is heated to a temperature of ~$550^{o}C$. The lead vapor is ionized by an electron current and in this process many different charged states of Pb are produced with a maximum of Pb^{+27}. These ions are selected and accelerated to 4.2 MeV/nucleon before passing through a carbon foil, which strips most of the electrons to create Pb^{+54}. The Pb^{+54} beam is then accelerated to 72 MeV/nucleon in the Low Energy Ion Ring (LEIR), which transfers them to the PS. The PS accelerates the beam to 5.9 GeV/nucleon and sends it to the SPS after passing it through a second foil where it is fully stripped to Pb^{+82}. The SPS accelerates it to 177 GeV/nucleon then sends it to the LHC, which accelerates it further to 2.76 TeV/nucleon. These two beams circulating in opposite direction in the LHC ring collide at four interaction points. These interaction points are equipped with four main different detector facilities− A Toroidal LHC ApparatuS (AT-

LAS), Compact Muon Solenoid (CMS), A Large Ion Collider Experiment (ALICE) and Large Hadron Collider beauty (LHCb) to record the collision data. The ATLAS and CMS experiment are high luminosity experiments and, are situated at CERN Point 1 and CERN Point 5 (diametrically opposite in the LHC ring), respectively. They are general purpose detector to study the Higgs Boson and its properties, to search for new physics beyond standard model like supersymmetry (SUSY) and extra-dimensions of the universe. These detectors are designed to primarily record p−p collisions but they are also capable of recording Pb−Pb collisions. The LHCb is dedicated to study the matter-antimatter puzzle of the universe. It has been installed at CERN Point 8 and, records only p−p collisions data. The ALICE experiment is also a general purpose detector designed specifically to study the formation and evolution of QGP. The details of the ALICE experiment is described briefly in the following section.

3.2 ALICE experiment

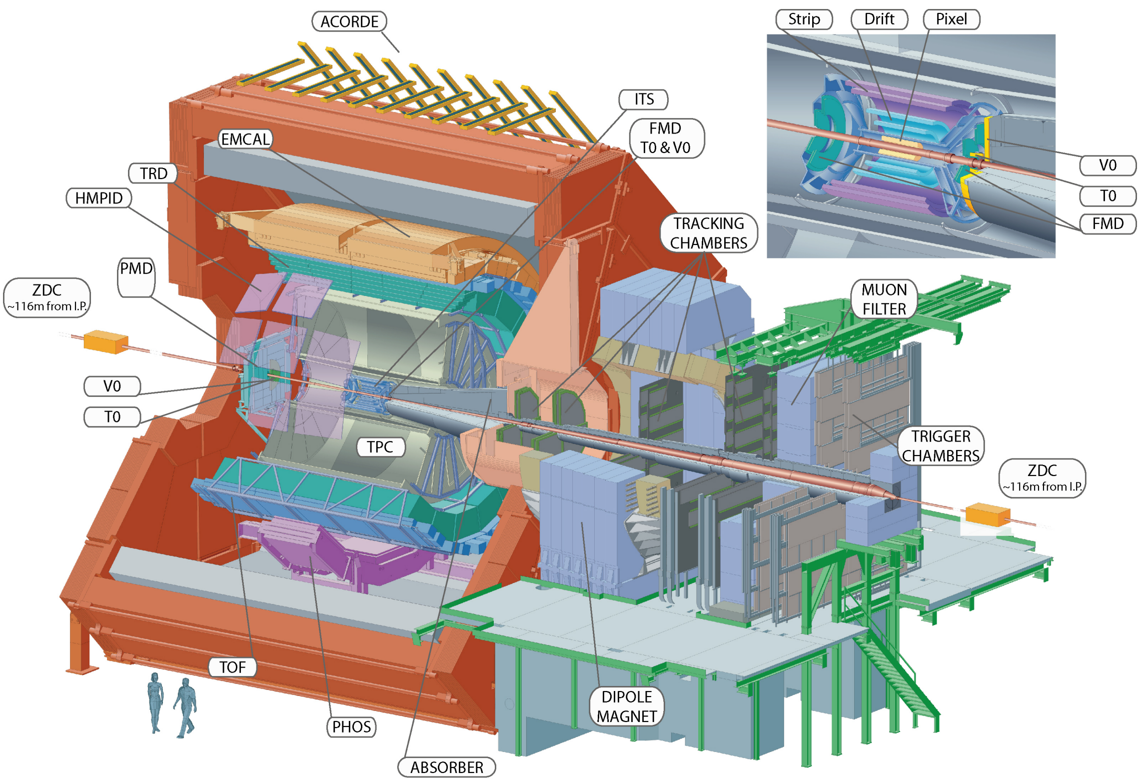

Figure 3.2: A Large Ion Collider Experiment at CERN [42]

A Large Ion Collider Experiment (ALICE), is one of the largest experiment at the LHC at CERN. It is a detector dedicated to the study of the hot and dense matter created in high energy heavy-ion collisions [42]. It is built by a collaboration of more than 1000 members from about 30 countries. The experiment measures $16 \times 16 \times 26$ m^3 and has a weight of about 10000 tonnes.

The main goal of the ALICE experiment is to study the properties of strongly interacting matter at extremely high temperatures and energy densities, where a novel phase of quark-gluon plasma (QGP) is expected to be formed in heavy ion collisions. In addition, the analysis of p−p collisions at LHC energies provides valuable references for the Pb−Pb observables and provides further insights in special topics where the ALICE measurements can act as complementary measurement to the other LHC experiments. These include minimum-bias measurements, observables requiring excellent particle identification, and the physics observables at low-p_T and diffractive events. The main sub detectors of ALICE (Figure 3.2) are introduced in the following sections. The detectors are broadly divided into central and forward detectors.

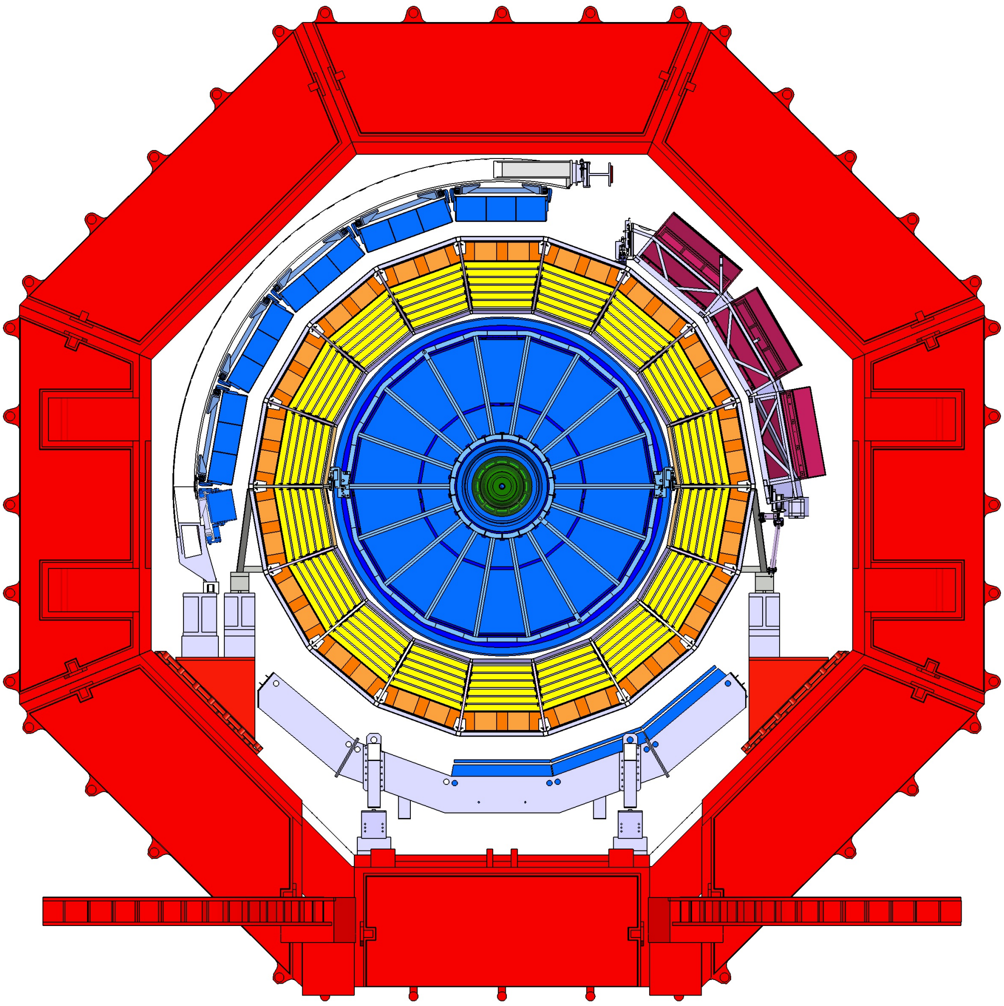

Figure 3.3: General ALICE Cross-Section with L3 Magnet [42]

3.3 Central detectors

ALICE consists of a central barrel with an η coverage of $|\eta| < 0.9$. The barrel is enclosed in a solenoid (reused from the L3 experiment) with a magnetic field of 0.5 T. The central part is optimized for the detection of charged hadrons, electrons and photons.

3.3.1 The Inner Tracking System

The Inner Tracking System (ITS) is the closest detector to the interaction point[42; 43]. The main tasks of ITS are:

- localize the position of primary vertex with a resolution better than 100 μm
- reconstruct the secondary vertices originating from the decays of hyperons and mesons
- tracking and identifying particles with momentum lower than 200 MeV/c[4]
- improve the momentum resolution for particles reconstructed by the Time-Projection Chamber (TPC) and to reconstruct particles traversing dead regions of the TPC.

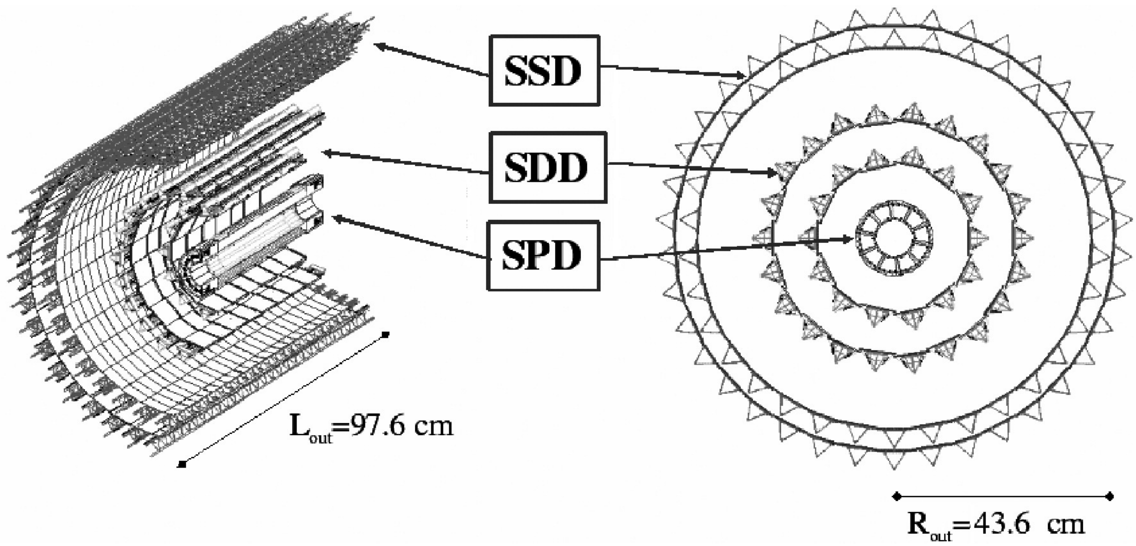

Figure 3.4: Layout of the ALICE ITS [44]

The ITS is 98 cm long and spans from a radius of 4 cm to 43 cm. It is a six layer cylindrical silicon detector surrounding the LHC beam pipe and its six layers are located

[4]Standalone tracking can detect very low-p_T particles down to 35 MeV/c that do not reach the other detectors.

at radii 4 cm, 7 cm , 15 cm, 24 cm, 39 cm and 44 cm from the interaction point. The η coverage of ITS is from -0.9 to 0.9. A schematic layout of ITS is shown in Figure 3.4. The two innermost layers are called Silicon Pixel Detectors (SPD). These are made of hybrid silicon pixels consisting of two-dimensional matrix of silicon diodes operating in reverse-biased mode. Its readout chips have high radiation tolerance design which is essential in the determination of position of the primary vertex and in the measurement of impact parameter of secondary tracks. This is required because of expectation of very high particle density produced in heavy-ion collisions at LHC ($\sim$ 50 particles per cm^2).

The two middle layers of the ITS are equipped with Silicon Drift Detectors (SDD) where particle density is expected to be $\sim$ 7 particles per cm^2. It is made of 300 μm homogeneous high-resistivity Neutron Transmutation Doped (NTD) silicon. The working principle of SDD is similar to a gaseous drift chamber. When a charged particle passes through it, the electron-hole pairs are produced. The drift time of electrons collected by the readouts determines the spatial position. The spatial precision of SDD is 35 μm. The two outermost layers of the ITS consists of Silicon Strip Detector (SSD) where the particle density is expected to be $\sim$ 1 particle per cm^2. The SSDs are crucial for connection of track from the ITS to the TPC. The four outer layers have analog readouts and hence, are also useful in particle identification using the specific energy loss (dE/dx) measurement in low momentum regime.

3.3.2 The Time-Projection Chamber

The Time-Projection Chamber (TPC) is the main tracking detector in ALICE central barrel [42; 45]. It is designed to provide precise measurement of charged particle momentum, particle identification and vertex determination. The TPC has full azimuthal coverage with $|\eta| < 0.9$. It surrounds the ITS with an inner radius of 80 cm, and an outer radius of 250 cm. Its length is 5 m and the active volume of 90 m^3, which makes it the largest TPC ever built.

It is made of a large cylindrical field cage which is filled with 90 m^3 of $Ne/CO_2/N_2$ (90/10/5) gas where the figures inside the bracket indicates the proportion. The TPC has 18 trapezoidal sectors with multi-wire proportional chambers (MWPC) at both ends (Figure 3.5). The readout of the signal is performed by the 570132 pads of 3 different sizes which form the cathode of multi-wire proportional chambers located at the end. The field cage design is based on a central high voltage electrode and two opposite axial potential divider to create a highly uniform electrostatic field in common gas volume. The central electrode voltage is 100 kV and the field cage operates at high voltage gradient ($\sim$ 400 V/cm) resulting in maximum drift time of about 90 μs. The entire detector is kept at an

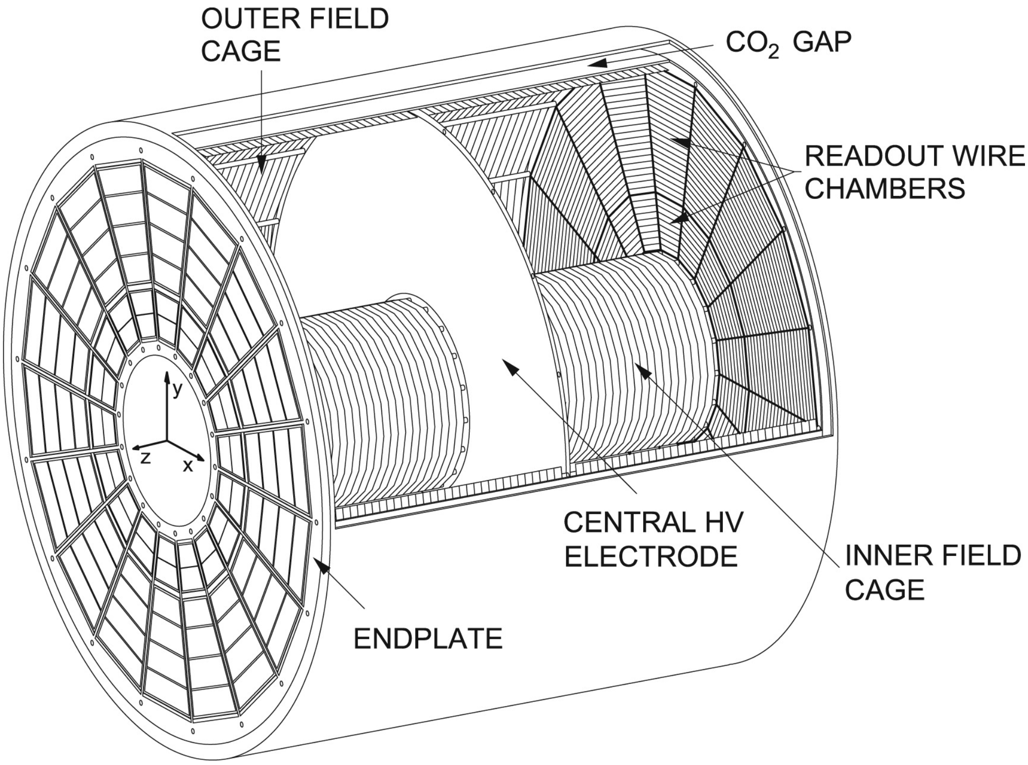

Figure 3.5: Schematic 3D view of ALICE TPC [46]

uniform magnetic field of 0.5 T along the z-direction by the L3 magnet. The large radius of the TPC as well as its fine granularity ensures a good tracking. Tracks with p_T ranging from 150 MeV/c up to 100 GeV/c can be measured. The precise measurement of the specific energy-loss through ionization (dE/dx) (energy resolution of 5%) together with the momentum measurement is used for identifying tracks. In the global tracking procedure, the TPC information is combined with the information from the ITS and other detectors to reconstruct global tracks. Using only TPC information for reconstruction ("TPC-only tracks") can ensure a uniform acceptance in azimuth but the momentum resolution might not be as good as that of global tracks. Since the finite drift time of the charged ions of 90 μs leads to a relatively slow read-out compared to other detectors, the TPC limits the rate of events that can be read out and recorded.

3.3.3 Transition-Radiation Detector

Transition Radiation detector (TRD) is installed between the TPC and Time Of Flight(TOF) detector [42; 47]. It spans its radial position from 2.9 m to 3.68 m from interaction point. Its η coverage is $|\eta| < 0.84$ with full azimuthal acceptance. It consists of 18 super modules. Each super module consists 30 modules arranged in five stacks along z-direction and 6 layers in radius. Every single layer consists of a radiator, a drift chamber (contains Xe/CO2 in proportion of 85 : 15 as counting gas) and MWPC with readout electronics. A schematic of TRD is shown in Figure 3.6. The main goal of the transi-

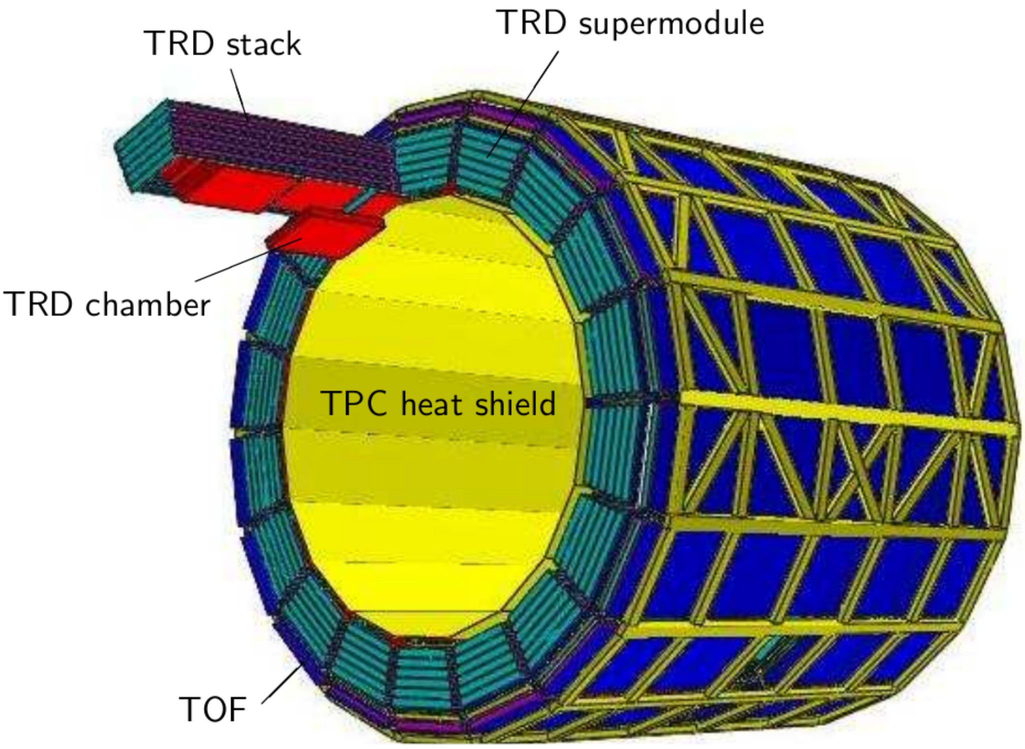

Figure 3.6: Schematic of the TRD layout in the ALICE space frame [42]

tion radiation detector (TRD) is to identify electrons above momenta 1 GeV/c because at high momenta, it becomes difficult to distinguish electron and pions with a dE/dx measurement. When a charged particle traverses between the boundary of two materials with different dielectric constants, transition radiation is emitted. The amount of transition radiation emitted is proportional to $\gamma = v/c$. The different amount of transition radiation of these particle species can be used to distinguish between electrons and pions. The TRD acts as a fast trigger to high momentum charged particles. It is a part of Level 1 trigger and can enhance the recorded yield of Υ, high-p_T J/Ψ etc. It can also be used as a tracker to increase the momentum resolution in the central barrel using the tracklet information from its layers.

3.3.4 Time-Of-Flight Detector

The Time Of Flight (TOF) detector is another very important detector in the ALICE central barrel [42; 48]. It is installed in a cylindrical shell with inner and outer radii of 370 cm and 399 cm from the interaction point, respectively. It covers a pseudo-rapidity region of $\eta \lesssim 0.9$. The TOF detector has a modular structure which consists of 18 sectors in φ and

5 segments in z direction. Each sector has one supermodule which has 5 modules. A 10-gap double-stack MRPC[5] strip is the basic unit of TOF detector. This strip is 122 cm long and 13 cm wide with an active area of 120×7.4 cm^2. The strips are placed (positioned transversely to the z direction) inside five gas-tight modules which also act as Faraday cages. The system of MRPCs achieves an overall time resolution of 100 ps. A schematic of the detector is shown in Figure 3.7.

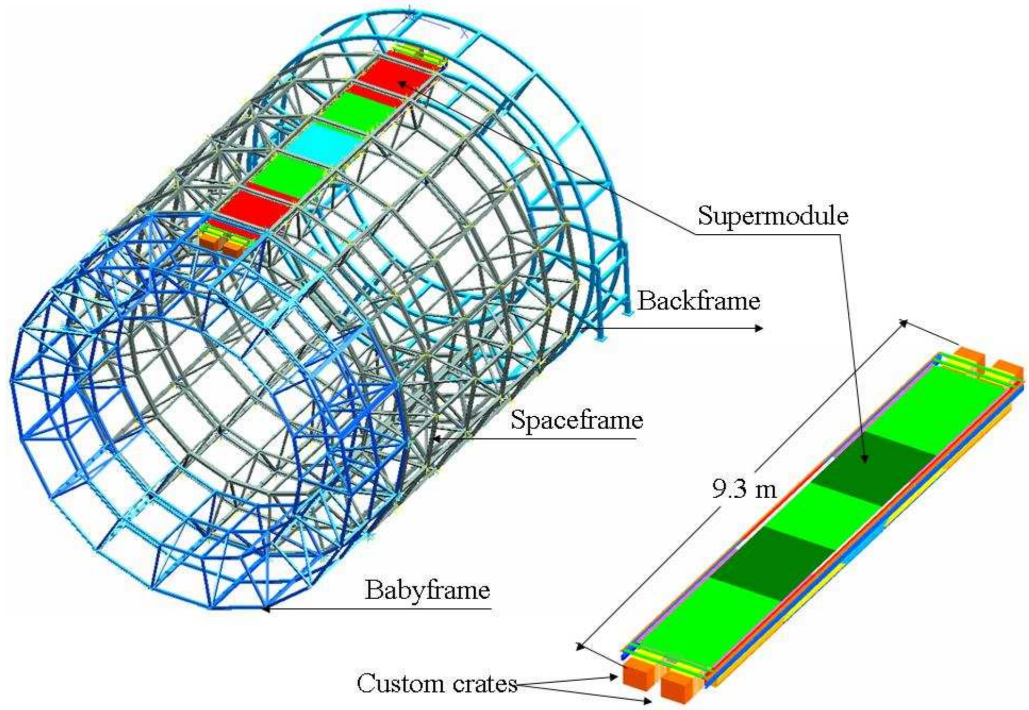

Figure 3.7: The schematic diagram of a single TOF supermodule consisting of 5 modules [42]

The TOF can perform particle identification (PID) in the intermediate momentum range, by the measurement of the time of flight of particles. It can distinguish pions, kaons and protons by measuring their time of flight at intermediate p_T of 0.5-3.0 GeV/c. The TOF can also be coupled with ITS and TPC for track and vertex reconstruction and for measurements of dE/dx in the low momentum region up to 1 GeV/c, to provide event-by-event identification of pions, kaons, and protons.

3.3.5 Specialized Detectors

A set of special purpose detectors, each covering a smaller range in azimuth than the main detectors, are installed in the central barrel as described below:

[5] multi-gap resistive plate chamber

High-Momentum Particle Identification Detector The High-Momentum Particle Identification Detector (HMPID) provides enhanced PID information of charged hadrons at high momentum range (p_T > 1 GeV/c) which is not attainable in ITS and TPC (through energy loss measurements) and in TOF (through time of flight measurements) [42; 49]. HMPID has very low acceptance ~ 5% in central barrel region. It has five modules that extend from 1.2^o to 58.8^o in azimuth and have η coverage from -0.6 to 0.6. The design of HMPID is based on proximity focusing Ring Imaging Cherenkov (RICH) counter. Liquid perfluorohexane (C_6F_6) is used as the radiator. This radiator emits Cherenkov photons when a charged particle passes through it. The emitted photons are detected by a thin layer of CsI deposited onto the cathode pads of MWPC. CH_4 is used as detector gas between radiator and the MWPC.

PHOton Spectrometer The PHOton Spectrometer (PHOS) is an electromagnetic spectrometer which consists of scintillating crystals and lead-tungstate crystal elements [42; 50]. It has high energy resolution and limited coverage. PHOS is installed at 460 cm from the interaction point at bottom part of ALICE detector. Its η coverage is -0.12 to 0.12 and azimuth coverage is upto 100^o. The main goal of PHOS is to study neutral mesons, like π^0 and η, via their decayed photons.

Electromagnetic Calorimeter The Electromagnetic Calorimeter (EMCal) is a large Pb-scintillator sampling calorimeter with cylindrical geometry [42; 51]. EMCal is installed at 436 cm from the interaction point. Its η coverage is -0.7 to 0.7 and azimuthal coverage is from 80^o to 187^o. The main physics goal of EMCal is to explore the physics of direct photons, neutral pions and jet quenching.

Alice Cosmic Ray Detector The Alice Cosmic Ray Detector (ACORDE) is the ALICE cosmic ray detector which is an array of plastic scintillators [42; 52]. It is placed on the upper surface of the L4 magnet. ACORDE is installed at 8.5 m from the interaction point. Its η coverage is -1.3 to 1.3 and azimuthal coverage is from -60^o to 60^o. It consists of 60 modules. Each ACORDE module consists of two large scintillator counter (each with effective area 190×20 cm^2). Its main objective is to provide a fast (Level-0) trigger signal which is useful in the detector calibration and alignment process and to measure single atmospheric muons in combination with TPC, TRD and TOF.

3.4 Forward Detectors

The forward detectors, installed in the forward region of ALICE, are some specialized small detector systems which are used for triggering events and to determine global event characteristics like collision time, collision vertex, centrality and event plane.

3.4.1 VZERO

The VZERO (V0) detector is used as a Level-0/minimum-bias trigger to reject events that are not suitable for physics analysis, like reactions between beam and gas [42; 53]. The measurement is performed by the measurement of the interaction time with a good time resolution of 1 ns. It consists two arrays of scintillator counters which are placed on either side of the interaction point. The V0A is positioned on the A side of the ALICE with an η acceptance of at 2.8 < η < 5.1 while V0C is located on C side with -3.7 < η < -1.7. The amplitude of the signals from these two detectors are used to estimate the centrality of the collision.

3.4.2 T0

The T0 detector system is similar to the V0 detector and provides the timing signals for Level 0 trigger by measuring the exact interaction time with a precision of 25 ps [42; 53]. It consists of two arrays of Cherenkov counters located on both sides of interaction point. T0A is installed on the A side with an η coverage of 4.61 < η < 4.92 while T0C is on C side of ALICE with -3.28 < η < -2.97. It also provides the reference time for TOF and can be used to reject beam-gas events by estimating the vertex position.

3.4.3 Photon Multiplicity Detector

The Photon Multiplicity Detector (PMD) is built out of two gas proportional chambers and a Pb converter in between [42; 54]. It measures photon multiplicities at pseudorapidities of 2.3 < η < 3.7. The active detector element consists of large array of honeycomb structured gas proportional counters installed in two planes (Charge Plane Veto: CPV and preshower planes) perpendicular to the beam pipe. Each plane of PMD made up of 24 modules and each module consists of 4608 honeycomb cells. A lead converter of thickness 1.5 is sandwiched between the two planes. When a charged particle passes, it generally does not produce any electron shower and thus affects only one cell but when a photon passes through the lead converter, it creates an electromagnetic shower of electrons and positrons and affects many cells. The combined information of CPV and preshower planes helps to identify the photons.

3.4.4 Forward Multiplicity Detector

The Forward Multiplicity Detector (FMD) uses silicon strips to measure the charged-particle multiplicity [42; 53]. The FMD consists of 5 rings which are classified into FMD1, FMD2 and FMD3 based on different positions. These are installed on either side of ITS detector. FMD1 is installed at 320 cm away from the IP and has an η coverage from 3.68 to 5.03. FMD2 has an η coverage of 1.7 to 3.68 while FMD3 has an η coverage of -1.7 to 3.68.

3.4.5 Zero Degree Calorimeter

The Zero Degree Calorimeter (ZDC) has been installed to measure the impact parameter (b) of the collision through measurement of the number of spectator nucleons [42; 55]. It is made of one electromagnetic calorimeter, one neutron and one proton calorimeter on both side of the interaction point at a distance of 116 m from the interaction point.

3.4.6 The Muon Spectrometers

The Muon spectrometer is dedicated for muon detection [42]. It is installed in the C side of ALICE. It is made up of an absorber which absorbs hadrons and photons. It consists of 10 planes of highly granular tracking system, a passive muon-filter wall, four planes of trigger chambers and a large dipole magnet. A front absorber, with length 4.13 m and radiation length $\sim 60X_0$, is placed inside the solenoid magnet which is 503 cm away from interaction point in negative z-direction. There are five tracking stations with spatial resolution of about 100 μm which provides two-dimensional hit information. One of them is placed inside and one of them is placed outside the dipole magnet. Each tracking system consists of two chambers and every chamber consists two cathode planes. There is an iron wall of 1.2 m which is used as muon filter. There are two trigger detectors too which are placed in two planes made from RPC modules. Every trigger planes consists of 18 RPC modules. The dipole magnet is placed at z = -9.94 m from IP, outside the L3 magnet which allows reconstruction of muon momentum. Muon Spectrometer can detect muons in the region -4.0 < η < -2.5. This makes possible to study vector meson resonances like φ meson to quarkonia through their $\mu^+\mu^-$ decay channels as well as to study the unlike sign di-muon continuum up to masses of 10 GeV/c^2.

The various ALICE sub-detectors are summarized in Table 3.2. The acceptance is 360^o in azimuth otherwise specified.

Detector	Acceptance (η,ϕ)	Position (m)	Dimension (m^2)
ITS layer 1,2 (SPD)	±2, ±1.4	0.039, 0.076	0.21
ITS layer 3,4 (SDD)	±0.9, ±0.9	0.150, 0.239	1.31
ITS layer 5,6 (SSD)	±97, ±0.97	0.380, 0.430	5.0
TPC	±0.9 at r=2.8 m	0.848, 2.466	readout 32.5
	±1.5 at r=1.4 m		Volume 90 m^3
TRD	±0.84	2.90,3.68	716
TOF	±0.9	3.78	141
HMPID	±0.6,$1.2^o < \phi < 58.8^o$	5.0	11
PHOS	±0.12,$220^o < \phi < 320^o$	4.6	8.6
EMCal	±0.7,$80^o < \phi < 187^o$	4.36	44
ACORDE	±1.3,$-60^o < \phi < 60^o$	8.5	43
Muon Spectrometer			
Tracking station 1	$-2.5< \eta < -4.0$	-5.36	4.7
Tracking station 2		-6.86	7.9
Tracking station 3		-9.83	14.4
Tracking station 4		-12.92	26.5
Tracking station 5		-14.22	41.8
Trigger station 1	$-2.5< \eta < -4.0$	-16.12	64.6
Trigger station 2		-17.12	73.1
ZDC:ZN	$\|\eta\| < 8.8$	±116	2×0.0049
ZDC:ZP	$6.5 < \eta < 7.5$,	±116	2×0.027
	$-9.7^o < \phi < 9.7^o$		
ZDC:ZEM	$4.8 < \eta < 5.7$,	7.25	2×0.0049
	$-16^o < \phi < 16^o$ and		
	$164^o < \phi < 196^o$		
PMD	$2.3 < \eta < 3.7$	3.64	2.59
FMD disc 1	$3.62 < \eta < 5.03$	inner: 3.2	
FMD disc 2	$1.7 < \eta < 3.68$	inner: 0.834	0.266
		outer: 0.752	0.266
FMD disc 3	$-3.4 < \eta < -1.7$	inner: -0.628	
		outer: -0.752	
V0A	$2.8 < \eta < 5.1$	3.4	0.548
V0C	$-1.7 < \eta < -3.7$	-0.897	0.315
T0A	$4.61 < \eta < 4.92$	3.75	0.0038
T0C	$-3.28 < \eta < -2.97$	-0.727	0.0038

Table 3.2: Summary of the ALICE detector subsystems [42]

3.5 Data Acquisition and Event Reconstruction

In ALICE, the online processes are referred as the processes which have been done in real time (when the event is taking place) while offline processes are the activities independent of the actual event time [42]. The task of the data acquisition (DAQ)is to build events by collecting and combining informations from several detectors for a given event. The information about data taking conditions are also required.The system has been designed to buffer events and export the information to a permanent storage known as CASTOR. The ALICE DAQ system is able to handle a data rate of up to 1.25 GB/s. A two-level trigger system decides whether an event is interesting enough to read out all the sub-detectors and write it to storage. In the first step, a hardware trigger (Central Trigger Processor (CTP)), provides a fast decision on three levels using the detector signals. The decision time on the highest level (L2/Level-2) is comparable to the TPC drift time. The CTP can be used to avoid problems due to pile-up can by allowing only a certain number of high-multiplicity events in a certain time window. In the second step, the High-Level Trigger (HLT), which is essentially a farm of about 1000 computers processing the data in parallel, carries out an online event reconstruction per sub-detector. It performs a fast analysis to allow for more sophisticated triggers(high-energy jets or muon pairs). After the raw data produced by ALICE DAQ system is stored, the offline reconstruction of events is followed. ALICE produces 10-15 Peta Byte data on an average per year. The raw data size of a central Pb−Pb event is $\sim$ 14 MB and the output data size for an event is around 3 MB after reconstruction. The reconstruction and analysis of such a huge amount of data requires highly efficient computing resources which can not be provided at CERN only. This requirement led to the concept of grid which combines several computing resources at different locations to be used in the ALICE. The ALICE grid uses currently 53 computing center present in different collaborative countries. The so-called GRID middle-ware used in the ALICE is ALICE Grid Environment (AliEn) which provides a user interface and integration in ROOT framework to perform data analysis. The framework used for reconstruction and analysis of the data recorded by ALICE as well as for the simulation of Monte-Carlo events is called AliRoot. It is a software package based on ROOT and written in C++ programming language. During a Monte-Carlo event simulations using AliRoot package, a collision is simulated by an event generator which is interfaced with AliRoot software package. There are various event generators like PHYTHIA, PHOJET etc for simulating p−p collision events, HIJING, Therminator etc for simulating Pb−Pb collision events. The event generators produce a kinematics tree which contains the full particle informations like PDG, momentum etc. The generated particles from event generators are propagated through modeled ALICE detector environment. This is done by simulation tools like Geant3, Geant4 or Fluka which are modeled with ALICE detector system. The generated particles from the event generators can interact with the detector material and may produce secondary particles emulating the real collisions. These signals caused by interaction of particles with an active detector region are called *hits*. The detector response to these hits is simulated resulting in digits (ADC counts). At this point, the simulated detector response and the signals measured in real collisions are comparable and hence the following steps are identical for both simulated and real collision data. The signals of detectors which are close in space and/or time are combined to form clusters to reduce noise. This process is carried out for every ALICE sub-detector individually. The cluster from all ALICE sub-detectors are combined to tracks. This begins with the TPC using a Kalman-Filter procedure. The particle momentum and identity are extracted from the extracted track curvature and the specific energy-loss in the medium. The primary and secondary vertices are reconstructed from the tracks or from several track segments.The extracted information from the reconstruction is stored as an *Event Summary Data (ESD)* object. The ESDs can be further filtered based on specific analysis and can be stored in *Analysis Object Data (AOD)*.

Chapter 4

Pion-kaon femtoscopy in Pb−Pb collisions at $\sqrt{s_{\rm NN}}$= 2.76 TeV measured with ALICE at the LHC

"It doesn't matter how beautiful your theory is, it doesn't matter how smart you are. If it doesn't agree with experiment, it's wrong." – Richard P. Feynman

Abstract: This chapter describes the experimental pion-kaon femtoscopy analysis. It contains detailed information about the experimental data set, analysis software, various event cuts, track cuts and PID cuts required to carry out this analysis as well as background corrections necessary for getting meaningful correlation function. This chapter briefly discusses the fitting method and systematic error analysis.

4.1 Pion-kaon femtoscopic correlations

The main goal of heavy-ion collisions at LHC is to create and study QGP like medium. The equation of state of such a system is not yet determined. The study of bulk properties of matter produced in heavy-ion collisions can only be done by systematic spatio-temporal analysis of the system, experimentally. The spatio-temporal information of the system can be easily extracted using femtoscopic techniques [56]. The femtoscopic studies of identical mesons provide insights about the dimension of the system produced in heavy ion collisions. The non-identical particle femtoscopic studies give not only information about source dimension but also about the emission asymmetries (first moment of the correlation function) between different particle species. The observation of such an emission asymmetry can be related to the hydro-motivated collective evolution of the system created in heavy-ion collisions. The primary aim of this thesis is the measurement of the femtoscopic correlations between charged pions and kaons in Pb−Pb collisions at $\sqrt{s_{\mathrm{NN}}}$= 2.76 TeV recorded by the ALICE detector at the LHC during 2011 data taking period.

4.1.1 Experimental Data sample

The pion-kaon femtoscopy analysis was performed in Pb−Pb collisions at $\sqrt{s_{\mathrm{NN}}}$= 2.76 TeV collected in 2011. The analysis was carried out for both positive and negative polarity of the magnetic field. The events were selected on basis of a trigger configuration which required the conincidence of the signals in the VZERO-A and VZERO-C detectors. The timing information provided by the Zero Degree Calorimeter (ZDCs) and the VZERO detectors was used to remove the beam gas events. The minimum-bias events were triggered by the coincidence of signal in the VZERO detector and the Silicon Pixel Detector (SPD) of the ITS detector. About 18.5 million events for positive magnetic field polarity and 23.2 million events for negative magnetic field polarity have been analyzed using the technical production $LHC11h - pass2$ by ALICE detector. The analysis has been performed over three tupe of triggered events namely central, semi-central and peripheral collisions determined by the sum of the VZERO-A and VZERO-C amplitudes. In terms of centrality percentile, the analysis has been performed in seven centrality bins- 0-5%, 5-10%, 10-20%, 20-30%, 30-40%, 40-50% and 50-90%. The events, for which the z position of reconstructed vertex was within 10.0 cm with respect to the nominal interaction point of the ALICE detector, have been selected for analysis. The distribution of the z position of the primary vertex is shown in Figure 4.1.

4.1.2 Analysis Software

The ALICE software package which has been used for this particular analysis is AliFemto package which is a part of AliRoot and AliPhysics framework. The code can be found in the official repository of ALICE Collaboration codes used to perform specific analysis.

`https://github.com/alisw/AliPhysics/tree/master/PWGCF/FEMTOSCOPY`

The analysis has been run on the GRID using the CF_PbPb LEGO train with the latest versions of AliRoot and AliPhysics. The LEGO trains can be found at: `https://alimonitor.cern.ch/trains/` The configuration file can be found on the following link:

https://github.com/alisw/AliPhysics/tree/master/PWGCF/FEMTOSCOPY/macros/Train/NonIdParticleFemto/PionKaonFemto

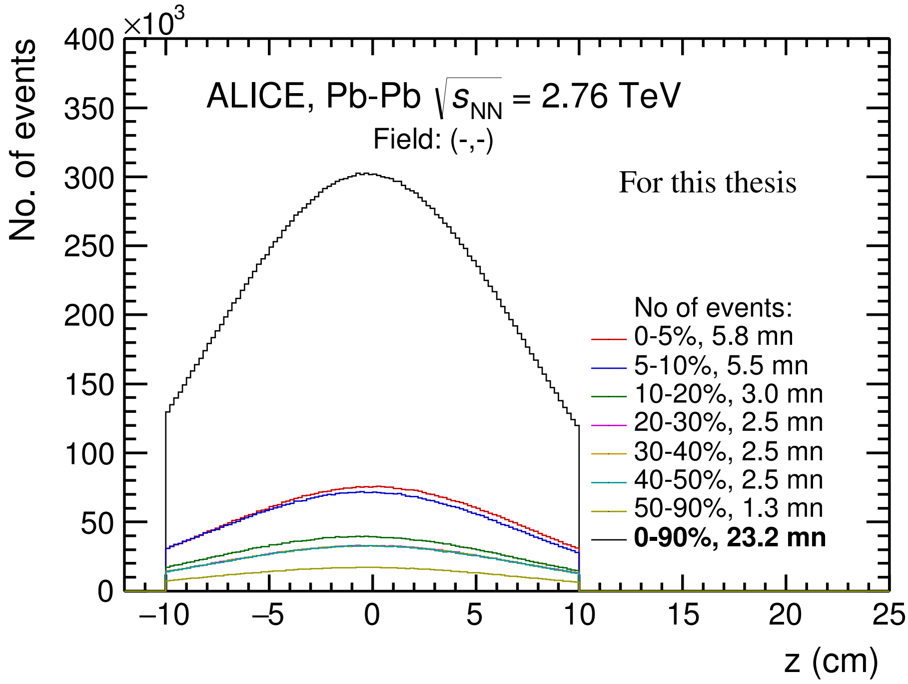

Figure 4.1: The distribution of z position of primary vertex for negative polarity of magnetic field for Pb−Pb collisions at $\sqrt{s_{NN}}$= 2.76 TeV recorded by ALICE at the LHC.

4.1.3 Track selection

The track selection was based on charged tracks reconstructed using the TPC detector only. The azimuthal angle (ϕ) distribution is not uniform for global tracks due to acceptance holes in ITS detector. Therefore, TPC-only tracks were considered for this analysis. The reconstructed tracks are required to have at least 50 reconstructed space points (or clusters) out of a maximum of 159 in the TPC. A Kalman fit is performed to these space points with an additional constraint that the track has to pass through the primary vertex. The χ^2/ndf of the fit is required to be less than 4. The distance of closest approach (DCA) of a track to the primary vertex in the transverse (DCA_{xy}) and longitudinal (DCA_z) directions is required to be less than 2.4 cm and 3.2 cm respectively. The DCA cuts are imposed to reduce the contamination from secondary tracks originating from weak decays and from interaction with the detector material. Tracks with 0.19 GeV/c < p_T < 1.5 GeV/c (Figure 4.2, 4.3) measured within the pseudo-rapidity range $|\eta|$ < 0.8 (Figure 4.4, 4.5) were accepted for the analysis. A low p_T cutoff is used to reduce event-by-event biases from smaller reconstruction efficiency at lower p_T. The tracks

p_T	[0.19, 1.5] GeV/c
η	[-0.8, 0.8]
Bit 7 (128)	TPC only tracks,constrained to SPD vertex in the filter
Minimum number of TPC clusters	50 out of a maximum 159
χ^2/ndf of the fit	< 4
SetAcceptKinkDaughters	kFALSE
DCA_z	< 3.2
DCA_{xy}	< 2.4 cm
SetDCAToVertex2D	kTRUE

Table 4.1: Various track quality cuts used to select tracks for a selected event.

with kinks (the tracks that appear to change direction due to multiple scattering and decay) are rejected. The details of the track-cuts can be found in Table 4.1 .

4.1.4 Particle identification

In order to carry out the analysis, a reliable identification of tracks as pions and kaons is very important. In the present analysis, the combined information of the TPC and TOF detectors are used for particle identification. The particle identification is based on the specific energy loss (dE/dx) of the particle in the TPC while the time of flight information is used for the TOF detector. A track is identified as a pion or kaon depending on the value of $n\sigma_{TPC/TOF}$ which is defined as the following for both TPC and TOF detectors:

The $n\sigma$ for TPC is based on the specific energy loss

$$n\sigma_{TPC} = \frac{dE/dx_{meas} - dE/dx_{exp}}{\sigma_{TPC}} \tag{4.1}$$

Here, dE/dx_{meas} is the specific energy loss measured in the TPC gas, dE/dx_{exp} is the energy loss calculated using parametrized Bethe-Bloch formula and σ_{TPC} is the TPC dE/dx resolution.

Similarly, the $n\sigma$ for TOF is based on the time of flight measurement of the track detected by TOF.

$$n\sigma_{TOF} = \frac{TOF_{meas} - TOF_{exp}}{\sigma_{TOF}} \tag{4.2}$$

The TOF_{meas} and TOF_{exp} corresponds to the measured and expected time of flight for a given particle species, respectively while σ_{TOF} corresponds to the TOF resolution. The detailed description of the particle identification is given in Ref. [57]

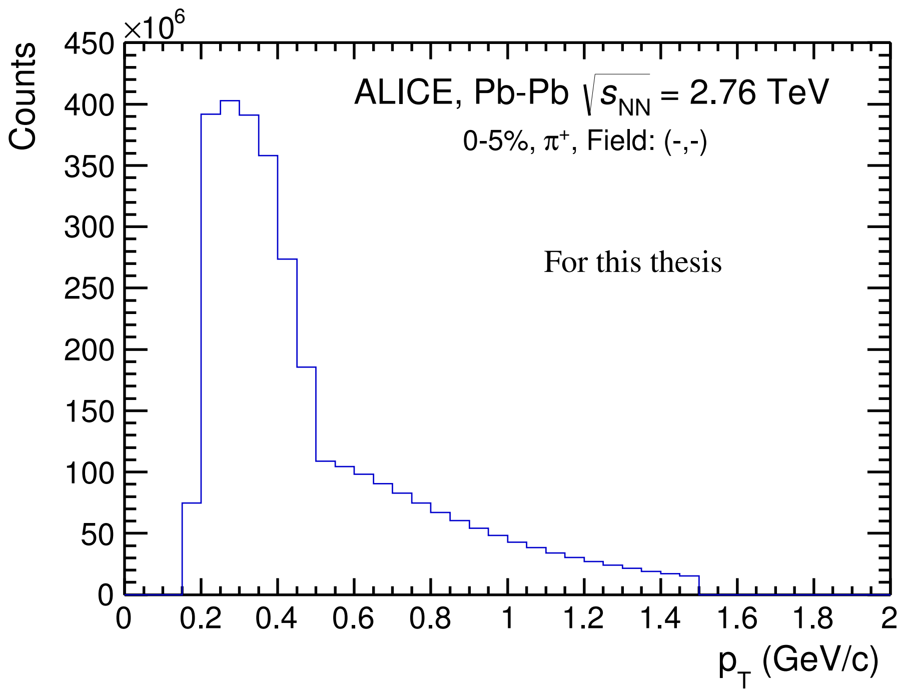

Figure 4.2: p_T distribution of charged pions for Pb–Pb collisions at $\sqrt{s_{NN}}$= 2.76 TeV recorded by ALICE at the LHC (0-5% central)

The variation of TPC dE/dx with momentum for pions and kaons is shown in Figure 4.6 and Figure 4.8, respectively. The TOF expected time distribution versus momentum for pions and kaons is shown in Figure 4.7 . and Figure 4.9 , respectively. The various $n\sigma_{TPC}$ and $n\sigma_{TOF}$ cuts used for selecting charged pions and kaons are given in Table 4.2.

4.1.5 Pair selection

The accepted tracks from each event are combined into pairs for all charge combinations. The pairs formed out of tracks with small angular difference can be affected by reconstruction effects. Hence, two-particle detector acceptance effects must be taken into account in this procedure. The pair level selection is also necessary for the removal of spurious correlations due to detector effects. In this analysis, two type of pair selection cuts were found to be effective and were implemented. These cuts are described in the following sections.

Removal of track pairs with merged TPC clusters The trajectories of the tracks used in the analysis are reconstructed from sets of clusters in the TPC. A TPC cluster has a typical size of 5 padrows in the $r - \varphi$ direction, corresponding to 2.5 cm and 3 cm in the inner and outer part of the TPC sector, respectively. When two clusters are spatially

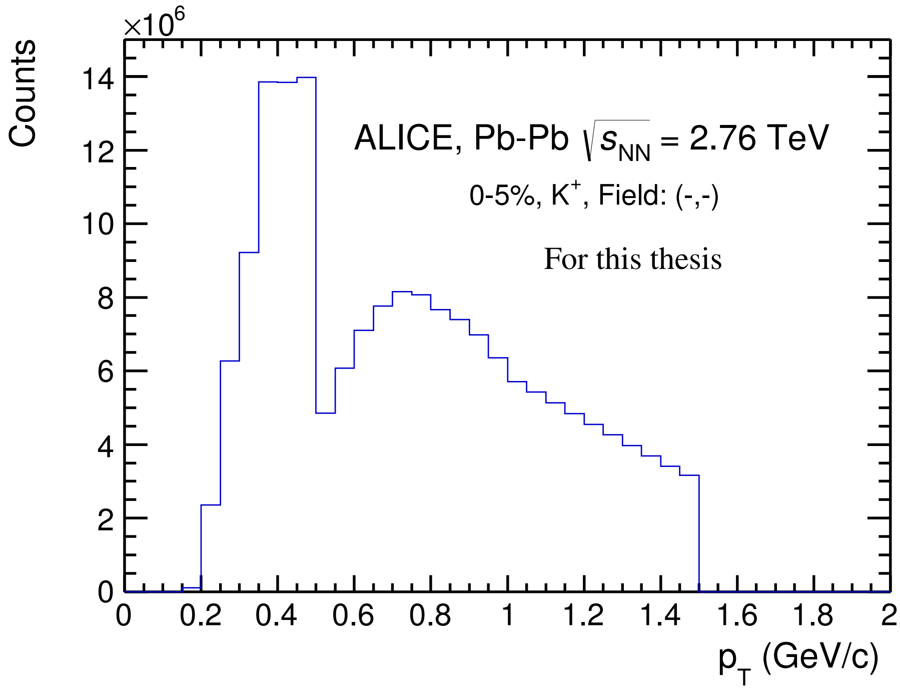

Figure 4.3: p_T distribution of charged kaons for Pb−Pb collisions at $\sqrt{s_{\rm NN}}$= 2.76 TeV recorded by ALICE at the LHC (0-5% central)

close in the TPC volume, their signals may overlap. This may result in the inability to reconstruct one of the tracks, or both of them. Such effect is called "merging". The ALICE tracking algorithm is designed to handle such cases. However if the two clusters overlap, the reconstruction algorithm automatically rejects such clusters from any $\mathrm{d}E/\mathrm{d}x$ determination. As a result, even if the momenta of both tracks are correctly reproduced, their $\mathrm{d}E/\mathrm{d}x$ measurement may be distorted or of lesser quality, and such tracks can be rejected by the track quality cuts.

Cut on fraction of shared clusters In general, for the high-multiplicity collisions, the produced tracks can be very close to each other. As a result, the track clusters[1] may be merged affecting the particle reconstruction algorithm. As a result, some pairs of tracks cannot be disentangled and they are reconstructed as one track. Therefore, a cut was applied to remove all such pairs of tracks which share more than 5% of their overall number of registered hits in TPC. If the track reconstruction algorithm was not able to distinguish

[1]Cluster is a region in TPC, where traversing particle induced a signal on a given padrow. In order to induce a signal particle must produce a charge, which is higher than the threshold, and fulfil all other necessary criteria. There are 159 padrows per TPC sector, so the maximum number of clusters that particle can produce is 159.

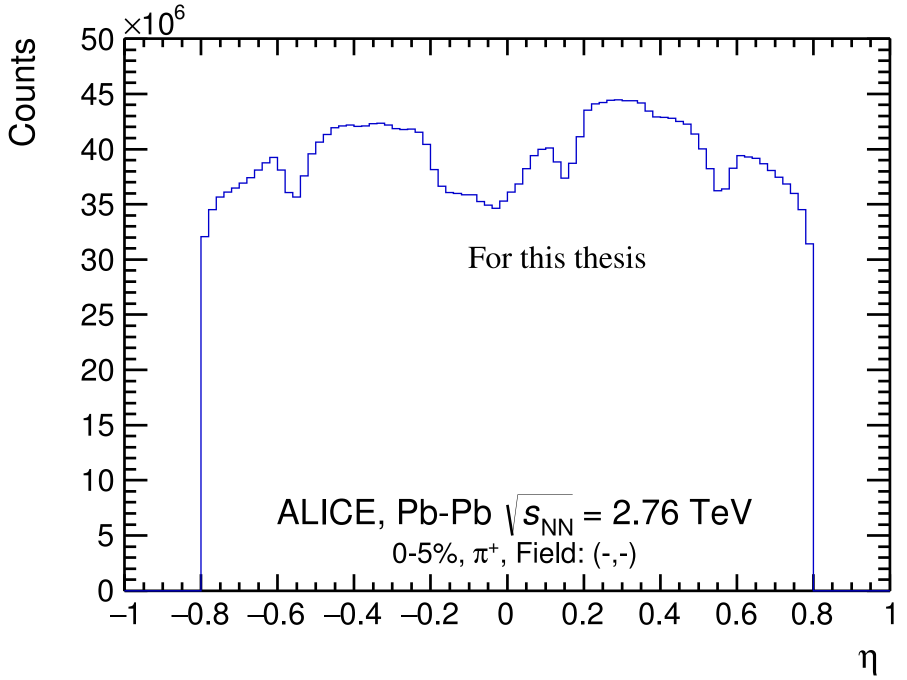

Figure 4.4: η distribution of charged pions for Pb−Pb collisions at $\sqrt{s_{\rm NN}}$= 2.76 TeV recorded by ALICE at the LHC (0-5% central)

two hits and these two tracks share the same space point in TPC, the corresponding hit in TPC is marked as "shared".

Cut for electron-positron pair removal The residual correlations appearing in the unlike-sign pairs could not be completely removed by the track merging cuts. The fake correlations were identified as electron-positron pairs originating from γ conversion. These pairs were misidentified as a pion or a kaon and hence contributed to the signal. Hence, a cut for electron-positron pairs, called the $\overline{\gamma}$ cut is applied in order to remove unnecessary effect of γ conversion. The dE/dx signals of the produced e^+ and e^- pairs may overlap with the dE/dx bands of pions and kaons and may be misidentified as an unlike-sign pair of pion and kaon. The pion-kaon pair with momenta p_1 and p_2 is removed if their invariant mass $M_{\rm inv} = 2m_e^2 + 2(E_1E_2 - \vec{p}_1 \cdot \vec{p}_2)$ is less than 0.002 GeV/c and polar angle difference $\Delta\theta = |\theta_1 - \theta_2|$ is less than 0.008 radian, where m_e is the electron mass.

Cut on merged fraction of points This pair cut aims to remove the detector effects by constraining the merged fraction of points. Even if the tracks with shared hits are removed by applying cuts on shared clusters, the tracking algorithm may not mark two closely lying tracks as "shared" if the two different tracks are closer than the average

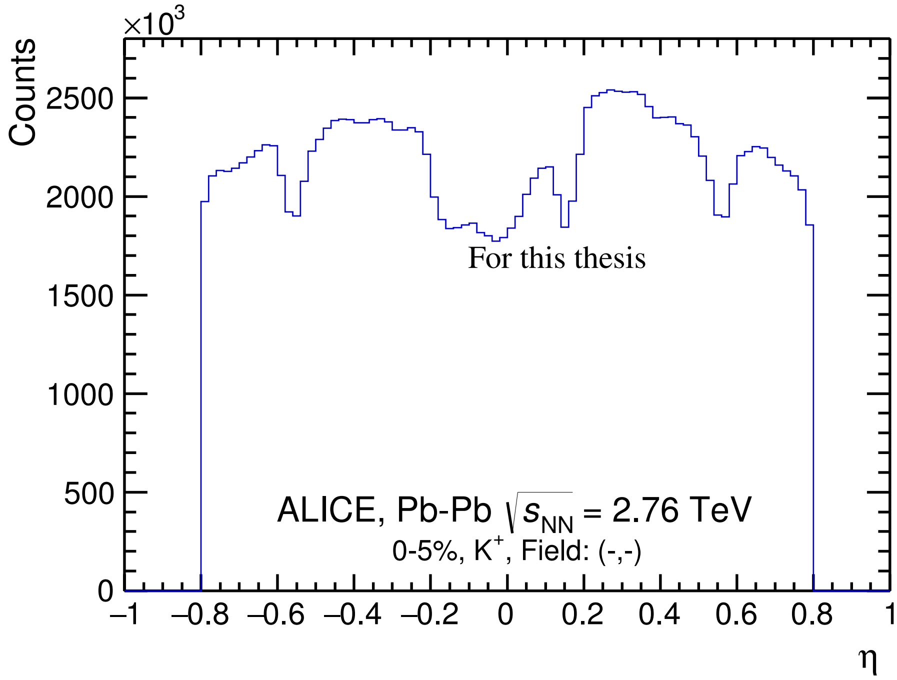

Figure 4.5: η distribution of charged kaons for Pb−Pb collisions at $\sqrt{s_{\mathrm{NN}}}$= 2.76 TeV recorded by ALICE at the LHC (0-5% central)

cluster size in TPC. The probability of finding such pairs is high when $\Delta\eta < 0.01$ for such pairs. For such pairs, the helices of the two tracks are projected on the plane perpendicular to the beam axis and the distance, d between these two helices are checked at a step size of 1 cm starting from $d = 0.8$ m and $d = 2.5$ m (the range covered by TPC). If d is found to be smaller than 3 cm (the average TPC cluster size), these points are marked as "merged". The fraction of merged points or the merged fraction(MF) is calculated as :

$$MF = \frac{N_{pass}}{N_{total}} \tag{4.3}$$

where N_{pass} is the number of merged points and N_{total} is the total number of steps (of step size 1.0 cm) in the selected range. The track pairs are removed if their MF is higher than the selected value. As previously discussed in chapter 2, the Double ratio in $Side$ direction is expected to be unity due to symmetry considerations. However, due to the limited detector resolution effects, it is shifted from unity in small $k*$ region. It is necessary to obtain the best cut which minimizes the unwanted detector signals. The $(C+/C-)_{Side}$ components after applying different combinations of MF cuts are used to obtain the best MF cut as these components should be flat at unity in case of absence of the merging effect. A chi-square test was performed to obtain the best set of merged fraction cut.

Particle	$n\sigma$ for TPC and TOF
Pion	$n\sigma_{TPC} < 3.0$ for $\lvert p\rvert < 500$ MeV/c, $\sqrt{(n\sigma^2_{TPC} + n\sigma^2_{TOF})} < 3.0$ for $\lvert p\rvert > 500$ MeV/c
Kaon	$n\sigma_{TPC} < 2.0$ for $\lvert p\rvert < 400$ MeV/c, $n\sigma_{TPC} < 1.0$ for 400 MeV/c $< \lvert p\rvert <$ 450 MeV/c, $n\sigma_{TPC} < 3.0$ and $n\sigma_{TOF} < 2.0$ for 450 MeV/c $< \lvert p\rvert <$ 800 MeV/c, $n\sigma_{TPC} < 3.0$ and $n\sigma_{TOF} < 1.5$ for 800 MeV/c $< \lvert p\rvert <$ 1000 MeV/c, $n\sigma_{TPC} < 3.0$ and $n\sigma_{TOF} < 1.0$ for $\lvert p\rvert > 1000$ MeV/c

Table 4.2: $n\sigma$ cuts given for pion and kaon identification for Pb−Pb collisions at $\sqrt{s_{\rm NN}}$= 2.76 TeV recorded by ALICE at the LHC

The results were obtained using the following formula:

$$\chi^2_{ndf(Side)} = \frac{1}{n}\sum_{i=1}^{n}\left(\frac{(C+/C-)_{Side}(k_i^*) - 1}{\sigma_i(Side)}\right)^2, \tag{4.4}$$

where: χ^2_{ndf} is the value of chi-square divided by number of degrees of freedom, n is number of considered data points, $\sigma_i(Side)$ refers to the error associated with $(C+/C-)_{Side}$. The values of χ^2_{ndf} were calculated for $0.0 \le k^* \le 0.2$ GeV/c, where the femtoscopic correlations are dominant. The tables 4.3 and 4.4 show the result for χ^2/ndf test for 0-5% centrality class for like-sign and unlike-sign pairs respectively. The results for other centrality classes show a similar trend. It was found from this test that the set of two-track cuts with MF 1% and $\overline{\gamma}$ cut has the lowest value of χ^2_{ndf} for unlike-sign pairs. A cut of MF 7% was found suitable for like-sign pairs.

Pair	**Magnetic Field**	χ^2/ndf **for no paircut**	χ^2/ndf **for 1% MF cut**	χ^2/ndf **for 3% MF cut**	χ^2/ndf **for 7% MF cut**
π^+K^+	+ve	5.4976	2.4188	2.4310	2.2936
π^-K^-	+ve	6.2763	2.3971	2.4165	2.4859
π^+K^+	-ve	6.9418	1.9611	1.8666	1.8129
π^-K^-	-ve	7.4470	2.2219	2.2031	2.1611
Average		6.5407	2.2497	2.2293	2.1883

Table 4.3: χ^2/ndf test result for like-sign pairs of charge pions and kaons for 0-5% centrality class for Pb−Pb collisions at $\sqrt{s_{\rm NN}}$= 2.76 TeV recorded by ALICE at the LHC

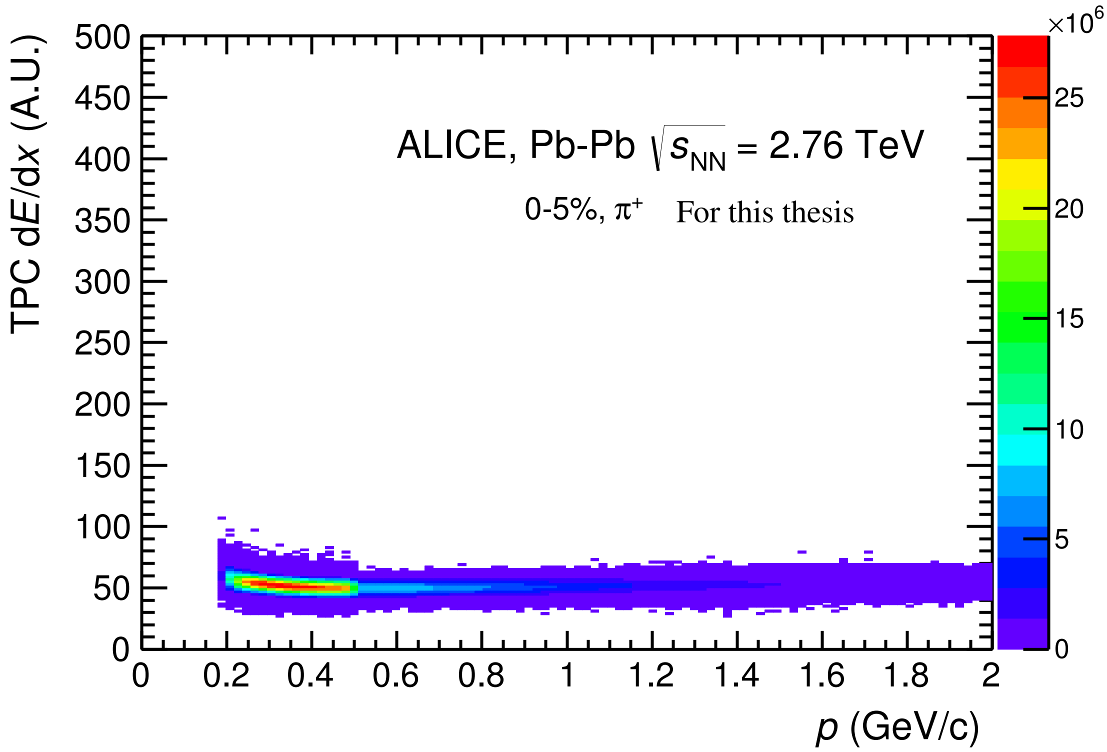

Figure 4.6: Variation of dE/dx versus momentum for pions for Pb−Pb collisions at $\sqrt{s_{\mathrm{NN}}}$= 2.76 TeV recorded by ALICE at the LHC (0-5% central)

4.1.6 Purity and primary fraction calculation

One of the important part of the analysis requires the correct identification of the particles considered. It should be noted that all the selected pairs do not contribute to the observed correlation. One of the major reasons could be the particle misidentification where one misidentifies a pion or a kaon for another particle. The other major cause can be the effect of decays where one particle from the pair can come from a decay of another particle. This is also known as secondary contamination.

The purity of the particle refers to the ratio of the number of correctly identified particles to the total number of particles identified as the selected type. This was calculated using the HIJING Monte Carlo generator [58]. The generated particles were passed through the same particle identification algorithm as done for real data. The results for 0-5% centrality class is shown in Figure 4.10. The figure shows the number of correctly identified particles by the particle identification algorithm and the number of misidentified particles as other ones. The purity (p) of pions and kaons were calculated by dividing the number of correctly identified particles by the total number of particles identified as the selected type. The purity of pion sample is about 99.6% for all centrality classes while

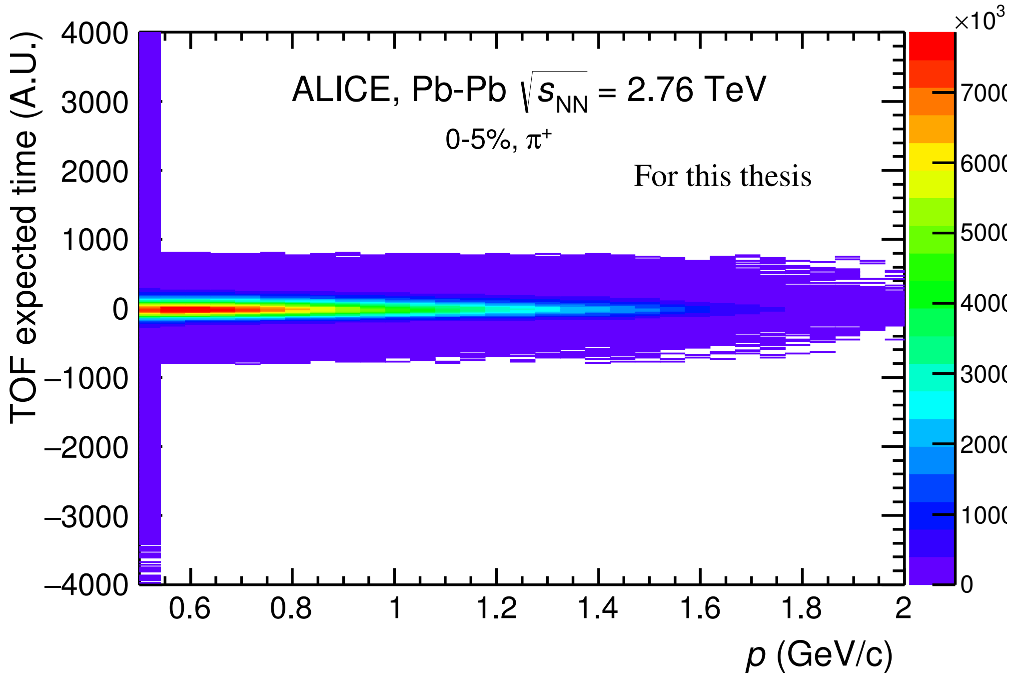

Figure 4.7: TOF expected time versus momentum for pions for Pb−Pb collisions at $\sqrt{s_{NN}}$= 2.76 TeV recorded by ALICE at the LHC (0-5% central)

the purity of kaon sample varies from 81% to 84% for most central to peripheral events (Figure 4.11).

The fraction of primary particles ('f') is estimated by dividing the number of primary particles (of a selected type) by the total number of particles of the same type. The values of the primary fraction for pions and kaons for different centrality classes are given in table 4.5.

4.1.7 Momentum resolution correction

Another important correction which is implemented is the correction due to finite momentum resolution. It is not applied to the data directly but the effects are passed into the fitting procedure. The effect was estimated using the Monte Carlo data generated with HIJING generator. The generated events are passed through the same reconstruction algorithm as used for real data analysis. For example, at the generated level, the real momentum p_{real} of the particle is known and at the reconstructed level one can fetch the reconstructed momentum p_{reco}. The momentum deviation (p_{real} - p_{reco}) were estimated by fitting Gaussian functions for different p_{reco} ranges. The spread (also known as smear sigmas) was determined by extracting the value of the standard deviation. This method was also carried out for θ and φ angles of the particle. The variation of the smear sigmas,$\sigma_{\delta p}$,

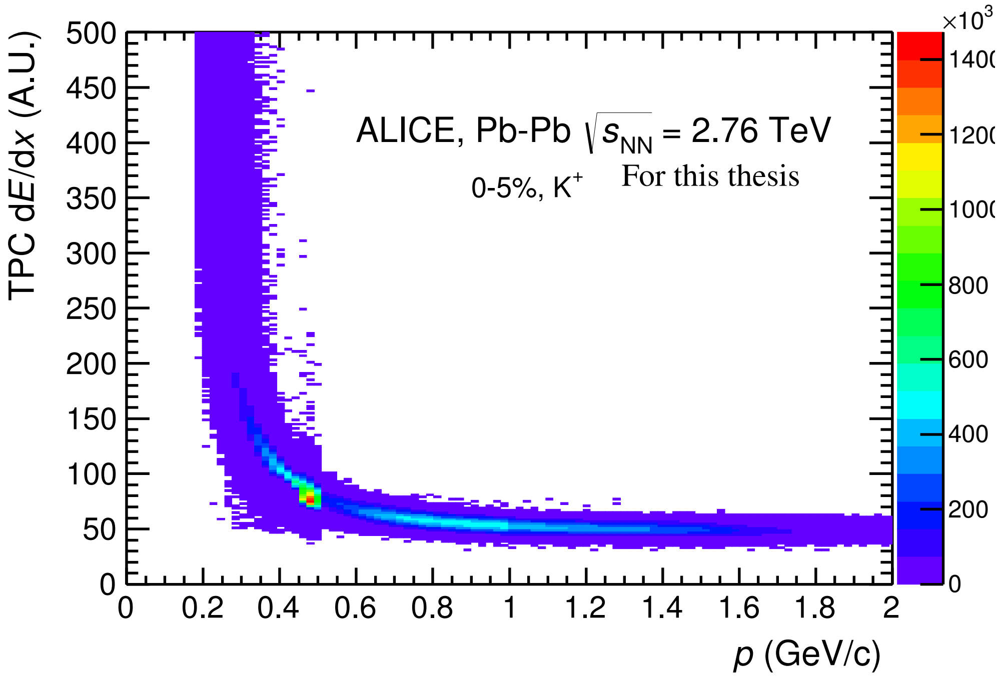

Figure 4.8: Variation of dE/dx versus momentum for kaons for Pb−Pb collisions at $\sqrt{s_{\rm NN}}$= 2.76 TeV recorded by ALICE at the LHC (0-5% central)

$\sigma_{\delta\phi}$, and $\sigma_{\delta\theta}$ was studied as a function of $p_{\rm reco}$. The obtained results were fitted with following functions as described in [59].

$$f_{\rm p}(p_{\rm reco}) = a_{\rm p} + b_{\rm p}(p_{\rm reco})^{c_{\rm p}}, \tag{4.5}$$

$$f_{\theta}(p_{\rm reco}) = a_{\theta} + b_{\theta}(p_{\rm reco})^{c_{\theta}}, \tag{4.6}$$

$$f_{\varphi}(p_{\rm reco}) = a_{\varphi} + b_{\varphi}(p_{\rm reco})^{c_{\varphi}}, \tag{4.7}$$

where $f_{\rm p}(p_{\rm reco})$, $f_{\theta}(p_{\rm reco})$, and $f_{\varphi}(p_{\rm reco})$ are the form of the fitting functions to the deviations of momentum, θ angle, and φ angle, respectively, and a, b, and c are the parameters of these functions. This particular form of the fitting function and the extracted values of the nine parameters were given as an input in the fitting algorithm to estimate the momentum resolution correction. The data obtained from MC simulations, together with fits, which is used in this analysis are obtained from the analysis using spherical harmonics [59] and is presented in Figure 4.12.

4.1.8 Non-femtoscopic background correction

The measured experimental femtoscopic correlation function also contains other event-wide correlations projected to the two-particle space as discussed in chapter 2. The

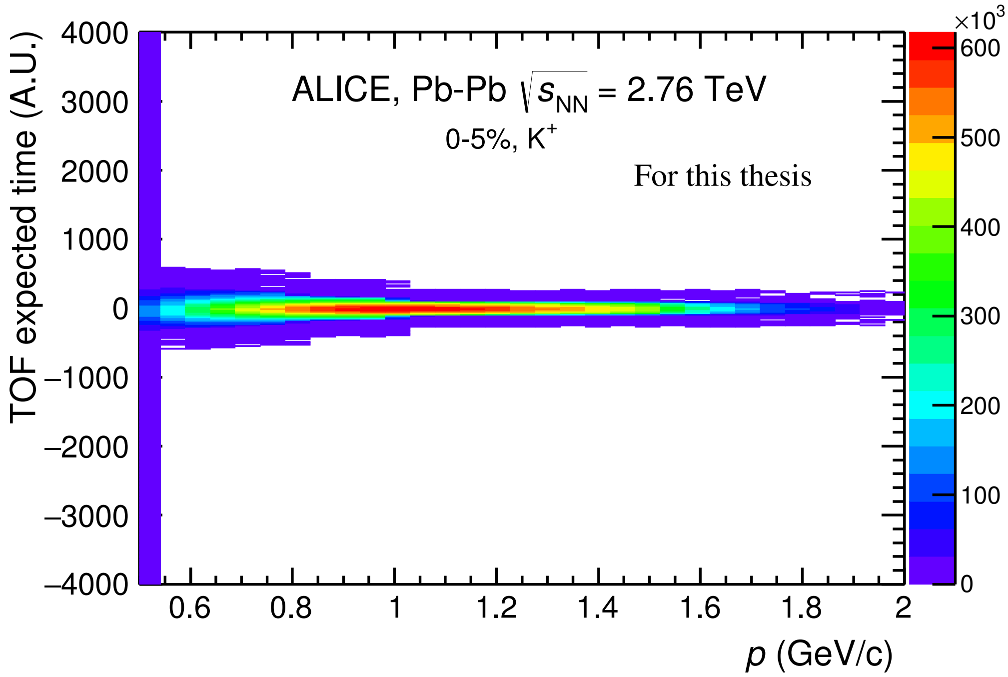

Figure 4.9: TOF expected time versus momentum for kaons for Pb−Pb collisions at $\sqrt{s_{NN}}$= 2.76 TeV recorded by ALICE at the LHC (0-5% central)

sources of these correlations can be elliptic flow v_2, global conservation of energy and momentum, resonance decay correlations, residual correlations (remnants of the femtoscopic correlations between parent particles, which decayed weakly into the particles of interest) and others. The observed non-flat background at large $k*$ also indicates that the background at lower values of $k*$ may not be flat either. Therefore, It is necessary to remove the non-femtoscopic background before carrying out the further procedures of fitting and extracting relevant parameters. The procedure for correcting the background is discussed in the following.

The experimental correlation function can be written as the sum of real femtoscopic correlations and the contribution from the background sources. This is given by the following expression:

$$C^{ij}_{exp} = B^{ij} + |\psi^{ij}|^2 \tag{4.8}$$

where C^{ij}_{exp} is the experimental correlation function, B^{ij} is the non-femtoscopic background contribution, and $|\psi^{ij}|^2$ is the real correlation (C^{ij}_{real}) between the pairs. The background function had been assumed to be a 6^th order polynomial given by following expression:

$$B^{ij} = a^{ij}_0 + \sum_{l=1}^{5} a_l k^{*(l+1)} \tag{4.9}$$

Pair	**Magnetic Field**	χ^2/ndf **for no paircut**	χ^2/ndf **for 1% MF cut**	χ^2/ndf **for 3% MF cut**	χ^2/ndf **for 7% MF cut**
π^-K^+	+ve	1.3168	1.0588	1.2069	1.2820
π^+K^-	+ve	2.8674	2.1149	2.1333	2.3948
π^-K^+	-ve	1.7220	1.2660	1.2785	1.1984
π^+K^-	-ve	2.2667	1.7491	1.6335	1.7308
Average		2.0432	1.5472	1.5630	1.6515

Table 4.4: χ^2/ndf test result for unlike-sign pairs of charge pions and kaons for 0-5% centrality class for Pb−Pb collisions at $\sqrt{s_{\rm NN}}$= 2.76 TeV recorded by ALICE at the LHC

The fitting was done for both magnetic fields and all centrality bins separately by minimizing $\chi^2_{background}$ given by:

$$\chi^2_{background} = \frac{1}{\sigma^2_{tot}}\left[(C^{++}-B) - \frac{1}{(C^{+-}-B)}\right]^2 + \frac{1}{\sigma^2_{tot}}\left[(C^{--}-B) - \frac{1}{(C^{+-}-B)}\right]^2$$
$$+\frac{1}{\sigma^2_{tot}}\left[(C^{++}-B) - \frac{1}{(C^{-+}-B)}\right]^2 + \frac{1}{\sigma^2_{tot}}\left[(C^{--}-B) - \frac{1}{(C^{-+}-B)}\right]^2 \quad (4.10)$$

where σ_{tot} is the sum of σ's for all pairs for each bin of k^*.

The real correlation function can be expressed by following expression:

$$C^{ij}_{real} = C^{ij}_{exp} - B^{ij} \quad (4.11)$$

Before performing the background subtraction, the σ_i value of the correlation function in each (k^*_i) bin was recalculated as the following :

$$\sigma_{\rm new}(k^*_i) = \sqrt{\sigma^2_{\rm old}(k^*_i) + \sigma^2_{\rm av.dist.}}, \quad (4.12)$$

where $\sigma_{\rm old}$ corresponds to the previously existing error on the correlation function in a particular (k^*) bin and $\sigma_{\rm av.dist.}$ is the average deviation of the value of correlation function from unity in the range 0.18 − 0.25 GeV/c. The average deviation is calculated using all charge combinations of pairs of particles for two different magnetic field polarities separately. The selected k^* range corresponds to the region where the C_{exp} should be flat at unity. One needs to add this additional component to the correlation function uncertainty because the C_{exp} is non-uniform at unity due to imperfect normalization of the correlation function. The detailed description of the background correction method can be found in [60].

Centrality (in %)	**Magnetic Field**	**Value of 'f'for π^+**	**Value of 'f'for π^-**	**Value of 'f'for K^+**	**Value of 'f'for K^-**
0-5%	+ve	0.92596	0.924682	0.996294	0.993394
	-ve	0.925814	0.924359	0.995723	0.993722
5-10%	+ve	0.925919	0.924364	0.996304	0.992917
	-ve	0.925672	0.924054	0.99575	0.993169
10-20%	+ve	0.925591	0.923829	0.996164	0.992182
	-ve	0.0.925491	0.9235	0.995689	0.992544
20-30%	+ve	0.925159	0.922318	0.996264	0.990525
	-ve	0.0.924819	0.922121	0.995671	0.990972
30-40%	+ve	0.923838	0.919746	0.996148	0.988163
	-ve	0.0.923691	0.919744	0.995671	0.988476
40-50%	+ve	0.921741	0.915947	0.996001	0.984427
	-ve	0.921515	0.915647	0.995404	0.985384

Table 4.5: The values of primary fraction for pion and kaons for different centrality classes

4.2 Fitting Correlation Function

After obtaining the correlation function, one needs to extract the information about the source size and emission asymmetry. This is achieved by fitting the correlation function with CorrFit software [61; 38] which was developed to describe the correlation function at RHIC energies. In previous femtoscopic measurements which involved identical particles, the source information was extracted by fitting the correlation function which contained either Bose-Einstein correlations or Fermi-Dirac correlations. All the other sources of correlations which constitutes the Final State Interactions(FSI) are factored out and are corrected for in the analysis. In order to extract the source size, the form of the source function is also assumed to be three dimensional Gaussian function. However, in case of non-identical particle femtoscopy, one cannot simply correct for the FSI's as they are the dominant source of correlation. The source model cannot be assumed to a Gaussian centred as zero because of the existence of finite emission asymmetries. In CorrFit program, one utilizes the full information of the interaction between pairs (Coulomb, Strong and Quantum statistics) and a source model (assumed one) to generate the correlation function.

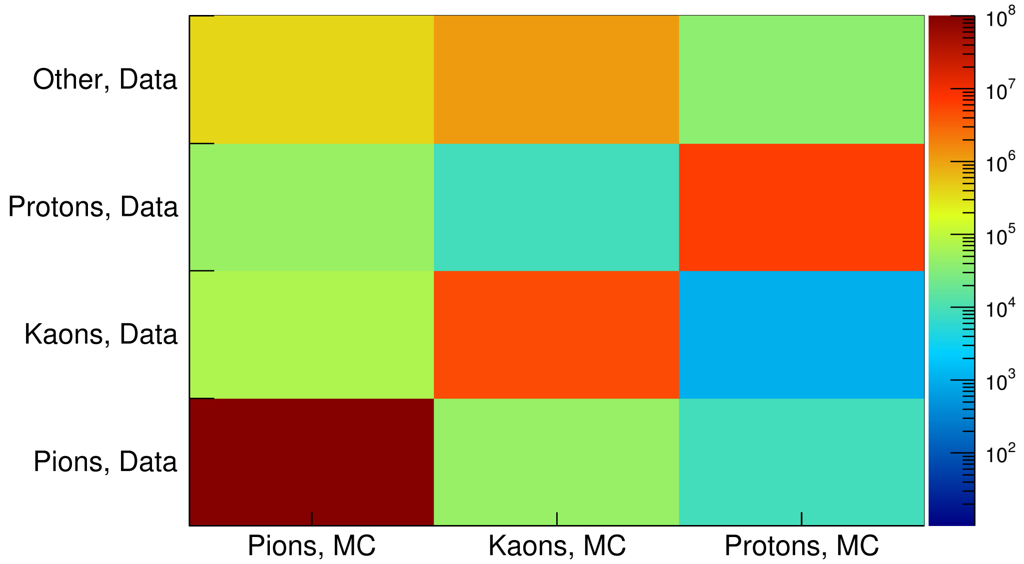

Figure 4.10: Number of particles identified correctly and misidentified as other particles estimated using the HIJING MC generator for 0-5% centrality class [59]

The Koonin-Pratt's equation [62; 63] which relates the experimental correlation function with the source function is given by:

$$C(\mathbf{k}^*) = \int d\mathbf{r}' |\psi(\mathbf{k}^*, \mathbf{r}')|^2 S(\mathbf{r}') \tag{4.13}$$

In equation 4.13, $|\psi(\mathbf{k}^*, \mathbf{r}')|^2$ is the pair wave function and can be calculated for a given pair. This value is treated as weight (W) in CorrFit package. This weight includes quantum statistics for identical particles and FSI's for charged particles. The calculation of W requires the information on relative distance of emission point $\vec{r^*}$ and pair relative momentum $\vec{k^*}$. Therefore, eight independent parameters (three from $\vec{r^*}$), three from $\vec{k^*}$ and two from pair-type) are sufficient to calculate value of W. These W values give information about the two-particle interaction in PRF. However, the main goal is to study about the source emitting these particles. Therefore, the full information of the two particles, their momenta $\vec{p_1}$, $\vec{p_2}$ and their emission points $\vec{r_1^*}$, $\vec{r_2^*}$ which make a total 16 independent values, are required. The ideal way of fitting the correlation function is to first reproduce exactly the two-particle momentum distribution and freeze-out configuration for all pairs which produces the experimental correlation function. This is quite a difficult task to be done using a complicated equation 4.13. Thus, an equivalent Monte-Carlo numerical integration using real momentum distribution from experimental data is performed assuming a specific form of the source function. The experimental correlation functions were parametrized by assuming the source function as a 3-dimensional Gaussian function

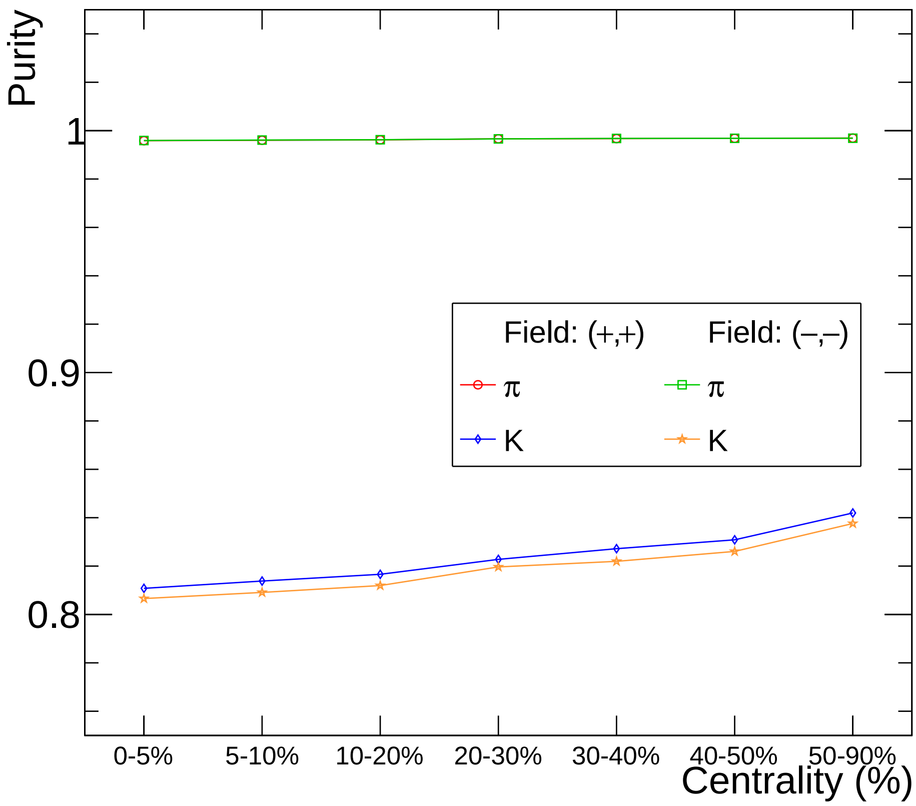

Figure 4.11: The particle purity as a function of centrality for pions and kaons

with three different sizes R_{out}, R_{side} and R_{long} in *out*,*side* and *long* directions respectively with the mean value μ_{out} corresponding to the emission asymmetry:

$$S(\mathbf{r}) = exp\left(-\frac{(r_{out} - \mu_{out})^2}{R_{out}^2} - \frac{r_{side}^2}{R_{side}^2} - \frac{r_{long}^2}{R_{long}^2}\right) \tag{4.14}$$

where r_{out}, r_{side} and r_{long} are the components of relative separation vector $\mathbf{r}$ of the emission points.

This aforementioned procedure is repeated for all necessary pairs to calculate theoretical correlation functions for a given source parametrization. Then the χ^2 test determines how well the theoretical correlation function describes the fexperimental correlation function. The procedure is repeated by giving different input of source parameters to get the best value of theoretical correlation function (minimum value of χ^2) which describes the experimental correlation function.

Corrfit input The momentum and energy distributions of particles were provided for pions and kaons. The p_x, p_y, p_z and E distributions for pions and kaons are shown in Figure 4.13 and 4.14 respectively.

The important inputs given in configuration files are;

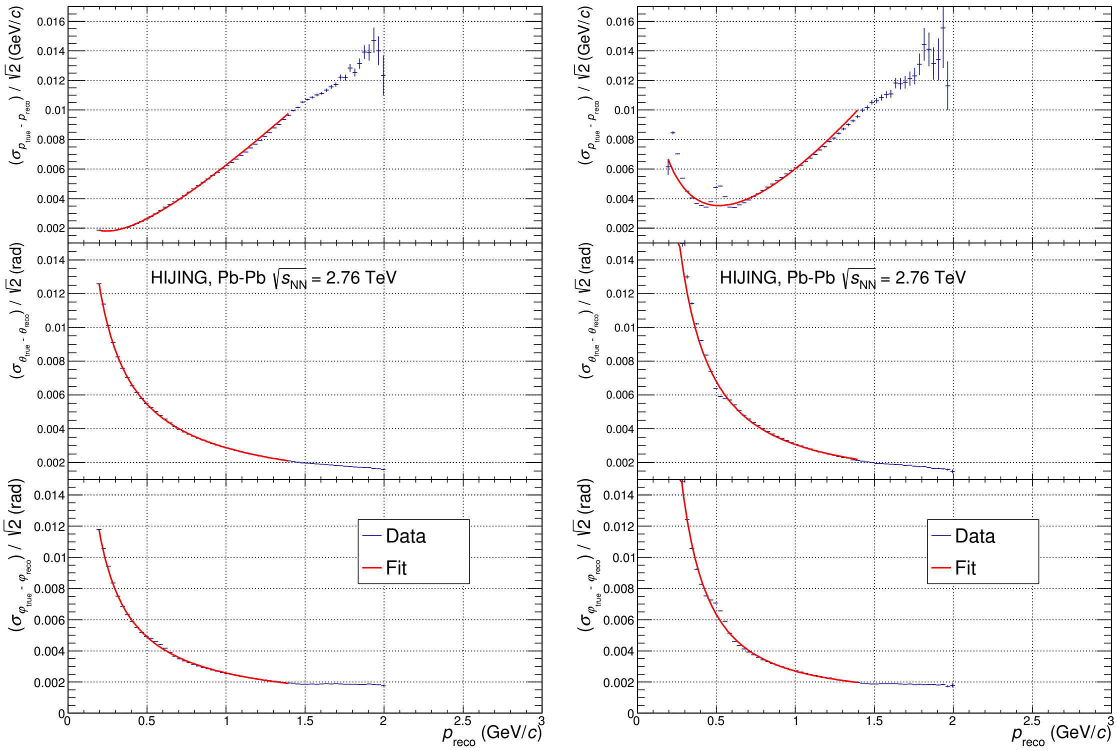

Figure 4.12: The values of standard deviation $\sigma/\sqrt{2}$ of the fitted Gaussian functions to the momentum (top plots), θ (middle plots), and φ (bottom plots) differences between the true and the reconstructed values, together with fits. Results are presented for pions (left plots) and kaons (right plots) [59].

— Correlation fitter: CFFitterNonId which fits 3-dimensional correlation function in *Out-Side-Long* directions,

— Source model: SourceModelGausLCMS which assumes that the source is a 3-dimensional Gaussian profile source like equation 4.14 with parameters average size of source (R_{out}), mean shift in Out direction (μ_{out}) and source sizes in Side and Long directions which are assumed to equal to R_{out} multiplied by a constant factor,

— Fitting range of R_{out} : (3.0,12.0) fm

— Fitting range of μ_{out} : (-8.0,0.0) fm

— R_{side} multiplier: 1.0

— R_{long} multiplier: 1.3

— Interactions: Strong and Coulomb

— The range of the fitting (in k^*) : (0.0,0.1) GeV/c

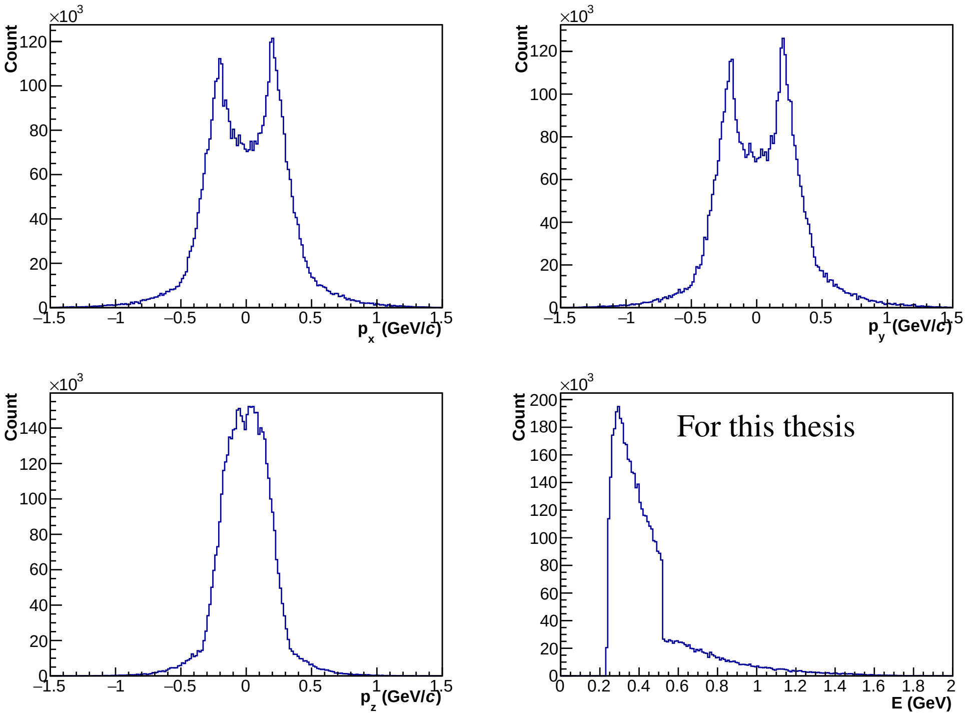

Figure 4.13: Four momentum distribution for pions for Pb−Pb collisions at $\sqrt{s_{\rm NN}}$= 2.76 TeV recorded by ALICE at the LHC.

— Normalization range (in k^*) : (0.15,0.20) GeV/c

R_{side} and R_{long} multipliers are taken to be 1.0 and 1.3. These values are chosen based from identical pion femtoscopy analysis where it was found that R_{side} is equal to R_{out} and R_{long} was almost 1.3 times R_{out} [64]. Another important parameter is the fraction of primary particles which is calculated for each centrality, pair, and magnetic field polarity separately using the following formula:

$$F^s_{\pi^\pm K^\pm}(c) = p^s_\pi(c) \cdot p^s_K(c) \cdot f^s_{\pi^\pm}(c) \cdot f^s_{K^\pm}(c) \cdot g^s(c), \tag{4.15}$$

where F is the fraction of primary, correctly identified pairs of particles that fits under the assumed Gaussian profile, p is the purity of particles, f is the fraction of primary particles, g is the fraction of femtoscopically correlated pairs under assumed Gaussian profile, c is centrality class, and s is the magnetic field polarity. The value of g is estimated using the results obtained in [37] (Table 4.6). The results for F are presented in Figure 4.15.

4.2.1 Systematic Error Estimation

For the estimation of systematic errors, there can be two major considerations. One of the major source can be detector effects (due to various event and track selection cuts,

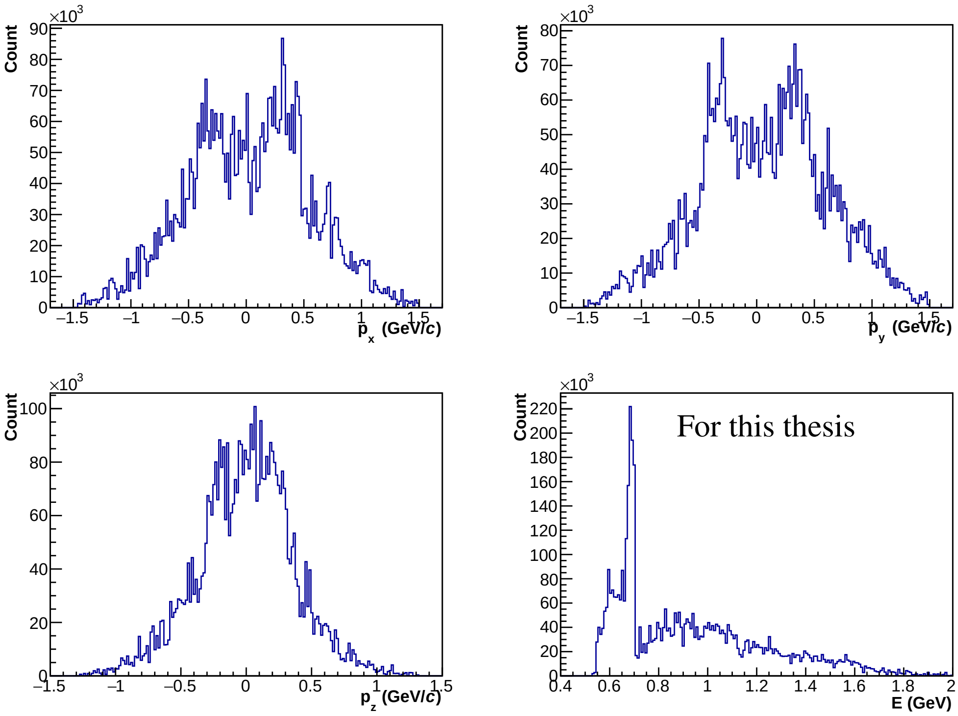

Figure 4.14: Four momentum distribution for kaons for Pb−Pb collisions at $\sqrt{s_{\rm NN}}$= 2.76 TeV recorded by ALICE at the LHC.

pair selections cuts etc) which affects the correlation function. The other refers to the systematic errors due to fitting of the correlation function (variation in purity, fitting range, normalization range etc) to extract the source parameters. Furthermore, the analysis has been performed for both magnetic field polarity and all possible charge combinations of pairs. The systematic uncertainties in correlation function was studied by varying the track quality cuts (using hybrid tracks), the pair selection cuts and the particle identification criteria. Table 4.7 summarizes the contributions from different sources.

The other source of systematic error originates while extracting the source parameters. The different contributions to the total systematic errors on source parameters can be studied by varying the normalization range, fitting range and the value of primary fraction. Table 4.8 shows the contributions from different sources.

Centrality (in %)	**Value of 'g'**
0-5	0.83
5-10	0.82
10-20	0.8
20-30	0.76
30-40	0.73
40-50	0.7

Table 4.6: Value of g for different centrality classes for pion-kaon pairs [37]

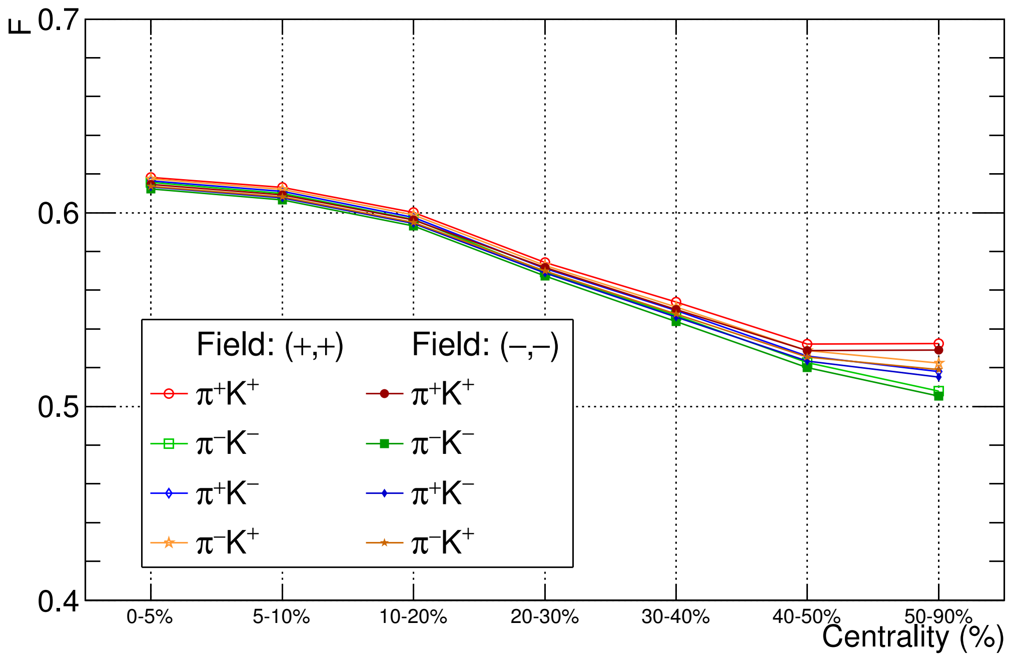

Figure 4.15: The fraction of primary, correctly identified pairs under the assumed Gaussian profile in function of centrality class for all combinations of pion-kaon pairs [59]

Error source	**variation**	**Error (in %) R$_{Out}$, μ_{Out}**
Track	Hybrid track (FilterBit8)	13, 17
Pair cuts	± 2 % MF cut	0.18, 0.5
Strict PID cut	**Pion:** $n\sigma_{TPC}$ < 2.5 for $\|p\|$ < 500 MeV/c, $\sqrt{(n\sigma^2_{TPC} + n\sigma^2_{TOF})}$ < 2.5 for $\|p\|$ > 500 MeV/c **Kaon:** $n\sigma_{TPC}$ < 2.0 for $\|p\|$ < 400 MeV/c, $n\sigma_{TPC}$ < 1.0 for 400 MeV/c < $\|p\|$ < 450 MeV/c, $n\sigma_{TPC}$ < 2.0 and $n\sigma_{TOF}$ < 2.0 for 450 MeV/c < $\|p\|$ < 800 MeV/c, $n\sigma_{TPC}$ < 2.0 and $n\sigma_{TOF}$ < 1.5 for 800 MeV/c < $\|p\|$ < 1000 MeV/c, $n\sigma_{TPC}$ < 2.0 and $n\sigma_{TOF}$ < 1.0 for $\|p\|$ > 1000 MeV/c	Combined error from strict and loose PID: 6, 15
Looser PID cut	**Pion:** $n\sigma_{TPC}$ < 3.0 for $\|p\|$ < 500 MeV/c, $\sqrt{(n\sigma^2_{TPC} + n\sigma^2_{TOF})}$ < 3.0 for $\|p\|$ > 500 MeV/c **Kaon:** $n\sigma_{TPC}$ < 2.5 for $\|p\|$ < 400 MeV/c, $n\sigma_{TPC}$ < 2.0 for 400 MeV/c < $\|p\|$ < 450 MeV/c, $n\sigma_{TPC}$ < 3.0 and $n\sigma_{TOF}$ < 2.5 for 450 MeV/c < $\|p\|$ < 500 MeV/c, $n\sigma_{TPC}$ < 3.0 and $n\sigma_{TOF}$ < 3.0 for 500 MeV/c < $\|p\|$ < 800 MeV/c, $n\sigma_{TPC}$ < 3.0 and $n\sigma_{TOF}$ < 2.5 for 800 MeV/c < $\|p\|$ < 1000 MeV/c, $n\sigma_{TPC}$ < 3.0 and $n\sigma_{TOF}$ < 2.0 for $\|p\|$ > 1000 MeV/c	

Table 4.7: Systematic studies from different experimental sources and their contributions

Error source	**variation**	**Error (in %) $\mathbf{R}_{Out}$, μ_{Out}**
Normalization range	k^* : (0.1,0.12), (0.12,0.17), (0.18,0.25) GeV/c	0.6, 0.9
Fit range	k^* = (0.,0.08),(0.,0.12),(0.,0.15), (0.005, 0.1), (0.01,0.1) GeV/c	9, 19
Primary fraction (purity)	± 10%	10, 16

Table 4.8: Systematic studies from different experimental sources and their contributions

Chapter 5

Experimental Observations

Abstract: This chapter describes the experimental results of the pion-kaon femtoscopy analysis in Pb−Pb collisions at $\sqrt{s_{\rm NN}}$= 2.76 TeV as recorded by ALICE experiment. The correlation functions and the double ratios obtained by the methods described in Chapter 4 are presented. The obtained correlation function is fitted using the CorrFit software to obtain the pion-kaon system size and the emission asymmetry. The results are compared with the results obtained by Spherical Harmonics technique. The final results are then compared with the expectations from Therminator2 model coupled with (3+1)D viscous hydrodynamics.

5.1 Experimental Correlation function

The experimental correlation function is given by the following equation:

$$C(\mathbf{k}^*) = \frac{\int N(\mathbf{p}_a, \mathbf{p}_b)\delta(\mathbf{k}^* - \frac{1}{2}(\mathbf{p}^*_a - \mathbf{p}^*_b))d^3p_a d^3p_b}{\int D(\mathbf{p}_a, \mathbf{p}_b)\delta(\mathbf{k}^* - \frac{1}{2}(\mathbf{p}^*_a - \mathbf{p}^*_b))d^3p_a d^3p_b} = \frac{N(\mathbf{k}^*)}{D(\mathbf{k}^*)} \tag{5.1}$$

where $N(\mathbf{k}^*)$ is the distribution of pairs coming from same events while $D(\mathbf{k}^*)$ is the distribution of pairs when the particles are taken from two different events and hence do not have any dynamical correlation. The variable k^* in equation 5.1 represents half of the relative momentum of the pair in PRF.

The experimental pion-kaon correlation function for Pb−Pb collisions at $\sqrt{s_{\rm NN}}$= 2.76 TeV measured for all charge combinations in *Out*, *Long*, and *Side* direction is studied for all considered centrality classes. This study is also presented for both positive and negative polarity of the applied magnetic field. Figures 5.1, 5.2, 5.3, 5.4, 5.5 and 5.6 show the correlation function as a function of k^* for 0-5%, 5-10%, 10-20%, 20-30%, 30-40% and 40-50% centrality classes. As can be seen in all the figures, the values of the pion-kaon correlation function is above unity for pairs of opposite charge combinations and below unity for same charge combinations. This observation is expected due to the Coulomb interaction between pions and kaons. The unlike-sign pairs show attractive interaction (above unity) while the like-sign pairs have repulsive interaction (below unity). The correlation function has similar behavior in all the three directions (*Out*, *Side* and *Long*) and there is no significant difference due to difference in polarities of magnetic field. The strength of correlation function is observed to increase from central to peripheral collisions.

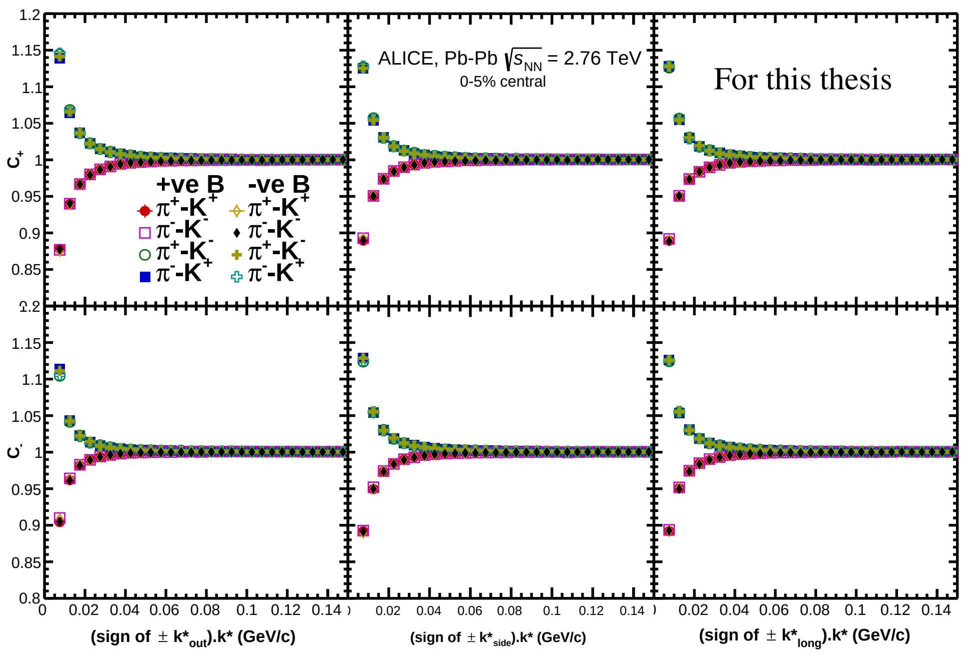

Figure 5.1: Pion-kaon correlation functions with pair cuts in *Out-Side-Long* directions for 0-5% centrality bin for Pb−Pb collisions at $\sqrt{s_{NN}}$= 2.76 TeV recorded by ALICE at the LHC

5.2 Double ratio and Emission Asymmetry

The qualitative features of pion-kaon emission asymmetry (as discussed in chapter 2) can be explored by using the Double ratios. Figure 5.7 shows the measured pion-kaon double ratios for all charge combinations in all the three directions for 0-5% centrality class. The emission asymmetry is expected to be observed in *Out* direction. The double ratio in *Out* direction is above unity for unlike-sign pairs while it is below unity for like-sign combinations of pions and kaons. This indicates that pions are emitted much closer

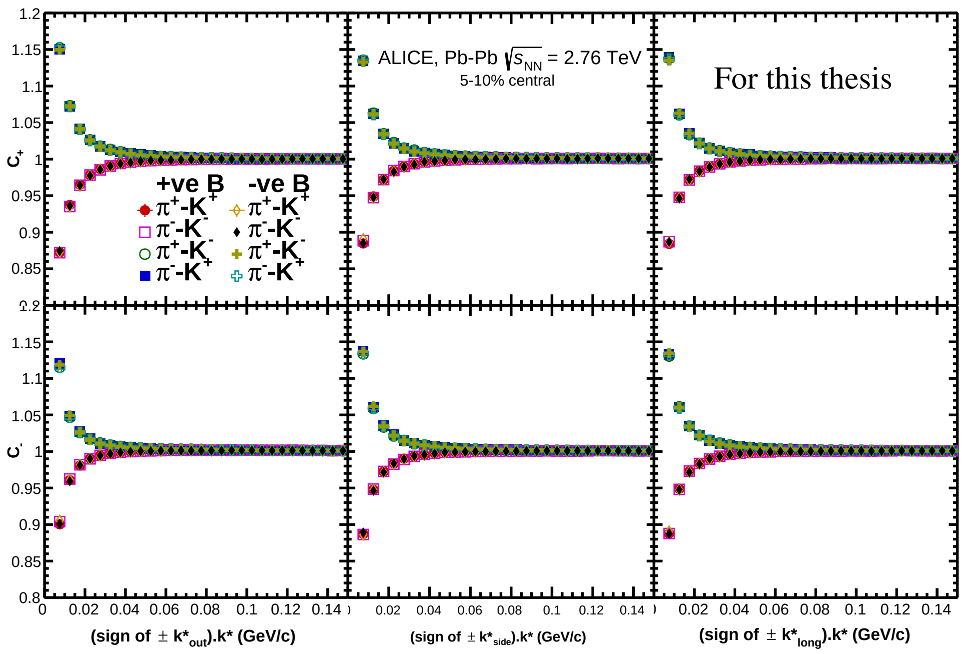

Figure 5.2: Pion-kaon correlation functions with pair cuts in *Out*-*Side*-*Long* directions for 5-10% centrality bin for Pb−Pb collisions at $\sqrt{s_{\rm NN}}$= 2.76 TeV recorded by ALICE at the LHC

to the centre of the fireball produced in heavy ion collision than kaons. In other words, pions seem to be emitted later than kaons.

The double ratio in *Side* direction is expected to be unity due to symmetry considerations. Similarly, the double ratio in the *Long* direction should be uniform at unity for collisions of symmetric system (here, Pb−Pb). It can be seen that the double ratios are almost flat at unity for both *Side* and *Long* direction but it is slightly deviated from unity in small k^* region due to the limited detector resolution effects. In general, the differences between the correlation functions with different set of pair cuts are really small. It is difficult to select the pair cuts by simply observing the correlation figures alone. However, it is important to remove the unwanted detector effects to reduce the spurious correlations. The detector effects can be visualised by exploring the double ratios in *Side* and *Long* directions where the ratio is expected to be unity. Any deviation from this value indicates towards the presence of detector effects. Various set of pair cuts (combination of different Merged fraction cut and $\overline{\gamma}$ cut) were used to obtain the double ratios in *Side* direction and a χ^2_{ndf} test was performed to select the best combination. According to this procedure, it was found out that the set of two track cut when MF is 1% with $\overline{\gamma}$ cut has the lowest value of χ^2_{ndf} for $k^* \leq 0.2$ GeV/c for unlike-sign pairs while for like-sign pairs, a MF cut of 7%

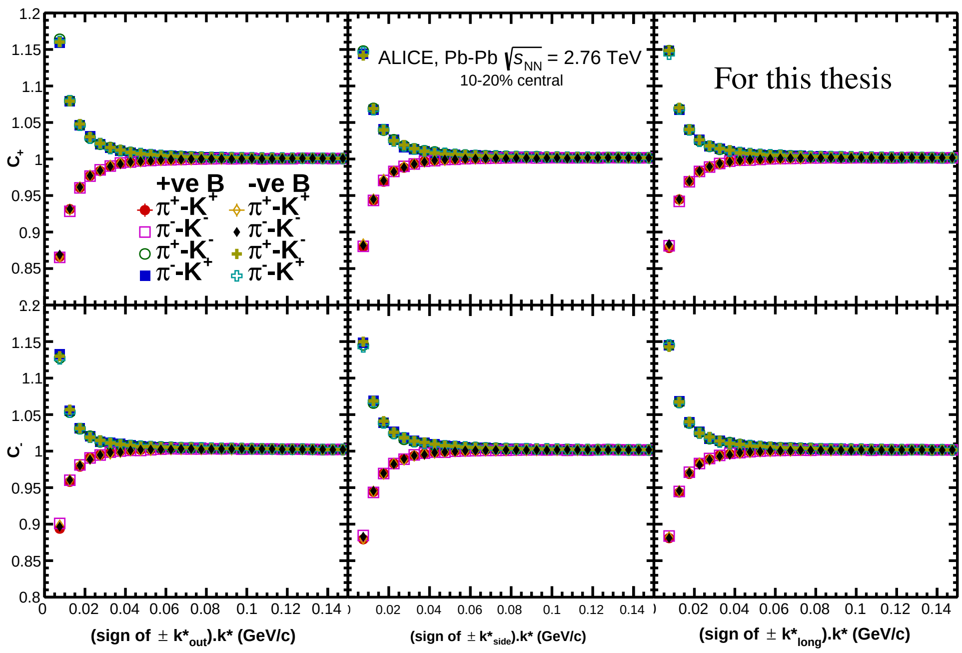

Figure 5.3: Pion-kaon correlation functions with pair cuts in *Out*-*Side*-*Long* directions for 10-20% centrality bin for Pb−Pb collisions at $\sqrt{s_{NN}}$= 2.76 TeV recorded by ALICE at the LHC

was found suitable. The detector effects can be visualised by comparing the double ratios in *Side* and *Long* direction before and after the application of various pair selection cuts. The variation of double ratios with k^* for like-sign pairs in *Side* and *Long* directions is shown in Figure 5.8 and 5.10 respectively for most central events. A similar figure for unlike-sign pairs in *Side* and *Long* is shown in Figure 5.9 and 5.11 respectively. These figures compare the values of double ratio before and after applying the pair cuts. It is clearly visible that the double ratio is deviated from unity when the pair cuts were not applied (first upper panel) or without (or with) the application of anti-γ cut only. However, with the application of merged fraction cut, the double ratios are much closer to unity in both *Side* and *Long* direction.

Figures 5.12, 5.13, 5.14, 5.15, 5.16 and 5.17 show the double ratios (after applying the pair cuts) for all charge combinations as a function of k^* for different centrality classes in *Out*, *Side* and *Long* direction for different polarities of magnetic field.

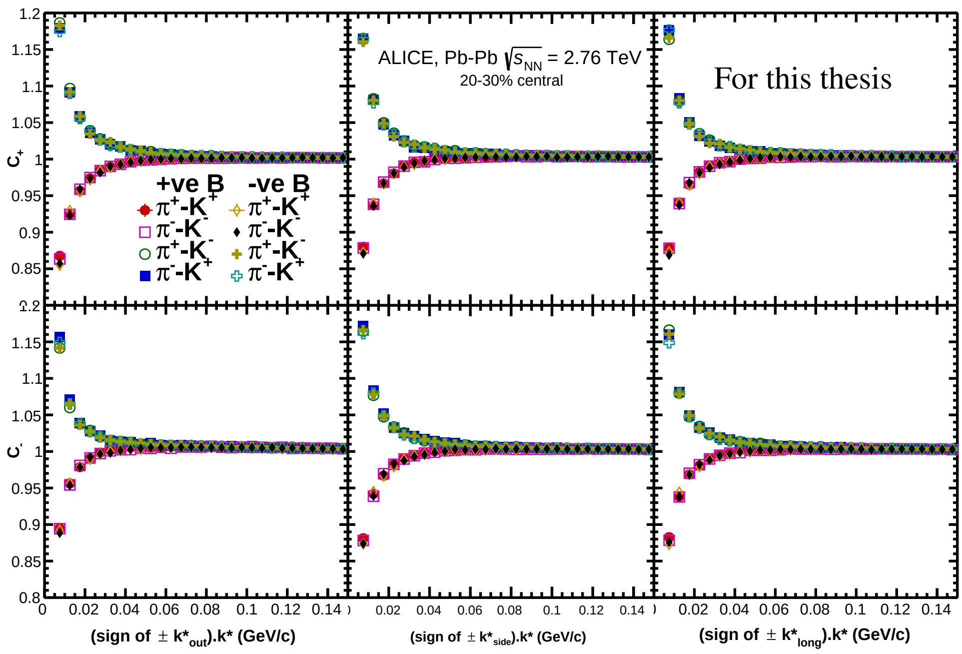

Figure 5.4: Pion-kaon correlation functions with pair cuts in *Out-Side-Long* directions for 20-30% centrality bin for Pb−Pb collisions at $\sqrt{s_{NN}}$= 2.76 TeV recorded by ALICE at the LHC

5.3 Non-femtoscopic background correction

Figures 5.18, 5.19, 5.20, 5.21, 5.22 and 5.23 show the correlation function as a function of $k*$ in *Out* direction for different centrality bins after applying the above mentioned pair cuts. It can be seen that correlation functions are not flat around unity but slightly above unity for higher values of k^* where the femtoscopic correlations are not present. The reason for this is the presence of background originating from non-femtoscopic correlations in experimental correlation function as discussed in 4.1.8. It can also be seen that this background increases from central to peripheral events where presumably the contribution from elliptic flow dominates. It is necessary to remove this non-femtoscopic background to extract the relevant femtoscopic parameters. A sixth order polynomial was used to describe the nature of the background for all centrality classes. The background subtraction method as described in Chapter 4 is implemented to obtain the corrected correlation function. The correlation functions are also fitted with 6th order polynomial which explains the background nicely. Figures 5.24, 5.25, 5.26, 5.27, 5.28 and 5.29 show the background subtracted correlation function as a function of k^* in *Out* direction for different centrality classes. It can be observed that correlation functions are now flat around unity.

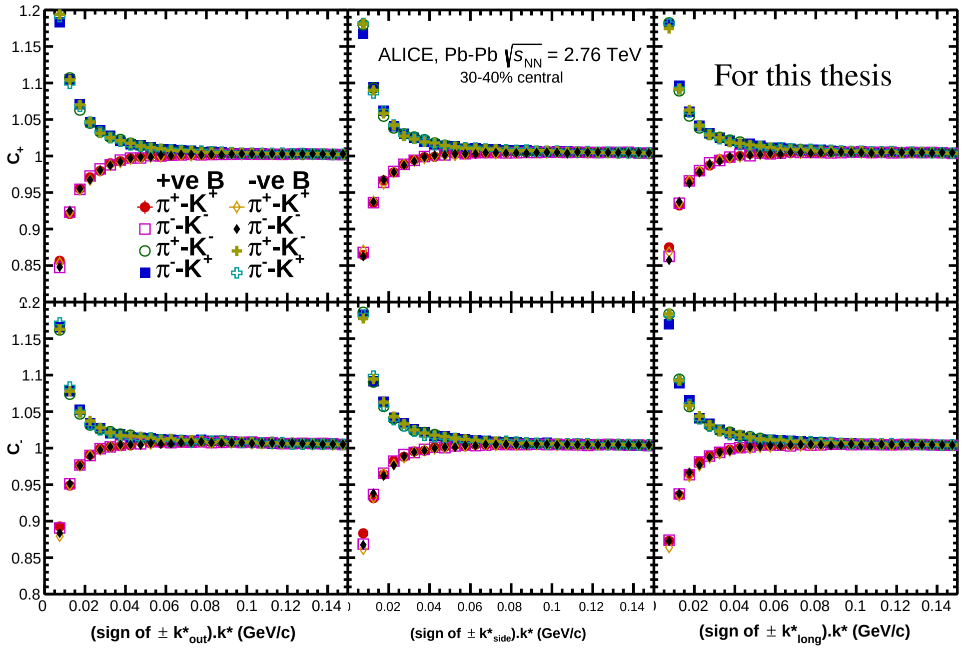

Figure 5.5: Pion-kaon correlation functions with pair cuts in *Out-Side-Long* directions for 30-40% centrality bin for Pb−Pb collisions at $\sqrt{s_{\rm NN}}$= 2.76 TeV recorded by ALICE at the LHC

5.4 Extraction of source parameters

The observation of double ratio which deviates from unity in *Out* direction indicated towards the existence of emission asymmetry in pion-kaon system. The numerical estimation of this emission asymmetry as well as the size of the pion-kaon homogeneity region can be performed by fitting the correlation function using the CorrFit [61] fitting procedure (described in Chapter 4). Figures 5.30, 5.31, 5.32 and 5.33 show the fitted correlation functions (after background subtraction) for different combination of pairs of particles for different centrality bins.

It can be observed that the fits nicely describe the overall shape of the correlation function and therefore one can assume that the parameters of the fit can be used to describe the source parameters of the data. Figure 5.34 shows the average source size of the pion-kaon homogeneity region and the emission asymmetry as a function of centrality for all charge combinations for both positive and negative polarity of magnetic fields. The average value of radii and the emission asymmetry between pion-kaon pairs decreases from most central events to peripheral events. The results of radii values are consistent for all combinations of pairs and both magnetic field polarities. There are some small deviations in some pair combinations for a given centrality class. However, the overall dependence

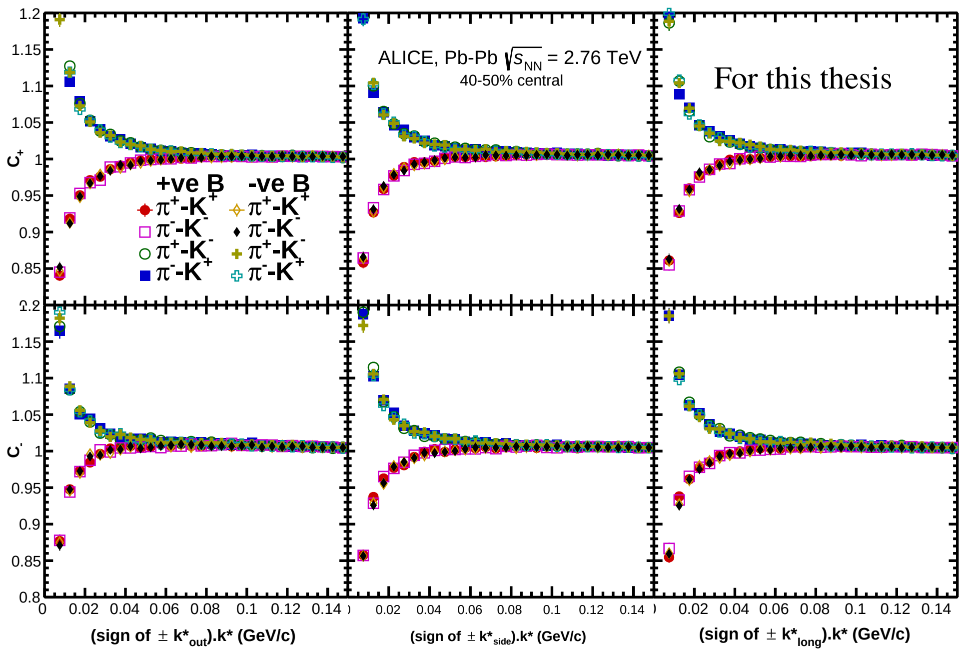

Figure 5.6: Pion-kaon correlation functions with pair cuts in *Out-Side-Long* directions for 40-50% centrality bin for Pb−Pb collisions at $\sqrt{s_{NN}}$= 2.76 TeV recorded by ALICE at the LHC

on centrality is preserved for all considered pairs and field polarity combinations. The trend for emission asymmetry is also consistent. The spread between the results for different pair combinations is higher than for radii results, but the overall tendency of an increase in asymmetry with centrality is clearly visible. Therefore, the final values of the source parameters were taken to be the average of values obtained for all pair combinations and polarity of magnetic field for a given centrality class. This is shown in Figure 5.35.

Figure 5.36 compares the source parameters obtained from the cartesian coordinate method with that of the spherical harmonics approach. The depicted ratio is around unity within uncertainties which indicates a good agreement between the two approaches. The radii values from two methods vary within 10% while they vary within 10% for μ.

One can observe the larger errors for μ in Cartesian coordinate approach. The reason lies in dividing the pairs into two groups to obtain C^+ and C^-. The statistical significance of the two groups may not be equal. The statistical error for obtaining average size is dominated by the statistics from the component which has higher statistics (best case scenario) while the opposite situation prevails in extracting emission asymmetry, μ. In

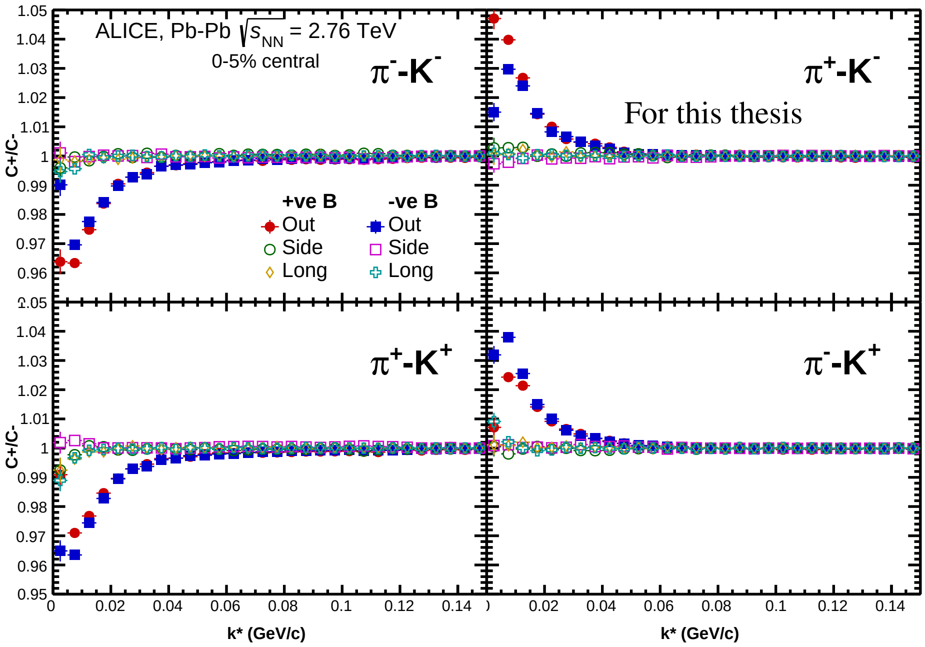

Figure 5.7: Pion-kaon double ratio without any pair cuts in *Out-Side-Long* directions for 0-5% centrality bin for Pb−Pb collisions at $\sqrt{s_{NN}}$= 2.76 TeV recorded by ALICE at the LHC

the later case, the statistical error is dominated by the statistics from the component with lower statistics (worst case scenario).

Figure 5.37 compares the experimental results with the estimations of Therminator2 (an event generator based on statistical hadronization) coupled with (3+1)D viscous hydrodynamic model [65]. There are different estimations due to introduction of additional time delays for case of kaons. The extracted source radius in *Out* direction agrees with the estimations and show no significant dependence on various values of kaon delay time. However, one can observe that the values of emission asymmetry are affected by the kaon delay time. The experimental data shows a good agreement with the Therminator2 calculations when an additional time delay of 2.1 fm/c was introduced for kaons. The experimental observations in this analysis are consistent with the hydrodynamic-induced evolution of the system created in heavy ion collisions and favors a strong radial flow in central collisions. The origin of asymmetry can be understood by the strong radial flow hypothesis and the interplay between the collective and thermal movement of the dense matter created in collisions of heavy ions.

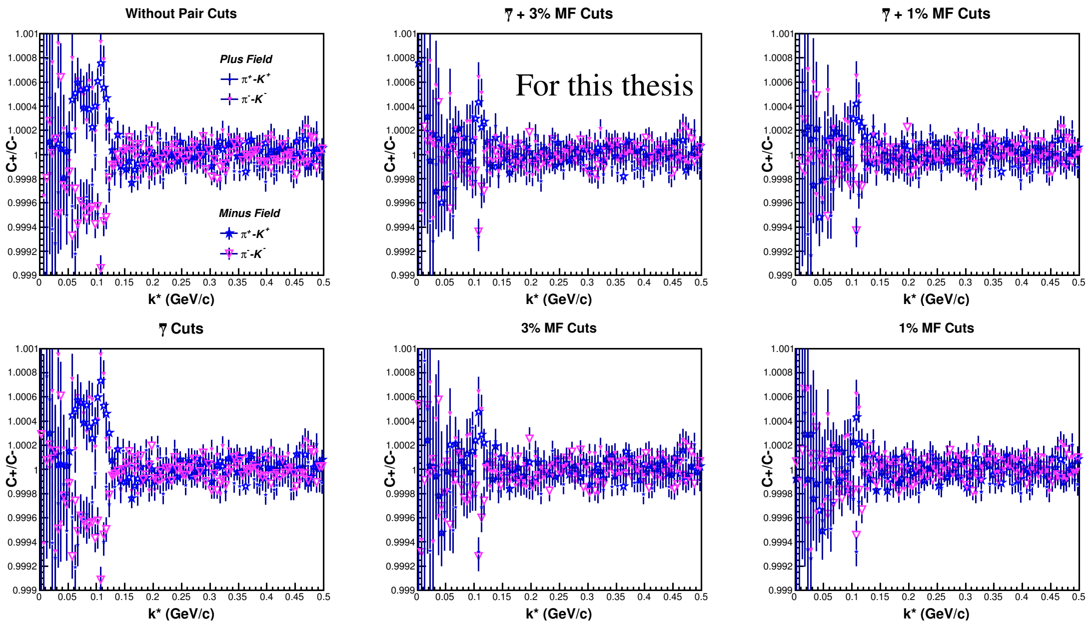

Figure 5.8: The variation of Double ratio with k^* in $Side$ direction for like-sign pairs (0-5% central)

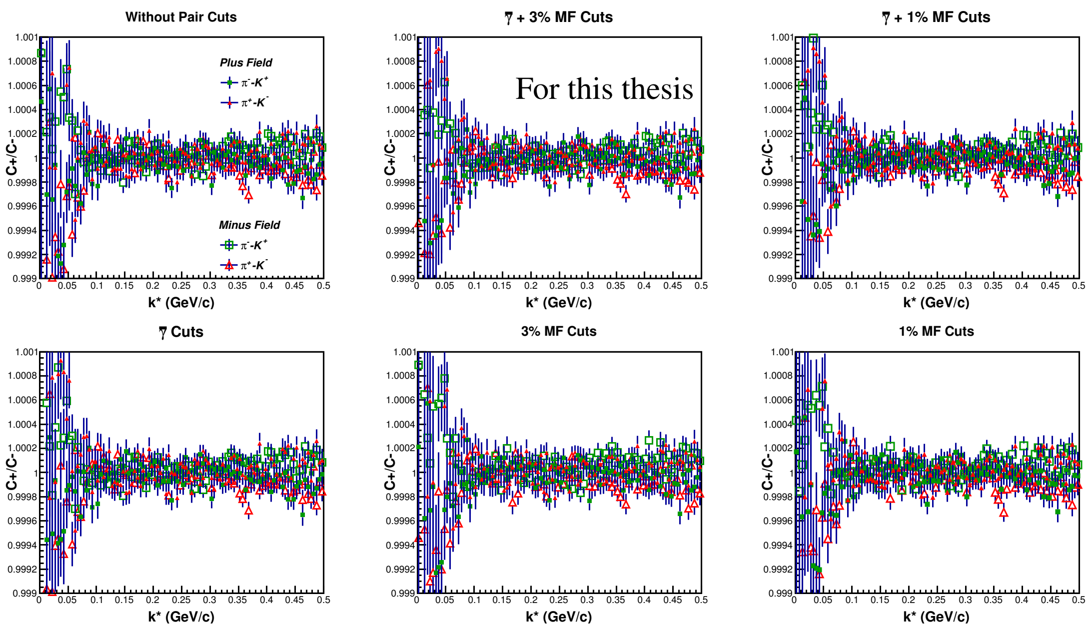

Figure 5.9: The variation of Double ratio in $Side$ direction for unlike-sign pairs (0-5% central)

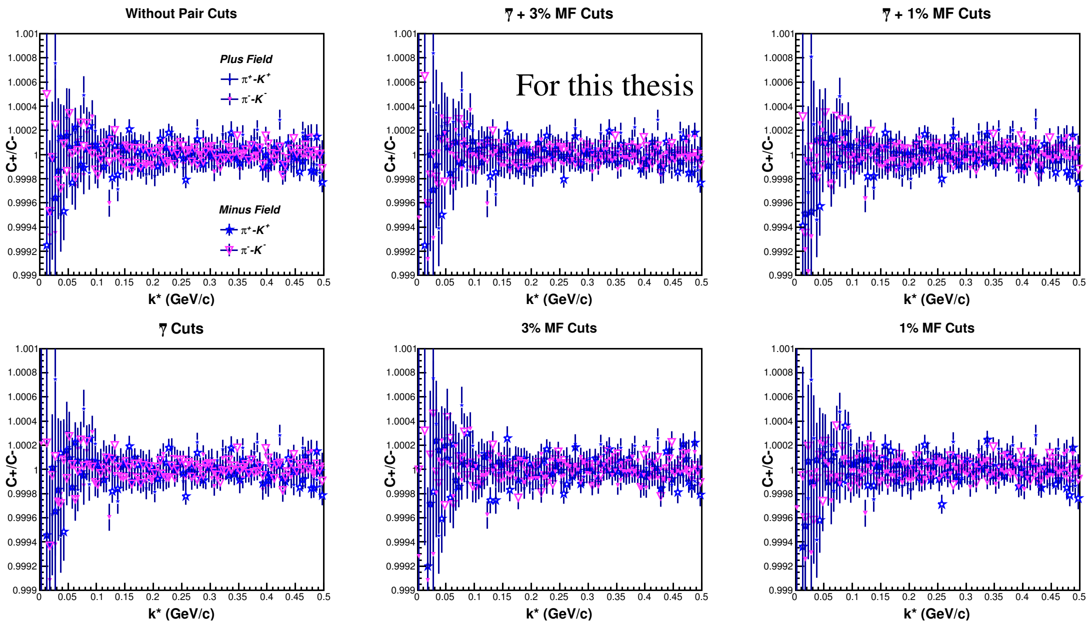

Figure 5.10: The variation of Double ratio in *Long* direction for like-sign pairs (0-5% central)

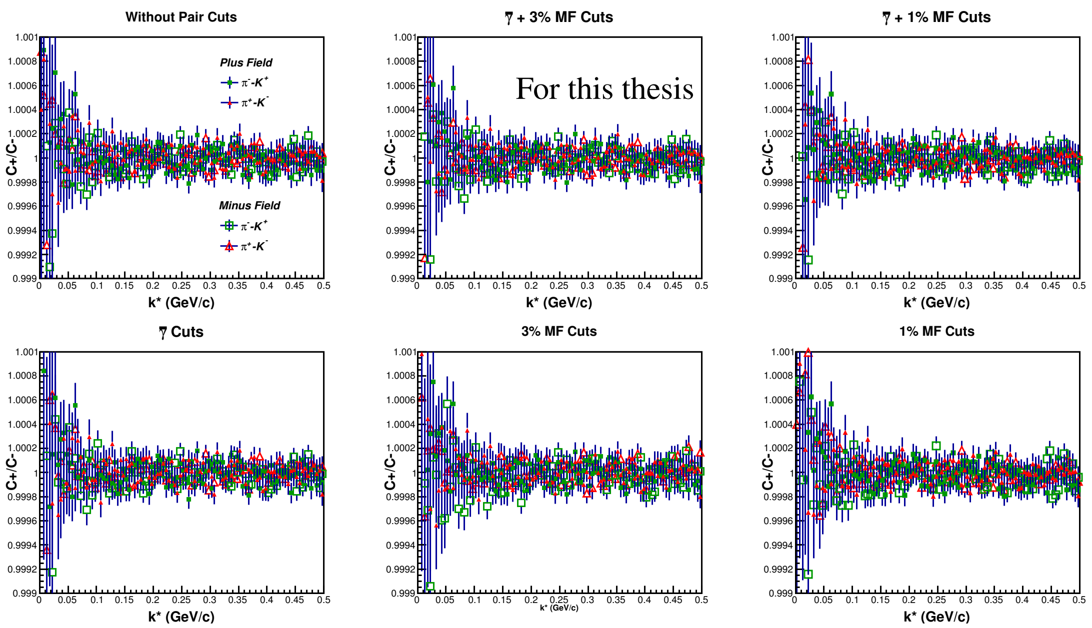

Figure 5.11: The variation of Double ratio in Long direction for unlike-sign pairs (0-5% central)

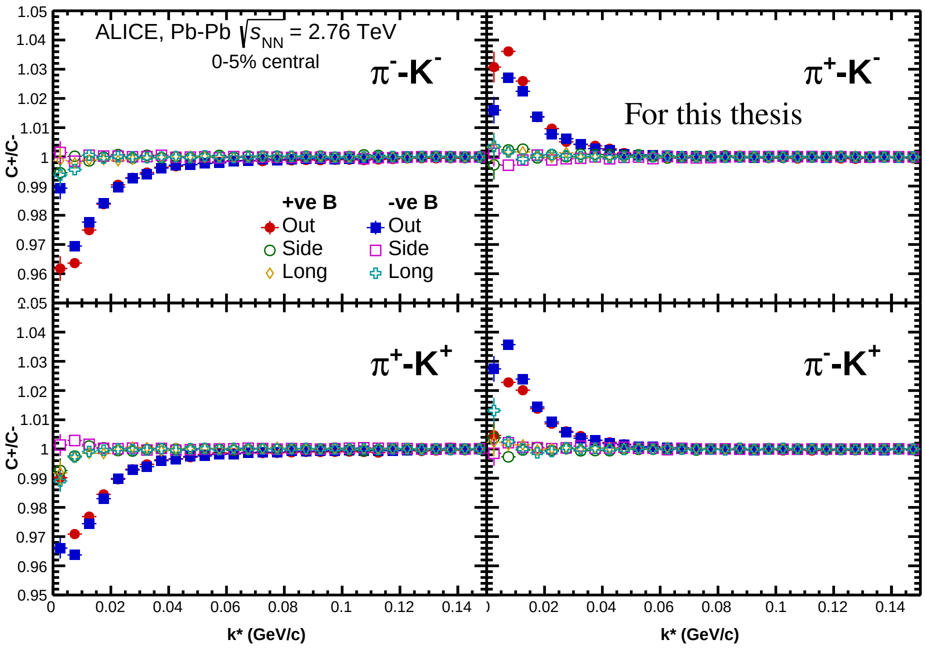

Figure 5.12: The pion-kaon double ratio as a function of $k*$ in *Out-Side-Long* directions for 0-5% centrality bin for Pb−Pb collisions at $\sqrt{s_{NN}}$= 2.76 TeV recorded by ALICE at the LHC

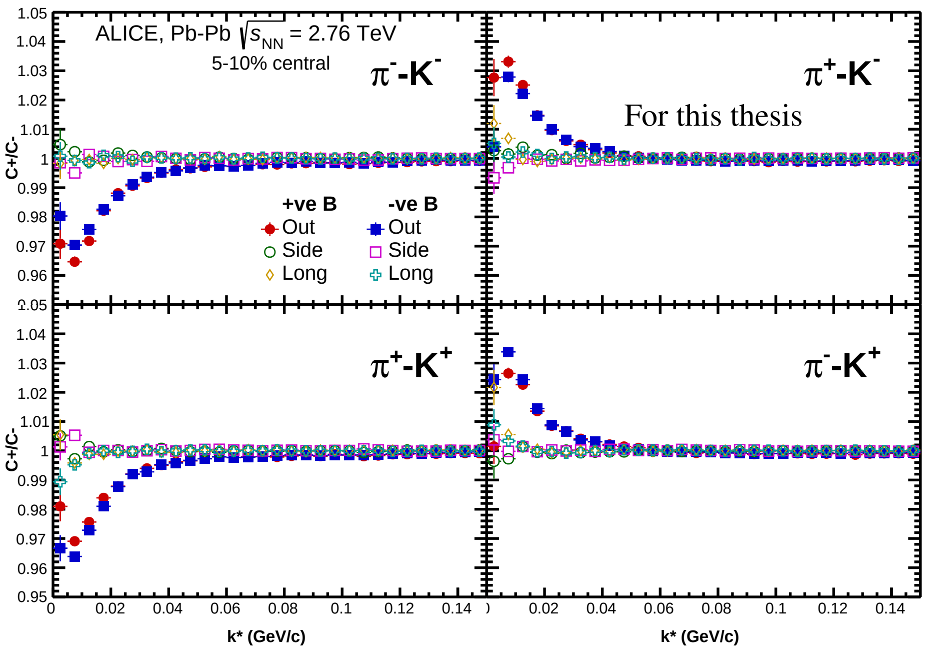

Figure 5.13: The pion-kaon double ratio as a function of $k*$ in *Out-Side-Long* directions for 5-10% centrality bin for Pb−Pb collisions at $\sqrt{s_{NN}}$= 2.76 TeV recorded by ALICE at the LHC.

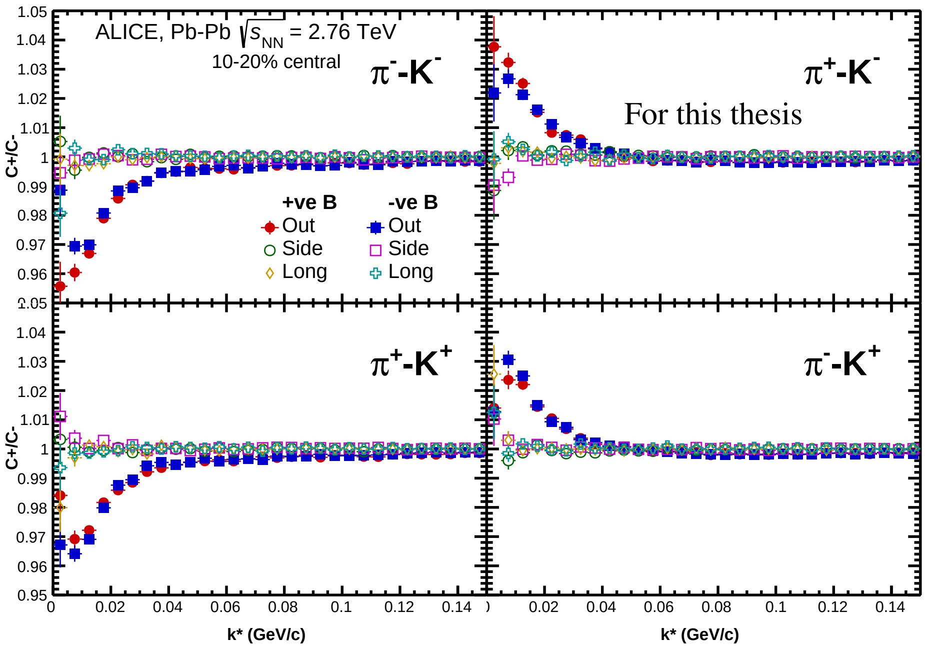

Figure 5.14: The pion-kaon double ratio as a function of $k*$ in *Out-Side-Long* directions for 10-20% centrality bin for Pb−Pb collisions at $\sqrt{s_{NN}}$= 2.76 TeV recorded by ALICE at the LHC.

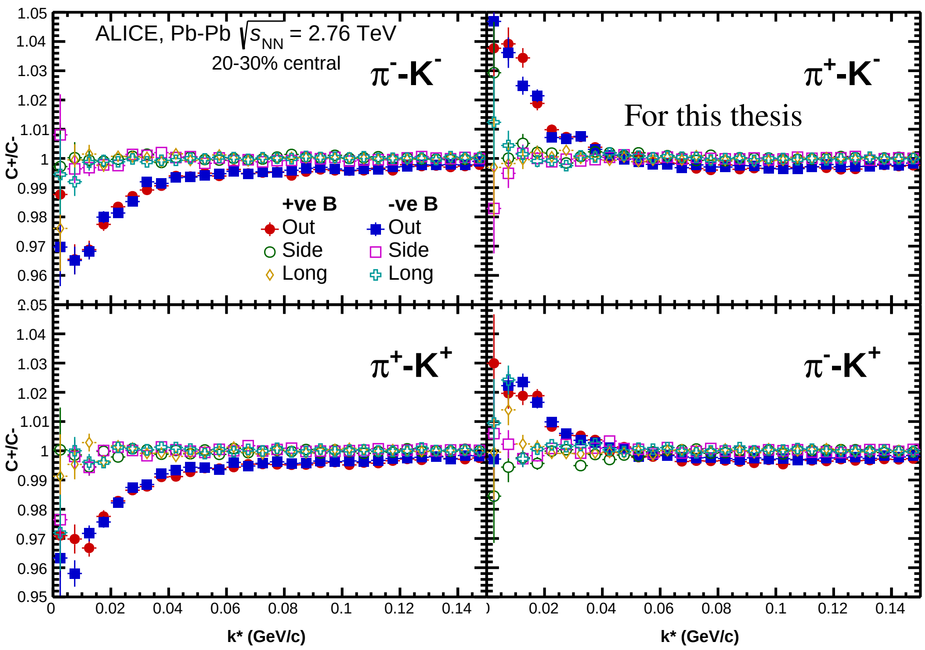

Figure 5.15: The pion-kaon double ratio as a function of $k*$ in *Out-Side-Long* directions for 20-30% centrality bin for Pb−Pb collisions at $\sqrt{s_{NN}}$= 2.76 TeV recorded by ALICE at the LHC.

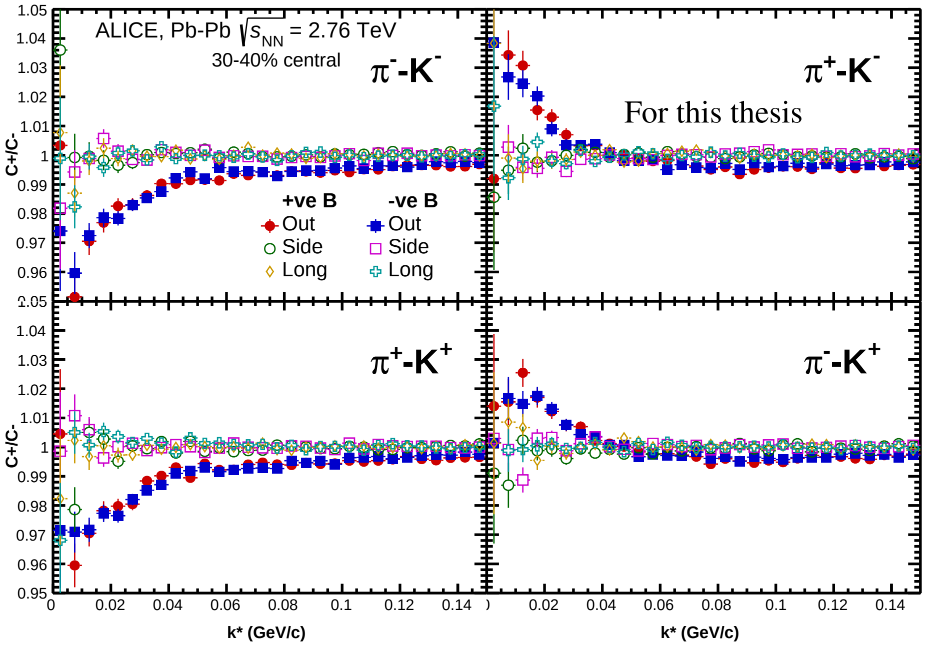

Figure 5.16: The pion-kaon double ratio as a function of $k*$ in *Out-Side-Long* directions for 30-40% centrality bin for Pb−Pb collisions at $\sqrt{s_{\rm NN}}$= 2.76 TeV recorded by ALICE at the LHC.

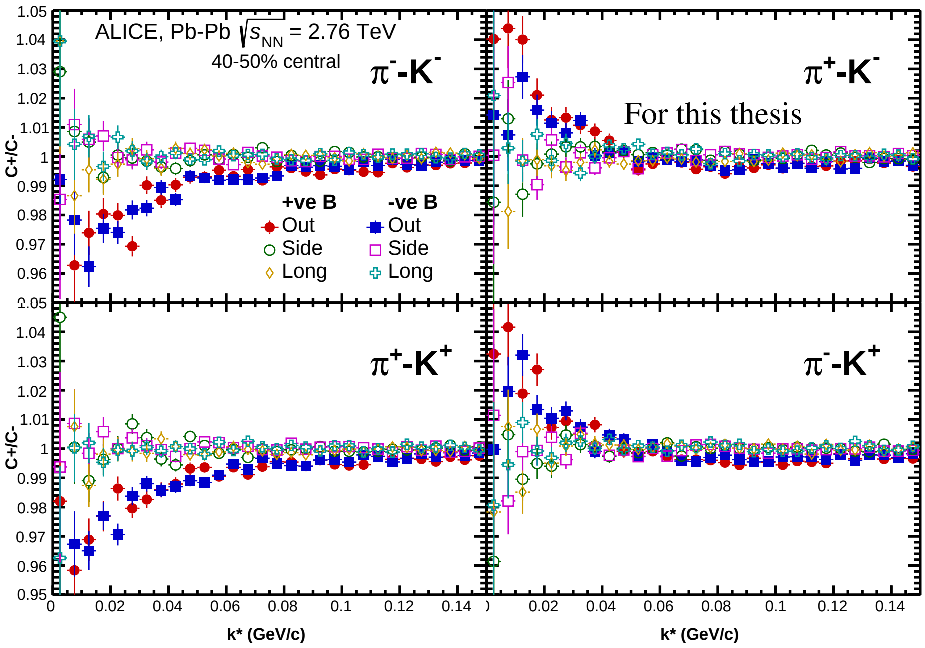

Figure 5.17: The pion-kaon double ratio as a function of $k*$ in *Out-Side-Long* directions for 40-50% centrality bin for Pb−Pb collisions at $\sqrt{s_{\rm NN}}$= 2.76 TeV recorded by ALICE at the LHC.

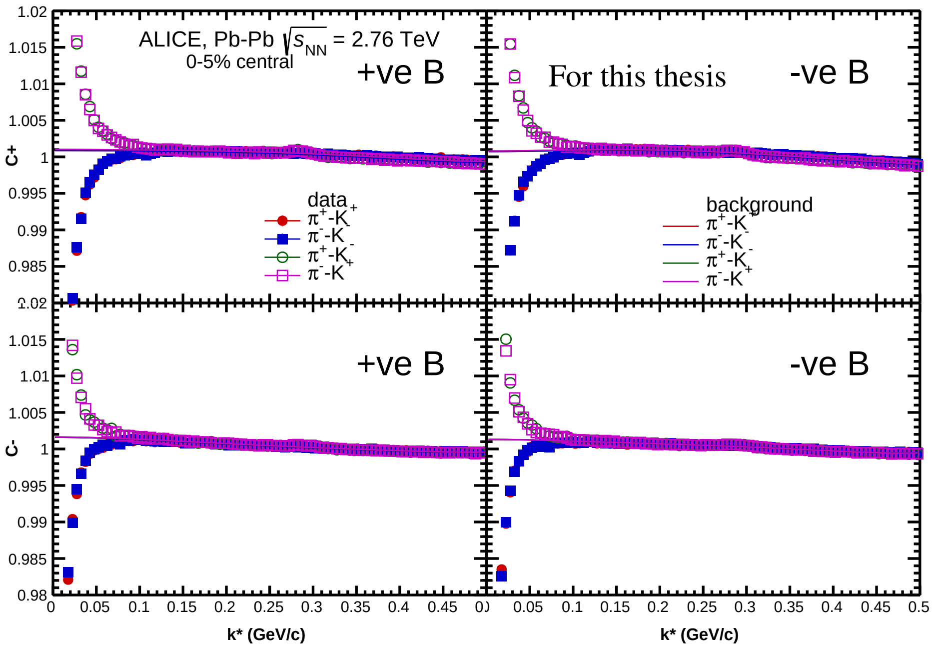

Figure 5.18: The pion-kaon correlation functions with pair cuts in *Out* directions for 0-5% centrality bin for Pb−Pb collisions at $\sqrt{s_{\mathrm{NN}}}$= 2.76 TeV recorded by ALICE at the LHC. The background curve is a 6th order polynomial function.

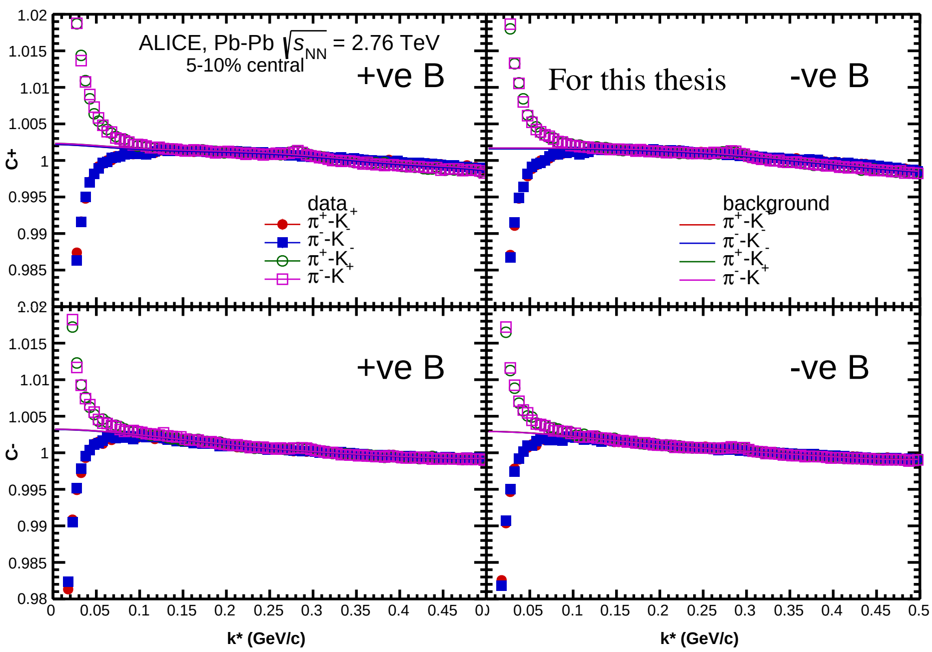

Figure 5.19: The pion-kaon correlation functions with pair cuts in *Out* directions for 5-10% centrality bin for Pb−Pb collisions at $\sqrt{s_{\mathrm{NN}}}$= 2.76 TeV recorded by ALICE at the LHC. The background curve is a 6th order polynomial function.

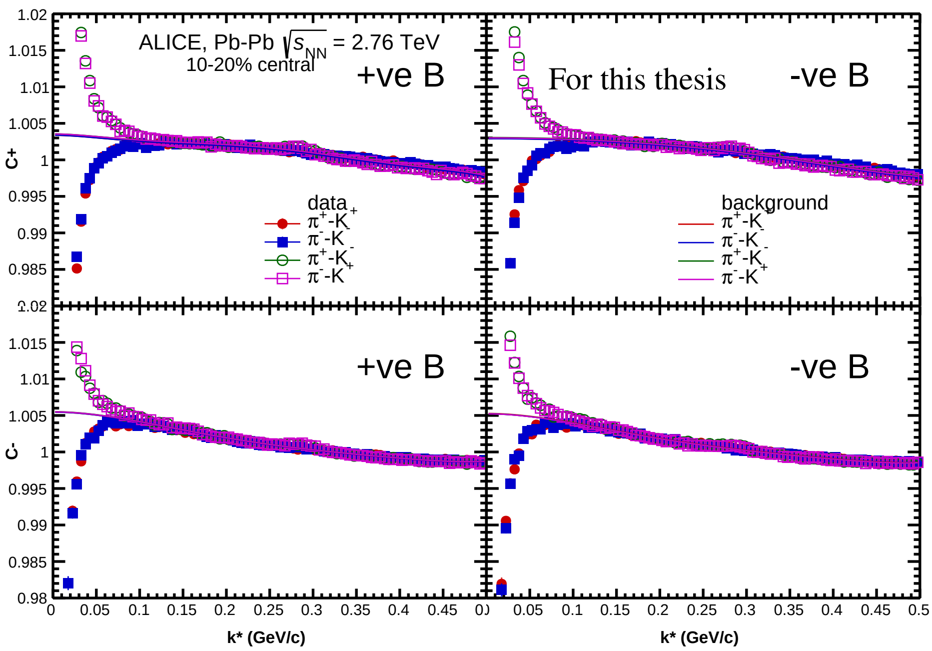

Figure 5.20: The pion-kaon correlation functions with pair cuts in *Out* directions for 10-20% centrality bin for Pb−Pb collisions at $\sqrt{s_{\rm NN}}$= 2.76 TeV recorded by ALICE at the LHC. The background curve is a 6th order polynomial function.

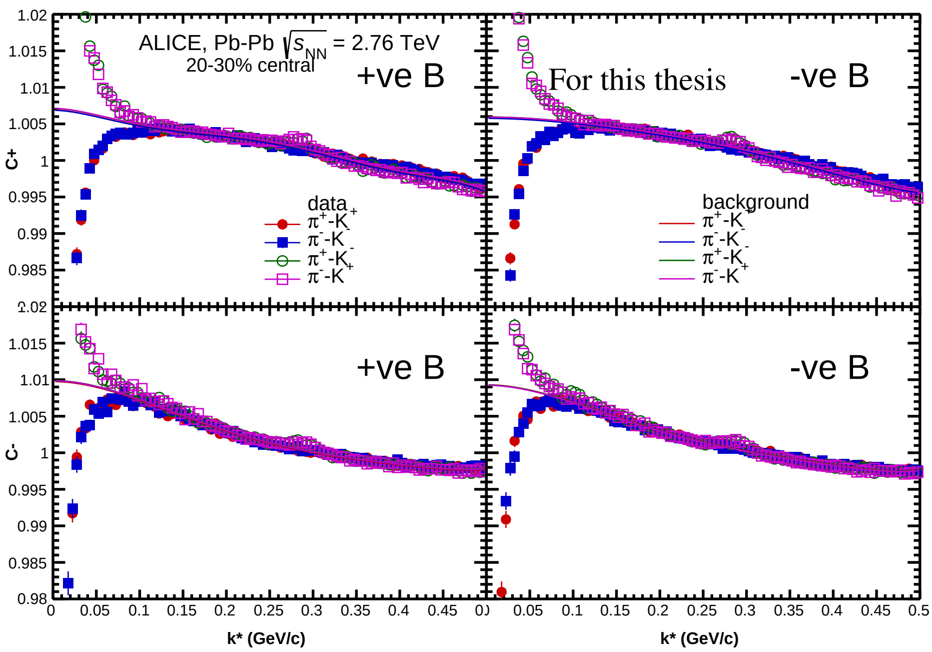

Figure 5.21: The pion-kaon correlation functions with pair cuts in *Out* directions for 20-30% centrality bin for Pb−Pb collisions at $\sqrt{s_{\rm NN}}$= 2.76 TeV recorded by ALICE at the LHC. The background curve is a 6th order polynomial function

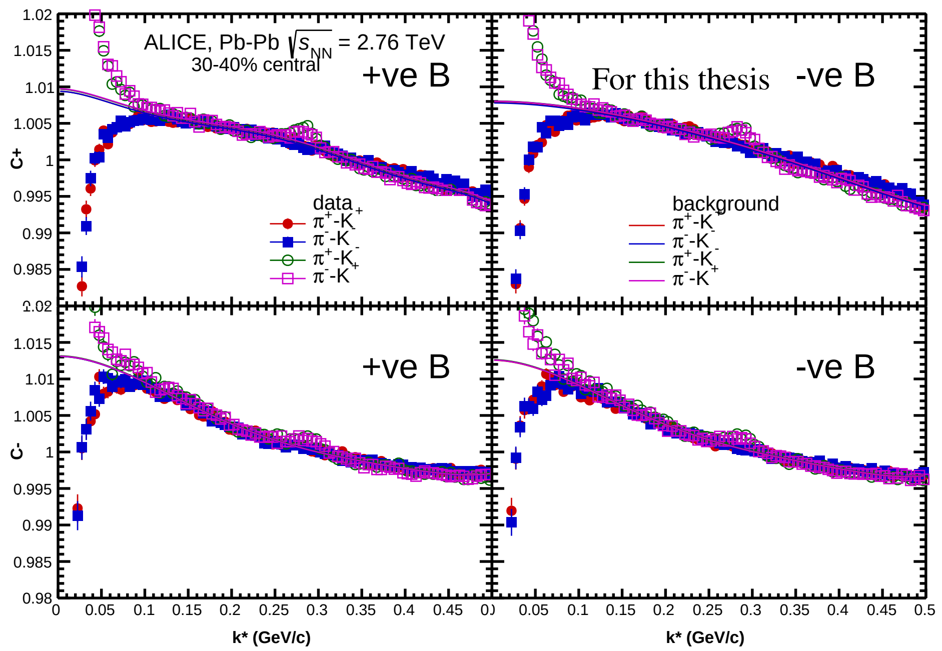

Figure 5.22: The pion-kaon correlation functions with pair cuts in *Out* directions for 30-40% centrality bin for Pb−Pb collisions at $\sqrt{s_{\rm NN}}$= 2.76 TeV recorded by ALICE at the LHC. The background curve is a 6th order polynomial function.

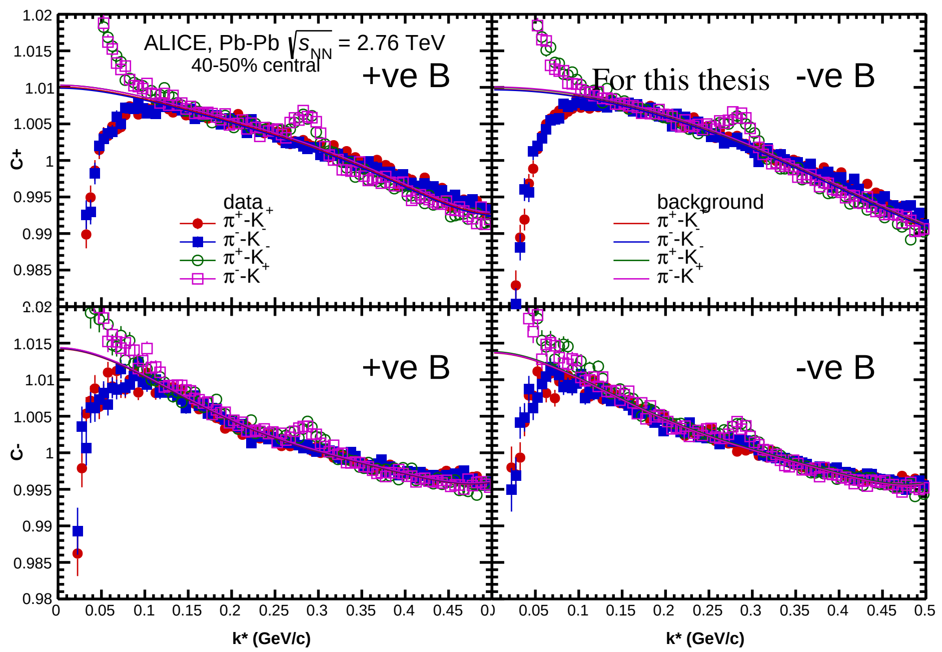

Figure 5.23: The pion-kaon correlation functions with pair cuts in *Out* directions for 40-50% centrality bin for Pb−Pb collisions at $\sqrt{s_{\rm NN}}$= 2.76 TeV recorded by ALICE at the LHC. The background curve is a 6th order polynomial function

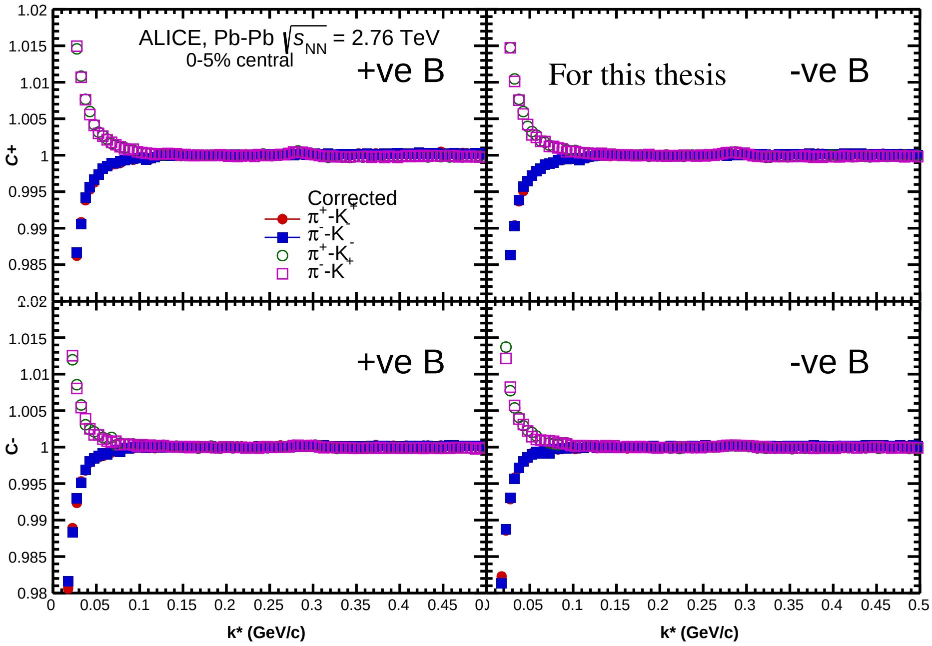

Figure 5.24: The background corrected pion-kaon correlation functions with pair cuts in *Out* directions for 0-5% centrality bin in Pb−Pb collisions at $\sqrt{s_{NN}}$= 2.76 TeV recorded by ALICE at the LHC.

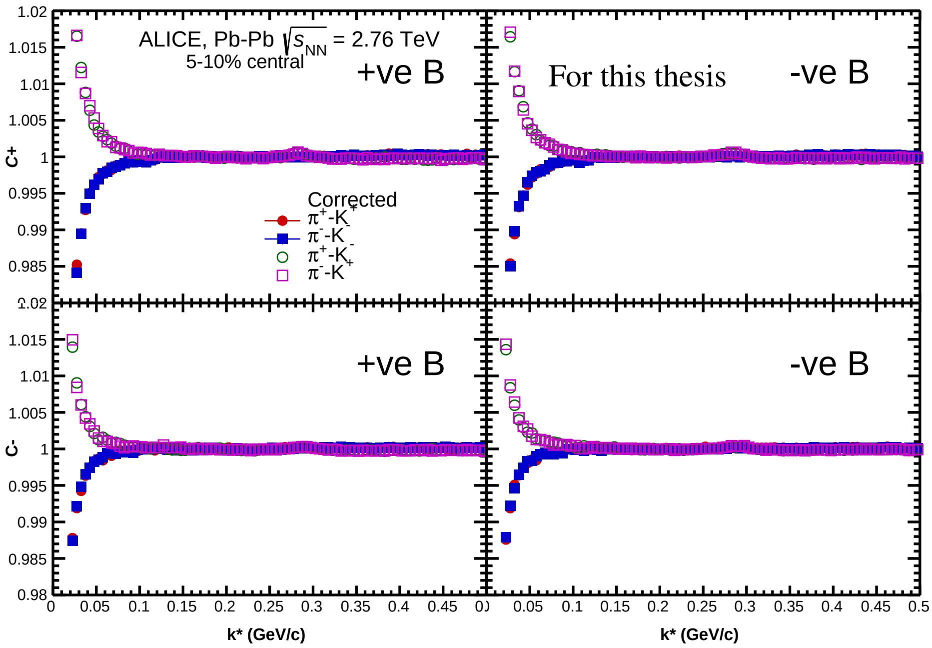

Figure 5.25: The background corrected pion-kaon correlation functions with pair cuts in *Out* directions for 5-10% centrality bin in Pb−Pb collisions data at $\sqrt{s_{NN}}$= 2.76 TeV recorded by ALICE at the LHC.

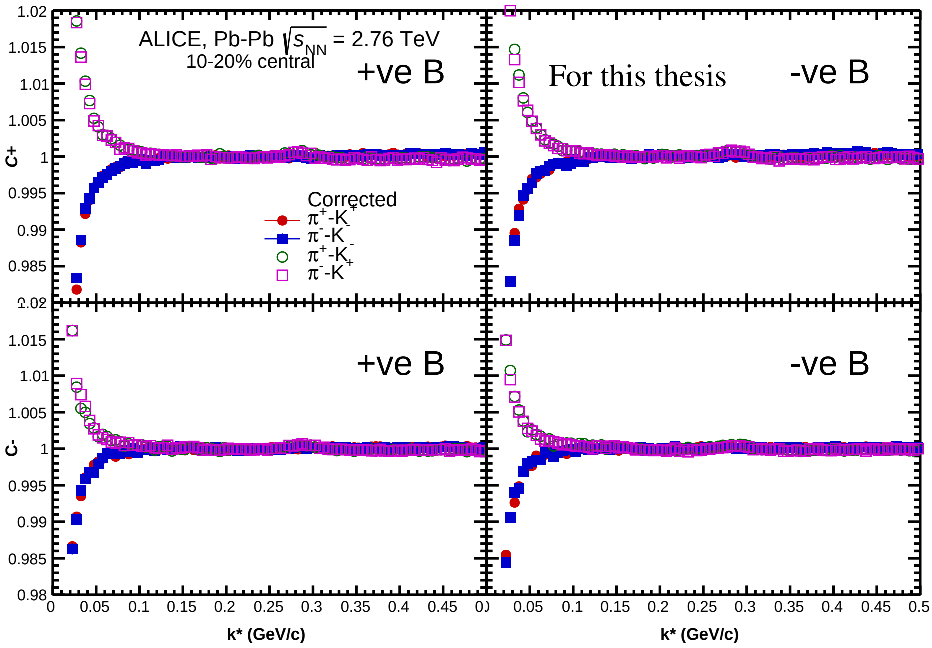

Figure 5.26: Non-femtoscopic background corrected pion-kaon correlation functions with pair cuts in *Out* directions for 10-20% centrality bin from Pb−Pb collisions data at $\sqrt{s_{\mathrm{NN}}}$= 2.76 TeV recorded by ALICE at the LHC.

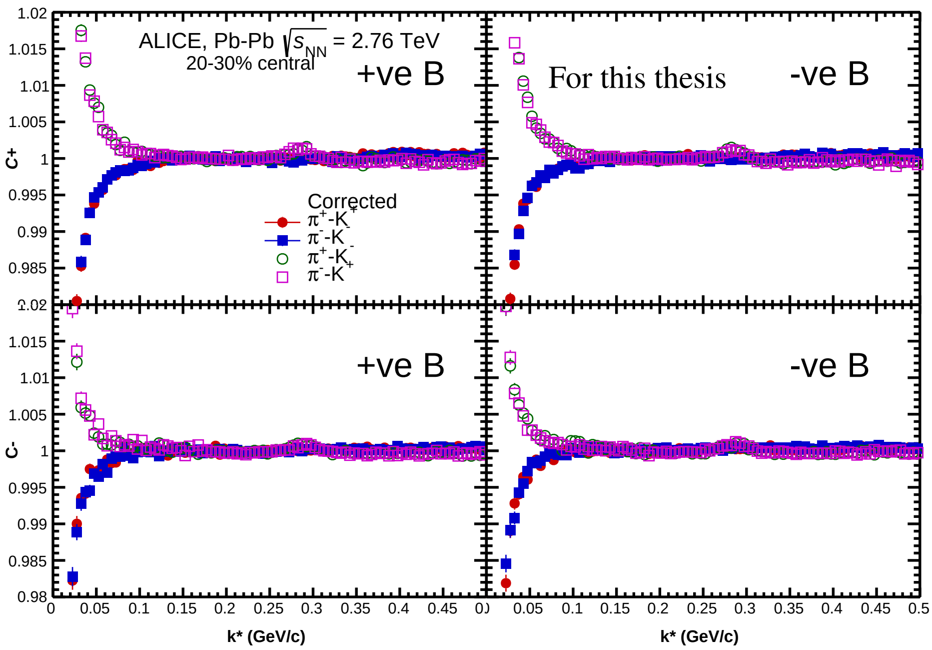

Figure 5.27: The background corrected pion-kaon correlation functions with pair cuts in *Out* directions for 20-30% centrality bin in Pb−Pb collisions data at $\sqrt{s_{\mathrm{NN}}}$= 2.76 TeV recorded by ALICE at the LHC.

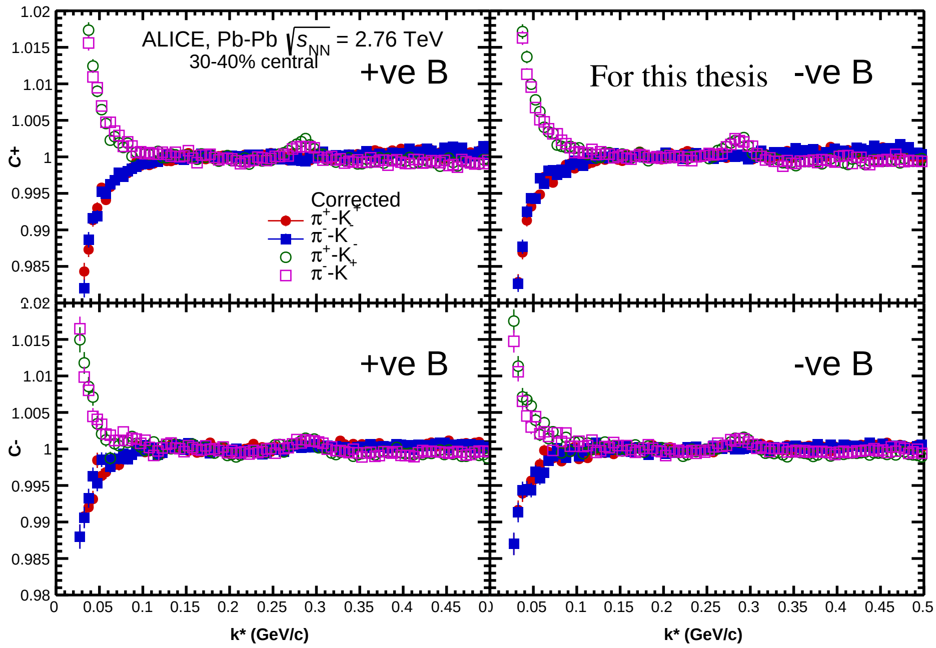

Figure 5.28: The background corrected pion-kaon correlation functions with pair cuts in *Out* directions for 30-40% centrality bin in Pb−Pb collisions data at $\sqrt{s_{\mathrm{NN}}}$= 2.76 TeV recorded by ALICE at the LHC.

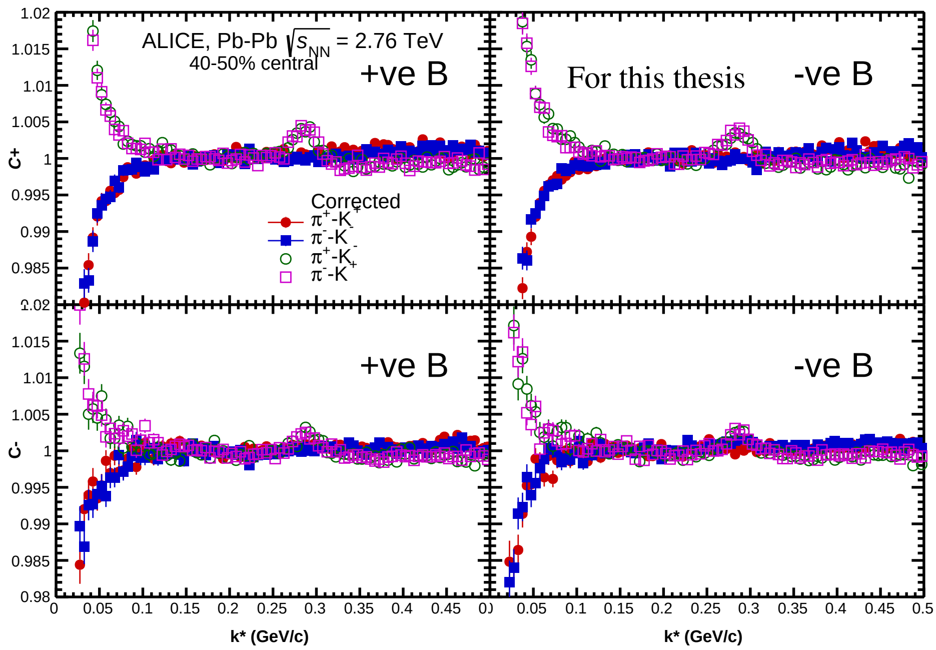

Figure 5.29: The background corrected pion-kaon correlation functions with pair cuts in *Out* directions for 40-50% centrality bin in Pb−Pb collisions data at $\sqrt{s_{\mathrm{NN}}}$= 2.76 TeV recorded by ALICE at the LHC.

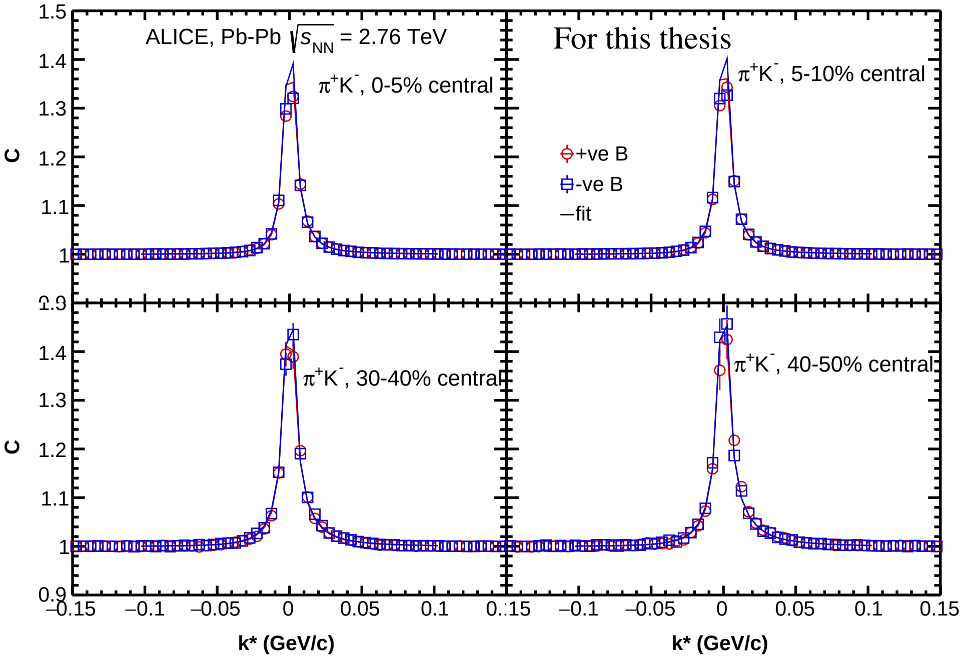

Figure 5.30: π^+K^- correlation functions for different centrality bins from Pb−Pb collisions data at $\sqrt{s_{NN}}$= 2.76 TeV recorded by ALICE at the LHC. The curves are fitting of the correlation function.

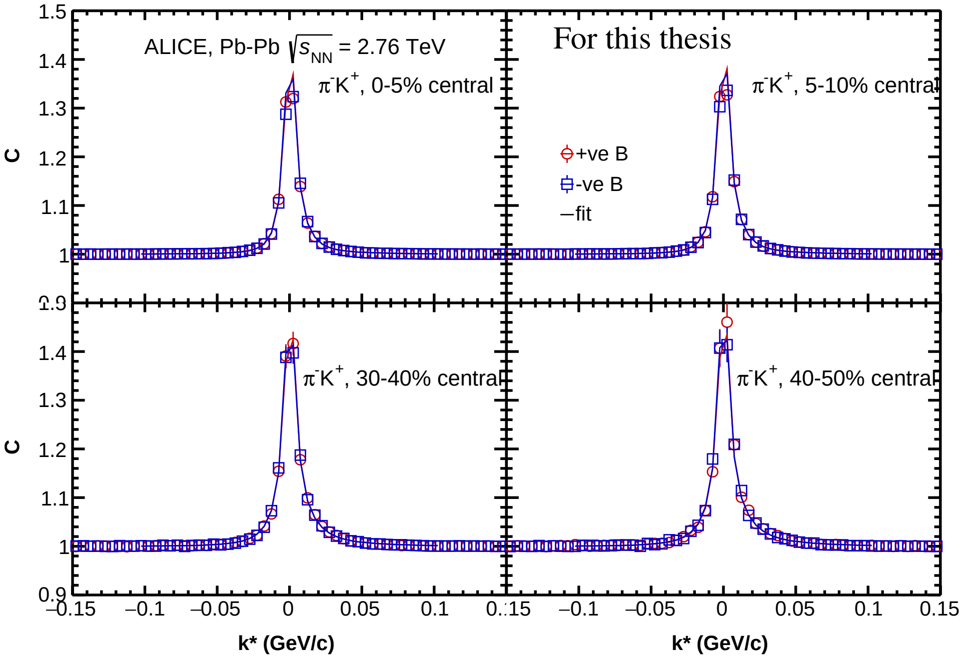

Figure 5.31: π^-K^+ correlation functions for different centrality bins from Pb−Pb collisions data at $\sqrt{s_{NN}}$= 2.76 TeV recorded by ALICE at the LHC. The curves are fitting of the correlation function.

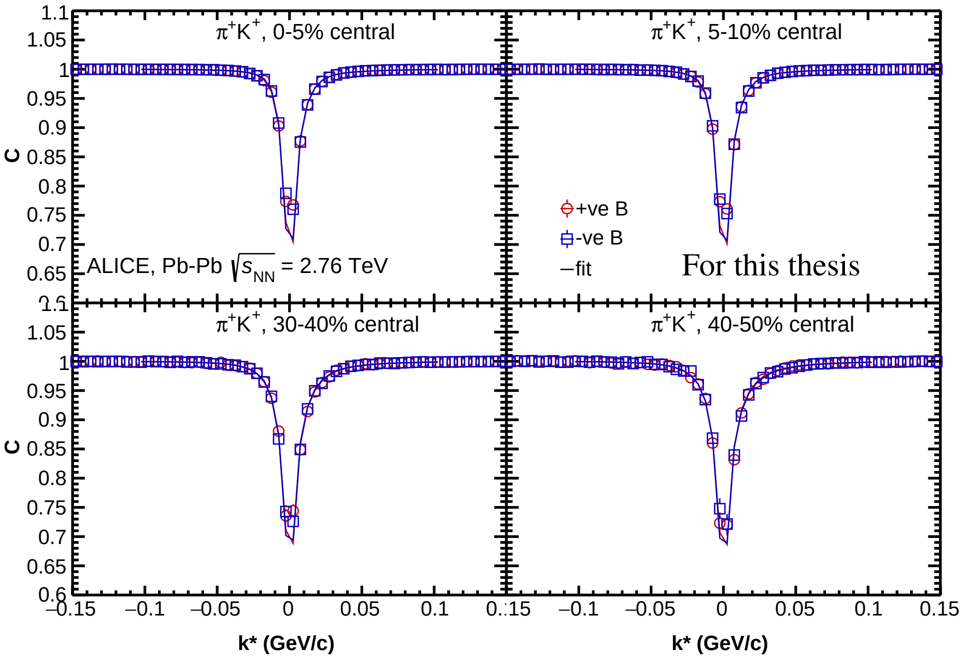

Figure 5.32: π^+K^+ correlation functions for different centrality bins for Pb−Pb collisions at $\sqrt{s_{NN}}$= 2.76 TeV recorded by ALICE at the LHC. The curves are fits to the correlation function.

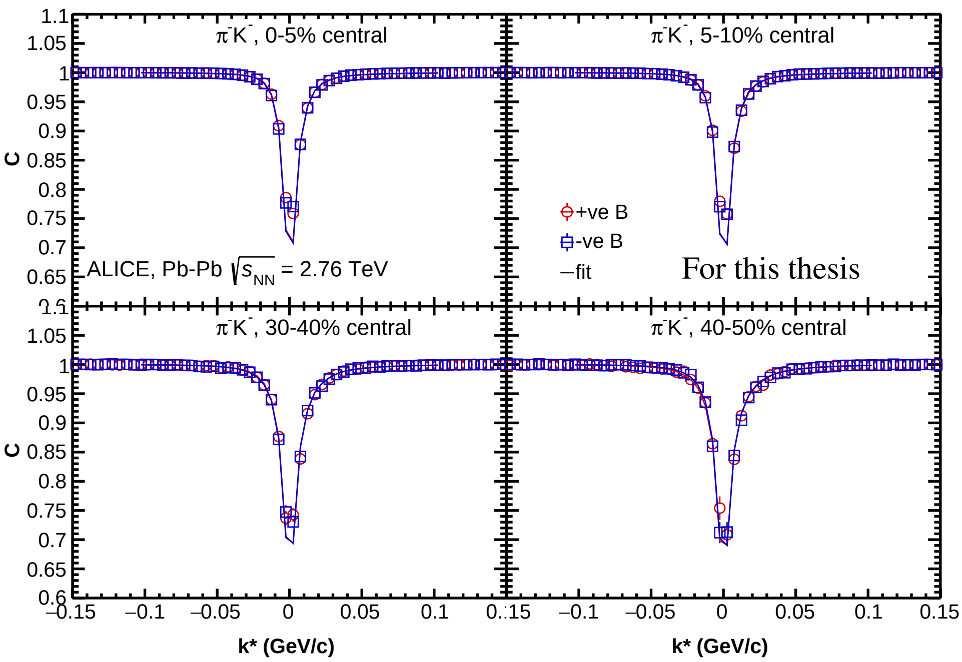

Figure 5.33: π^-K^- correlation functions for different centrality bins for Pb−Pb collisions at $\sqrt{s_{NN}}$= 2.76 TeV recorded by ALICE at the LHC. The curves are fits to the correlation function.

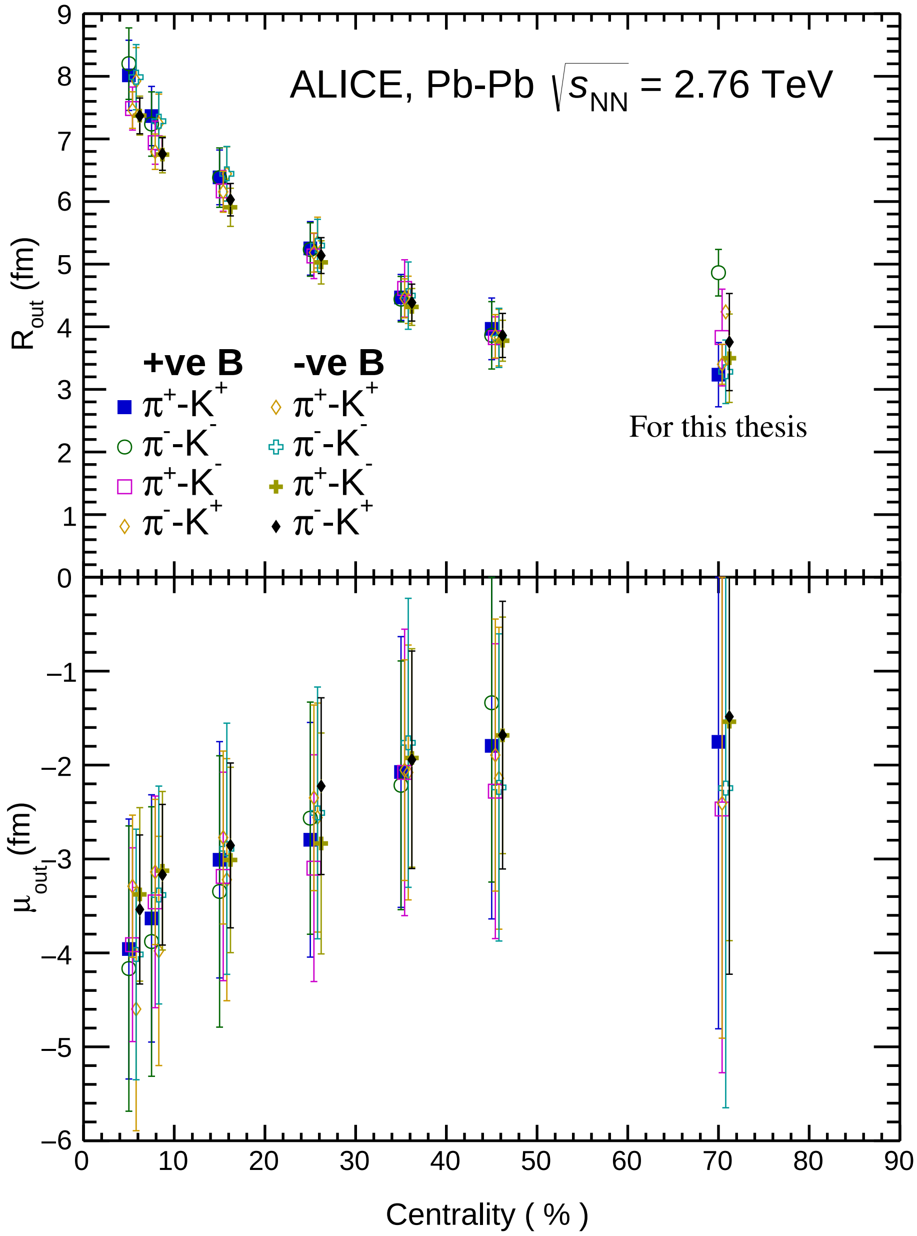

Figure 5.34: (Upper panel) The variation of the average size of the pion-kaon homogeneity region with centrality for all charge combinations for both positive and negative polarity of magnetic fields. (Lower panel) The variation of μ with centrality for all charge combinations for both positive and negative polarity of magnetic fields

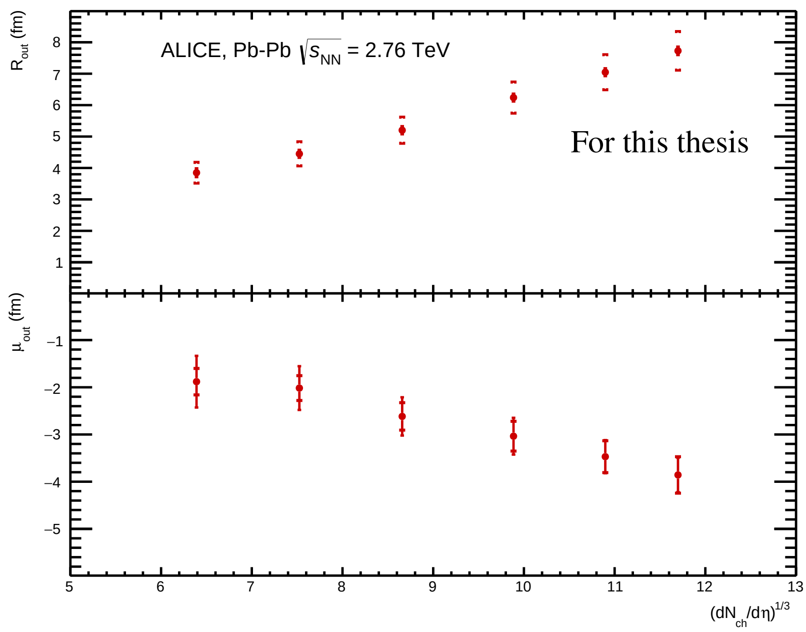

Figure 5.35: (Upper panel) The variation of the average size of the pion-kaon homogeneity region with centrality. (Lower panel) The variation of μ with centrality (Both size and μ are averaged over all charge combinations for both positive and negative polarity of magnetic fields)

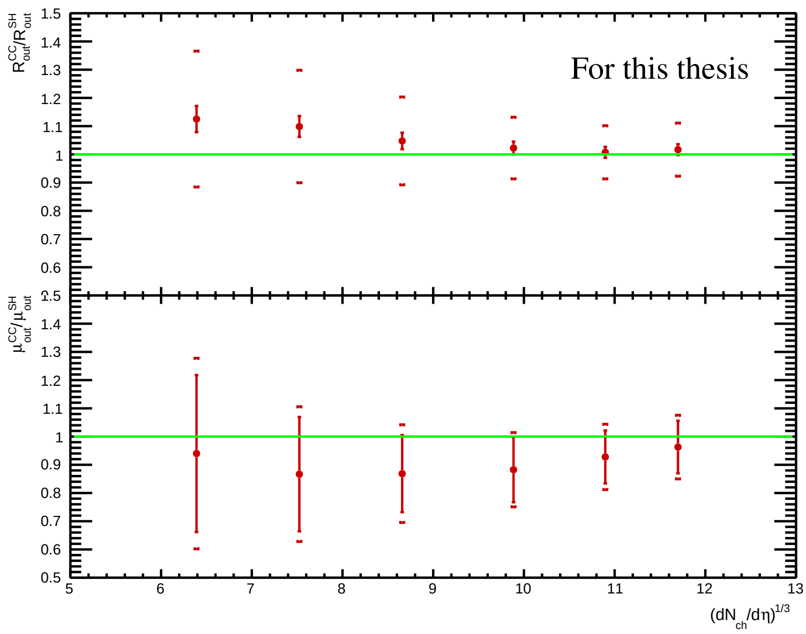

Figure 5.36: Comparison of the source parameters obtained from the cartesian coordinate method with that of the spherical harmonics approach. (Result from the spherical harmonics approach is taken from reference [59])

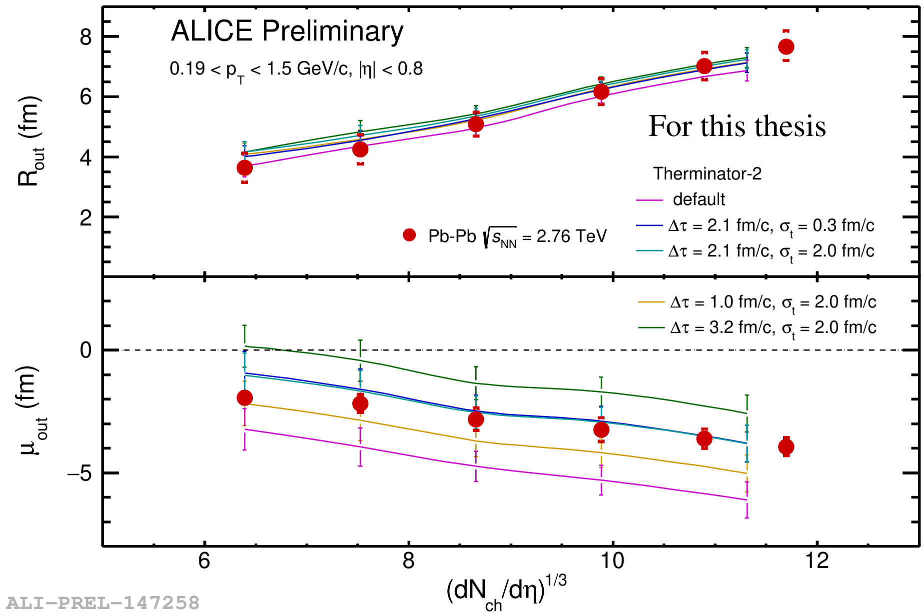

Figure 5.37: (**Upper panel**) The variation of average source size with $(dN_{ch}/d\eta)^{(\frac{1}{3})}$. (**Lower panel**) μ with $(dN_{ch}/d\eta)^{(\frac{1}{3})}$ (lower panel). The experimental results are compared with expectations of Therminator2 coupled with (3+1) viscous hydrodynamics model for different values of kaon delay time. Therminator2 results are taken from reference [65].

Chapter 6

Summary and Outlook

> *"Insanity is doing the same thing over and over again and expecting different results."* – Albert Einstein

The work in this thesis presents the non-identical particle femtoscopic studies which led to a better understanding of the measured emission asymmetry between pions and kaons in the system produced in heavy ion collisions. This is the first ever measurement of emission asymmetry at the LHC using the ALICE detector. The study has been performed using the data collected by ALICE experiment at LHC in Pb−Pb collisions at $\sqrt{s_{\rm NN}}$= 2.76 TeV for different polarities of applied magnetic field. The correlation function was calculated for pion-kaon pairs for all charge combinations. The analysis was carried out in different centrality classes namely 0-5%, 5-10%, 10-20%, 20-30%, 30-40% and 40-50%. The detailed steps of the femtoscopic technique required to determine the size of the homogeneity region of pion-kaon emission and the emission asymmetry have been described. The analysis reported in this thesis was performed with the cartesian coordinate formalism. The method involved the construction of correlation function and the Double Ratio of the pion-kaon pairs. The pions and kaons were identified by the combined information provided by the TPC and the TOF detector in different momentum ranges. The selected pairs were corrected for the two-track merging effects due to detector resolution. The mis-identified $e^{+}e^{-}$ pairs originating from γ conversions were also eliminated by using suitable selection cuts. The correlation functions and double ratios were obtained for all charge combinations of pion-kaon pairs in different centrality classes. The study was also performed in different polarities of the magnetic field to observe the influence of the magnetic field. The obtained correlation function was also corrected for the background pairs, originating from non-femtoscopic sources like elliptic flow, resonance decay etc. The relevant parameters of the source, namely the size and the emission asymmetry was extracted by fitting the correlation function using the Corrfit software. The algorithm assumed a three-dimensional Gaussian profile for the emitting source. The purity and the momentum resolution corrections were also applied to the fitting process in order to obtain the best estimate of the source parameters. The double ratio deviated from unity in the *Out* direction for all combinations of pion-kaon pairs. This observation indicated that the space-time position of pion and kaon emissions are not same and the pions are emitted closer to the centre of the source compared to kaons. The kaons are emitted earlier than pions.

It has been found that the average size of the pion-kaon homogeneity region and the emission asymmetry decreases for all charge combinations from most central to peripheral collisions. The convoluted radius of the pion-kaon emitting source in *Out* direction is of the order of 7 – 8 fm for the most central collisions and decreases to about 2.5 fm for peripheral collisions. This trend is consistent with the previous measurements of source size using identical particle femtoscopy. The same trend is followed for the emission asymmetry in *Out* direction. For the most central collisions, it has a value about 4 fm. It starts decreasing for peripheral collisions and is around 2 fm. The trend of emission asymmetry with respect to centrality is also similar to source size consistent with the previous observation at RHIC energies. The obtained results are also compared to the expectations of Therminator2 event generator coupled with (3+1)-dimensional viscous hydrodynamic calculations. The pion-kaon emission asymmetry obtained with the model agreed with the experimental observation when an additional time delay of 2.1 fm/c was introduced for kaons. The results obtained in this analysis are consistent with the hydrodynamic-induced evolution of the system created in heavy ion collisions and favors a stronger radial flow in central collisions. The asymmetry can be understood by the strong radial flow hypothesis and the interplay between the collective and thermal movement of the dense matter created in collisions of heavy ions.

6.1 Future perspective

The pion-kaon femtoscopy analysis presented in this thesis measures convoluted radii of pion-kaon system (equation 6.1) and not the exclusive radii of pion system or kaon system as measured in identical particle femtoscopy.

$$R^{\pi K}_{Out} = \sqrt{(R^{\pi}_{Out})^2 + (R^{K}_{Out})^2} \tag{6.1}$$

The three radii $R_{\pi K}$, R_{Kp} and $R_{\pi p}$ are required to get radii of pion, kaon and proton systems (equation 6.2, 6.3 and 6.4), separately.

$$R^{\pi}_{Out} = \sqrt{\frac{(R^{\pi K}_{Out})^2 + (R^{\pi p}_{Out})^2 - (R^{Kp}_{Out})^2}{2}} \tag{6.2}$$

$$R^{K}_{Out} = \sqrt{\frac{(R^{\pi K}_{Out})^2 - (R^{\pi p}_{Out})^2 + (R^{Kp}_{Out})^2}{2}} \tag{6.3}$$

$$R^{p}_{Out} = \sqrt{\frac{-(R^{\pi K}_{Out})^2 + (R^{\pi p}_{Out})^2 + (R^{Kp}_{Out})^2}{2}} \tag{6.4}$$

Similarly, in the case of relations between emission asymmetries, $\mu_{\pi p}$ is expected to be larger compared to $\mu_{\pi K}$ and μ_{Kp} due to difference in masses. μ_{Kp} is expected to be smaller compared to $\mu_{\pi K}$. Thus, one expects the following relation :

$$\mu_{\pi p} = \mu_{\pi K} + \mu_{Kp} \tag{6.5}$$

Therefore, it will be very interesting to study the femtoscopic correlations between pairs like pion-proton and kaon-proton to get the complete space-time picture of three systems. The study of strong interaction parameter can be done by analyzing the unlike-sign pairs of kaons and protons where correlation functions are expected to be similar to Yukawa-like strong interaction potential. The study of $K - p$ femtoscopic correlations in high multiplicity p−p collisions, for example, at 13 TeV can give information about strong interaction in smaller systems. It will be also interesting to study the femotoscpic correlations for non-identical pairs ($\pi - K$, $K - p$, $\pi - p$) at other higher LHC energies (like Pb−Pb at $\sqrt{s_{\rm NN}}$=5.02 TeV and Xe−Xe at $\sqrt{s_{\rm NN}}$=5.44 TeV) to study the energy and system size dependence of the source parameters.

Publications and Conference Proceedings

Data analysis: Paper draft for analysis "Pion-kaon femtoscopy in Pb-Pb collisions at $\sqrt{s_{\mathrm{NN}}}$= 2.76 TeV with ALICE at the LHC" is under communication with ALICE Internal Review Committee (IRC).

Publications :

1. Sadhana Dash, Basanta K. Nandi, Ranjit Nayak, **Ashutosh Kumar Pandey**, Priyanka Sett, " Comprehending particle production at RHIC and LHC energies using global measurements", Mod. Phys. Lett. A 32, 1750060 (2017), arXiv:1609.08609

2. **Ashutosh Kumar Pandey**, Priyanka Sett, Sadhana Dash "Weibull Distribution and the multiplicity moments in $pp(p\bar{p})$ collisions ", Phys. Rev. D 96, 074006 (2017), arXiv:1706.07585

3. ALICE collaboration publications link: `http://inspirehep.net/author/profile/Ashutosh.Kumar.Pandey.1`

Conference Proceedings :

1. **Ashutosh Kumar Pandey** (for ALICE collaboration) "Non-identical particle femtoscopy in Pb−Pb collisions at $\sqrt{s_{\mathrm{NN}}}$= 2.76 TeV measured with ALICE", to be published in PoS (Proceedings of Science)

2. **Ashutosh Kumar Pandey** (for ALICE collaboration) "Pion-kaon femtoscopy in Pb−Pb collisions at $\sqrt{s_{\mathrm{NN}}}$= 2.76 TeV ", *Nuclear Physics A, Volume 982, February 2019, Pages 351-354* (arXiv:1807.10072 [hep-ex])

3. **Ashutosh Kumar Pandey**, Ranjit Nayak, Basanta. K. Nandi, Sadhana Dash and Priyanka Sett, "Study of centrality and beam energy dependence of $dN_{ch}/d\eta$ and

$dE_T/d\eta$ at midrapidity using two component approach ", Published in *XXII DAE High Energy Physics Symposium, pages 267-270, Cham, 2018. Springer International Publishing*.

4. Ranjit Nayak, Sadhana Dash and **Ashutosh Kumar Pandey**, “Weibull Approach to Study Multiplicity Moments in e^+e^- and $p\bar{p}$ Collisions", Published in *XXII DAE High Energy Physics Symposium, pages 263-266, Cham, 2018. Springer International Publishing*.

Conference and Workshop:

1. Poster (Title: Non-identical particle femtoscopy in Pb−Pb collisions at $\sqrt{s_{\rm NN}}$= 2.76 TeV with ALICE at LHC) XXXIX International Conference on High Energy Physics (ICHEP2018), COEX, SEOL, 04-11 July 2018
2. Talk (Title: Pion-kaon femtoscopy in Pb-Pb collisions at $\sqrt{s_{\rm NN}}$= 2.76 TeV) in QM2018 The 27th Int. Con. on Ultrarelativistic Nucleus-Nucleus Collisions, Venezia, Italy, 13-19 May 2018
3. Invited talk (Title: Recent results from femtoscopic studies with ALICE at LHC) in 9th International Workshop on Multiple Partonic Interactions at the LHC, Hotel Peterhoff, Shimla, India, 11-15 December 2017
4. Talk (Title: Study of centrality and beam energy dependence of $dN_{ch}/d\eta$ and $dE_T/d\eta$ at midrapidity using two component approach) in XXII DAE-BRNS HIGH ENERGY PHYSICS SYMPOSIUM 2016, University of Delhi, December 12-16, 2016
5. International Conference on Triggering Discoveries in High Energy Physics, Department of Physics and Electronics, University of Jammu, Jammu - 180006, India, September 9 - 14, 2013

Acknowledgements

This thesis work would not have been possible without the help and support I received from many people.

First and foremost, I would like to express my gratitude and thanks to my thesis supervisor Prof. Sadhana Dash, for her constant support and help not only as supervisor but also as a friend. She has always trusted and supported me whenever I felt down as a researcher and human. Many times, she has shown her big heart and love towards me by forgiving my mistakes as a student. Whatever I have achieved during my PhD is due to her guidance, support and blessing. She is not only my PhD supervisor, but also my teacher, friend, guardian and inspiration for me. I do not have words to express my respect, love and gratitude towards her. I will just say that she maid me better person and student.

I would like to thank Prof. Basanta Kumar Nandi whom has always given the best advice for me. He is an inspiration for me both as a teacher and as a researcher. He is a very disciplined and good man. He has very good understanding and thinking capability which make his thought interesting during a discussion. I would like to express my gratitude towards him for his teaching, support, advise and blessing.

I would also like to thank Prof. Raghava Varma for his blessing, love and support. He is the one of my RPC member along with Prof. Basanta Kumar Nandi. Prof. Varma is a very great person and understands what a student may face during his study. He is very supportive and even cooked for me during my first CERN visit. I would also like to show my gratitude for his valuable advice for my research work as well as in life.

I would also like to express my gratitude to Prof R.P.Malik from Banaras Hindu University.

I would like to extend my thanks to Prof. Adam Kisiel and Prof. Lukasz Graczykowski from Warsaw University of Technology (WUT), Warsaw, Poland for their support and guidance for my research work. Prof. Kisiel is like supervisor to me. He has great knowledge and understanding of physics. His suggestions are really important for my work. Prof. Lukasz Graczykowski is like a friend and mentor to me and helped me a lot. It is an honor to me to work with Prof. Kisiel and Prof. Lukasz Graczykowski. I am also thankful to Przemyslaw Karczmarczyk, Ewa Katarzyna Lobejko and FEMTO group people from WUT for their support and suggestions.

As a part of ALICE-India collaboration and PMD installation team, I would like to thank my service work supervisor Prof. Tapan Kumar Nayak, Partha Bhaskar, Ram Narayan, Anik Gupta, Jogendra Saini, Sudhanta Pal, Sanjib Muhuri for their support and guidance. I would also like to thank my all friends from ALICE-India collaboration including Kishora Nayak, Samrangy Sadhu, Arvind Khuntia, Shushant Tripathy and seniors for their support, love and help.

Being a CERN and ALICE member, I would like to express my gratitude and respect to all PWGCF, PAG Femtoscopy conveners and CERN members for their valuable advise and support.

I would also like to extend my thanks to my seniors including Prabhat Pujari, Satyajit Jena, Nirbhay Kumar Behera, Greeshma, Amal Sarkar, Jitendra Nogia, Shyam Kumar and Siddhesh Sawant for their support and guidance in my earlier days of PhD. I am thankful to my juniors Bharati Naik, Preeti Dhankar, Ranjit Nayak, Baidyanath Sahoo, Pritam Chakraborty, Tulika Tripathy, Dibakar Bauri, Sonali and Santosh for their love and respect.

Being an IIT student, I would like to thank people from academic office, hostel, mess, department, security and other IIT members and employees for all their support and help.

I would also like to acknowledge my lovely friends Priya Tiwari, Vivek Kumar Singh, Suman Bharati, Amit Kumar Singh, Avinash Singh, Shailesh Kumar Pandey, Priya Chauhan, Vipin, Anurag Sharma, Nitika Tiwari and all my other friends for their support, help and love.

My deepest gratitude is to my parents, sister, brother, late sister-in-law Puja Pandey and every family member for their hard-work and trust, love, affection towards me. Whatever, I am today is due to their support and sacrifice for me.

Finally, I offer my prayer to the almighty God Lord Shiva and every divine power for giving me human life and strength.

Bibliography

[1] Science. https://en.wikipedia.org/wiki/Science, . Accessed: 27-02-2019.

[2] Branches of biology. https://en.wikipedia.org/wiki/Biology#Branches, . Accessed: 30-07-2018.

[3] Periodic table. http://drrajivdesaimd.com/2014/07/26/the-atom, . Accessed: 27-02-2019.

[4] Chemistry. https://en.wikipedia.org/wiki/Chemistry, . Accessed: 30-07-2018.

[5] Physics. https://en.wikipedia.org/wiki/Physics, . Accessed: 09-04-2019.

[6] States of matter. https://www.livescience.com/46506-states-of-matter.html, . Accessed: 09-04-2019.

[7] State of matter. https://en.wikipedia.org/wiki/State_of_matter, . Accessed: 09-04-2019.

[8] Four forces. https://en.wikipedia.org/wiki/Fundamental_interaction, . Accessed: 06-08-2018.

[9] Newton's law of universal gravitation. https://en.wikipedia.org/wiki/Gravitational_constant, . Accessed: 02-08-2018.

[10] Maxwell's equations. http://electrical-laws.blogspot.com/2013/02/maxwells-equations.html, . Accessed: 04-08-2018.

[11] Beta decay. https://en.wikipedia.org/wiki/Weak_interaction#/media/File:Beta-minus_Decay.svg, . Accessed: 05-08-2018.

[12] State of matter. https://physics.info/standard/, . Accessed: 09-04-2019.

[13] Andreas S. Kronfeld and Chris Quigg. Resource letter qcd-1: Quantum chromodynamics. *American Journal of Physics*, 78(11):1081–1116, 2010. doi: 10.1119/1.3454865. URL https://doi.org/10.1119/1.3454865.

[14] Strong coupling constant. https://people.nscl.msu.edu/~witek/Classes/PHY802/QCD2.pdf, . Accessed: 023-08-2018.

[15] Raymond Brock et al. Handbook of perturbative QCD: Version 1.0. *Rev. Mod. Phys.*, 67:157–248, 1995. doi: 10.1103/RevModPhys.67.157.

[16] H. David Politzer. Reliable perturbative results for strong interactions? *Phys. Rev. Lett.*, 30:1346–1349, Jun 1973. doi: 10.1103/PhysRevLett.30.1346. URL https://link.aps.org/doi/10.1103/PhysRevLett.30.1346.

[17] S. Bethke. Experimental tests of asymptotic freedom. *Progress in Particle and Nuclear Physics*, 58(2):351 – 386, 2007. ISSN 0146-6410. doi: https://doi.org/10.1016/j.ppnp.2006.06.001. URL http://www.sciencedirect.com/science/article/pii/S0146641006000615.

[18] Rajan Gupta. Introduction to lattice qcd. arXiv:hep-lat/9807028.

[19] Frithjof Karsch. Lattice qcd at high temperature and density. arXiv:hep-lat/0106019, 2001.

[20] QCD phase diagram. http://www.jicfus.jp/en/promotion/pr/mj/guido-cossu/, . Accessed: 01-10-2018.

[21] Heavy-ion collisions. https://u.osu.edu/vishnu/2015/07/22/photon-emission-from-relativistic-heavy-ion-collisions/. Accessed: 27-02-2019.

[22] QGP evolution. https://particlesandfriends.wordpress.com/2016/10/14/evolution-of-collisions-and-qgp/, . Accessed: 01-10-2018.

[23] Elliptic flow of identified hadrons in pb-pb collisions at 2.76 tev. *Journal of High Energy Physics*, 2015(6):190, Jun 2015. ISSN 1029-8479. doi: 10.1007/JHEP06(2015)190. URL https://doi.org/10.1007/JHEP06(2015)190.

[24] Multi-strange baryon production at mid-rapidity in pbâĂŞpb collisions at snn=2.76 tev. *Physics Letters B*, 728:216 – 227, 2014. ISSN 0370-2693. doi: https://doi.org/10.1016/j.physletb.2013.11.048. URL http://www.sciencedirect.com/science/article/pii/S0370269313009544.

[25] Evidence from d + Au measurements for final-state suppression of high-p_T hadrons in Au + Au collisions at rhic. *Phys. Rev. Lett.*, 91:072304, Aug 2003. doi: 10.1103/PhysRevLett.91.072304. URL https://link.aps.org/doi/10.1103/PhysRevLett.91.072304.

[26] Particle-yield modification in jetlike azimuthal dihadron correlations in pb-pb collisions at $\sqrt{s_{\mathrm{NN}}}$ = 2.76 TeV. *Phys. Rev. Lett.*, 108:092301, Mar 2012. doi: 10.1103/PhysRevLett.108.092301. URL https://link.aps.org/doi/10.1103/PhysRevLett.108.092301.

[27] Suppression of charged particle production at large transverse momentum in central pbâĂŞpb collisions at snn=2.76 tev. *Physics Letters B*, 696(1):30 – 39, 2011. ISSN 0370-2693. doi: https://doi.org/10.1016/j.physletb.2010.12.020. URL http://www.sciencedirect.com/science/article/pii/S0370269310013973.

[28] J. Adam et al. Direct photon production in pbâĂŞpb collisions at snn=2.76Âătev. *Physics Letters B*, 754:235 – 248, 2016. ISSN 0370-2693. doi: https://doi.org/10.1016/j.physletb.2016.01.020. URL http://www.sciencedirect.com/science/article/pii/S0370269316000320.

[29] Baldo SahlmÃijller. Direct photon measurement in Pb-Pb collisions at $\sqrt{s_{\mathrm{NN}}} = 2.76$ TeV with ALICE. *Nucl. Phys.*, A956:421–424, 2016. doi: 10.1016/j.nuclphysa.2016.03.052.

[30] One-dimensional pion, kaon, and proton femtoscopy in pb-pb collisions at $\sqrt{s_{NN}}$ = 2.76 tev. *Phys. Rev. C*, 92:054908, Nov 2015. doi: 10.1103/PhysRevC.92.054908. URL https://link.aps.org/doi/10.1103/PhysRevC.92.054908.

[31] R. HANBURY BROWN and R. Q. TWISS. A test of a new type of stellar interferometer on sirius. *Nature*, 178(4541):1046–1048, 1956. ISSN 1476-4687. doi: 10.1038/1781046a0. URL https://doi.org/10.1038/1781046a0.

[32] R. Hanbury Brown and R.Q. Twiss. Lxxiv. a new type of interferometer for use in radio astronomy. *The London, Edinburgh, and Dublin Philosophical Magazine and Journal of Science*, 45(366):663–682, 1954. doi: 10.1080/14786440708520475. URL https://doi.org/10.1080/14786440708520475.

[33] Gerson Goldhaber, William B. Fowler, Sulamith Goldhaber, T. F. Hoang, Theodore E. Kalogeropoulos, and Wilson M. Powell. Pion-pion correlations in antiproton annihilation events. *Phys. Rev. Lett.*, 3:181–183, Aug 1959.

doi: 10.1103/PhysRevLett.3.181. URL https://link.aps.org/doi/10.1103/PhysRevLett.3.181.

[34] Michael Annan Lisa, Scott Pratt, Ron Soltz, and Urs Wiedemann. Femtoscopy in relativistic heavy ion collisions: Two decades of progress. *Annual Review of Nuclear and Particle Science*, 55:357–402, 2005. ISSN 0163-8998. doi: 10.1146/annurev.nucl.55.090704.151533.

[35] G. Bertsch, M. Gong, and M. Tohyama. Pion Interferometry in Ultrarelativistic Heavy Ion Collisions. *Phys. Rev.*, C37:1896–1900, 1988. doi: 10.1103/PhysRevC.37.1896.

[36] S. Pratt, T. Csorgo, and J. Zimanyi. Detailed predictions for two pion correlations in ultrarelativistic heavy ion collisions. *Phys. Rev.*, C42:2646–2652, 1990. doi: 10.1103/PhysRevC.42.2646.

[37] Adam Kisiel. Nonidentical-particle femtoscopy at $\sqrt{s_{NN}} = 200$ gev in hydrodynamics with statistical hadronization. *Phys. Rev. C*, 81:064906, Jun 2010. doi: 10.1103/PhysRevC.81.064906. URL https://link.aps.org/doi/10.1103/PhysRevC.81.064906.

[38] Adam Kisiel. *Studies of non-identical meson-meson correlations at low relative velocities in relativistic heavy-ion collisions registered in the STAR experiment*. PhD thesis, 2004.

[39] J. Adams et al. Pion kaon correlations in Au+Au collisions at s(NN)**1/2 = 130-GeV. *Phys. Rev. Lett.*, 91:262302, 2003. doi: 10.1103/PhysRevLett.91.262302.

[40] Lyndon Evans and Philip Bryant. LHC Machine. *JINST*, 3:S08001, 2008. doi: 10.1088/1748-0221/3/08/S08001.

[41] LHC Guide. Mar 2017. URL https://cds.cern.ch/record/2255762.

[42] The ALICE Collaboration. The alice experiment at the cern lhc. *Journal of Instrumentation*, 3(08):S08002, 2008. URL http://stacks.iop.org/1748-0221/3/i=08/a=S08002.

[43] S. BeolÃĺ. The alice inner tracking system: Performance with proton and lead beams. *Physics Procedia*, 37:1062 – 1069, 2012. ISSN 1875-3892. doi: https://doi.org/10.1016/j.phpro.2012.02.443. URL http://www.sciencedirect.com/

science/article/pii/S1875389212017981. Proceedings of the 2nd International Conference on Technology and Instrumentation in Particle Physics (TIPP 2011).

[44] P. Kuijer. The inner tracking system of the alice experiment. *Nuclear Instruments and Methods in Physics Research Section A: Accelerators, Spectrometers, Detectors and Associated Equipment*, 530(1):28 – 32, 2004. ISSN 0168-9002. doi: https://doi.org/10.1016/j.nima.2004.05.042. URL http://www.sciencedirect.com/science/article/pii/S0168900204010289. Proceedings of the 6th International Conference on Large Scale Applications and Radiation Hardness of Semiconductor Detectors.

[45] Christian Lippmann. Performance of the alice time projection chamber. *Physics Procedia*, 37:434 – 441, 2012. ISSN 1875-3892. doi: https://doi.org/10.1016/j.phpro.2012.02.390. URL http://www.sciencedirect.com/science/article/pii/S187538921201721X. Proceedings of the 2nd International Conference on Technology and Instrumentation in Particle Physics (TIPP 2011).

[46] The alice tpc, a large 3-dimensional tracking device with fast readout for ultra-high multiplicity events. *Nuclear Instruments and Methods in Physics Research Section A: Accelerators, Spectrometers, Detectors and Associated Equipment*, 622(1):316 – 367, 2010. ISSN 0168-9002. doi: https://doi.org/10.1016/j.nima.2010.04.042. URL http://www.sciencedirect.com/science/article/pii/S0168900210008910.

[47] The alice transition radiation detector: Construction, operation, and performance. *Nuclear Instruments and Methods in Physics Research Section A: Accelerators, Spectrometers, Detectors and Associated Equipment*, 881:88 – 127, 2018. ISSN 0168-9002. doi: https://doi.org/10.1016/j.nima.2017.09.028. URL http://www.sciencedirect.com/science/article/pii/S0168900217309981.

[48] A. Alici. Particle identification with the alice time-of-flight detector at the lhc. *Nuclear Instruments and Methods in Physics Research Section A: Accelerators, Spectrometers, Detectors and Associated Equipment*, 766:288 – 291, 2014. ISSN 0168-9002. doi: https://doi.org/10.1016/j.nima.2014.05.059. URL http://www.sciencedirect.com/science/article/pii/S0168900214005993. RICH2013 Proceedings of the Eighth International Workshop on Ring Imaging Cherenkov Detectors Shonan, Kanagawa, Japan, December 2-6, 2013.

[49] G. De Cataldo. The high momentum particle identification detector in alice at lhc. *Nuclear Physics B - Proceedings Supplements*, 177-178:273 – 275, 2008. ISSN 0920-5632. doi: https://doi.org/10.1016/j.nuclphysbps.2007.11.127. URL http://www.sciencedirect.com/science/article/pii/S0920563207009565. Proceedings of the Hadron Collider Physics Symposium 2007.

[50] G. Conesa, H. Delagrange, J. DÃŋaz, M. Ippolitov, Y.V. Kharlov, D. Peressounko, and Y. Schutz. Performance of the alice photon spectrometer phos. *Nuclear Instruments and Methods in Physics Research Section A: Accelerators, Spectrometers, Detectors and Associated Equipment*, 537(1):363 – 367, 2005. ISSN 0168-9002. doi: https://doi.org/10.1016/j.nima.2004.08.044. URL http://www.sciencedirect.com/science/article/pii/S0168900204018534. Proceedings of the 7th International Conference on Inorganic Scintillators and their Use in Scientific adn Industrial Applications.

[51] Terry C. Awes. The alice electromagnetic calorimeter. *Nuclear Instruments and Methods in Physics Research Section A: Accelerators, Spectrometers, Detectors and Associated Equipment*, 617(1):5 – 8, 2010. ISSN 0168-9002. doi: https://doi.org/10.1016/j.nima.2009.10.010. URL http://www.sciencedirect.com/science/article/pii/S0168900209019032. 11th Pisa Meeting on Advanced Detectors.

[52] A. FernÃąndez, E. GÃąmez, G. Herrera, R. LÃşpez, I. LeÃşn-MonzÃşn, M.I. MartÃŋnez, C. Pagliarone, G. Paic, S. RomÃąn, G. Tejeda, M.A. Vargas, S. Vergara, L. VillaseÃśor, and A. Zepeda. Acorde a cosmic ray detector for alice. *Nuclear Instruments and Methods in Physics Research Section A: Accelerators, Spectrometers, Detectors and Associated Equipment*, 572(1):102 – 103, 2007. ISSN 0168-9002. doi: https://doi.org/10.1016/j.nima.2006.10.336. URL http://www.sciencedirect.com/science/article/pii/S016890020602016X. Frontier Detectors for Frontier Physics.

[53] P Cortese et al. ALICE technical design report on forward detectors: FMD, T0 and V0. 2004.

[54] G. Dellacasa et al. ALICE technical design report: Photon multiplicity detector (PMD). 1999.

[55] G. Dellacasa et al. ALICE technical design report of the zero degree calorimeter (ZDC). 1999.

[56] Michael Annan Lisa, Scott Pratt, Ron Soltz, and Urs Wiedemann. Femtoscopy in relativistic heavy ion collisions: Two decades of progress. *Annual Review of Nuclear and Particle Science*, 55:357–402, 2005. ISSN 0163-8998. doi: 10.1146/annurev.nucl.55.090704.151533.

[57] K. Aamodt et al. Production of pions, kaons and protons in pp collisions at $\sqrt{s} = 900$ gev with alice at the lhc. *The European Physical Journal C*, 71(6):1655, Jun 2011. ISSN 1434-6052. doi: 10.1140/epjc/s10052-011-1655-9. URL `https://doi.org/10.1140/epjc/s10052-011-1655-9`.

[58] Miklos Gyulassy and Xin-Nian Wang. Hijing 1.0: A monte carlo program for parton and particle production in high energy hadronic and nuclear collisions. *Computer Physics Communications*, 83(2):307 – 331, 1994. ISSN 0010-4655. doi: https://doi.org/10.1016/0010-4655(94)90057-4. URL `http://www.sciencedirect.com/science/article/pii/0010465594900574`.

[59] Przemyslaw Karczmarczyk. Analysis of emission asymmetry based on non-identical particle femtoscopy in heavy-ion collisions at lhc energies, 2016.

[60] A. Kisiel. Non-identical Particle Correlation Analysis in the Presence of Non-femtoscopic Correlations. *Acta Physica Polonica B*, 48:717, 2017. doi: 10.5506/APhysPolB.48.717.

[61] Adam Kisiel. CorrFit - a program to fit arbitrary two-particle correlation functions. *Nukleonika*, 49(suppl.2):s81–s83, 2004.

[62] S.E Koonin. *PLB70*, 2010.

[63] S. Pratt. *Phys. Rev. C42*, 1990.

[64] K. Aamodt et al. Two-pion Bose-Einstein correlations in central Pb-Pb collisions at $\sqrt{s_{NN}} = 2.76$ TeV. *Phys. Lett.*, B696:328–337, 2011. doi: 10.1016/j.physletb.2010.12.053.

[65] Adam Kisiel. Pion-kaon femtoscopy in pb-pb collisions at $\sqrt{s_{NN}} = 2.76$ tev modeled in (3+1)d hydrodynamics coupled to the therminator 2 code, and the effect of delayed kaon emission. *Phys. Rev. C*, 98:044909, Oct 2018. doi: 10.1103/PhysRevC.98.044909. URL `https://link.aps.org/doi/10.1103/PhysRevC.98.044909`.